COMPUTATIONAL SIMULATIONS OF COMPRESSIBLE TRANSITIONAL FLOWS IN A

TURBINE VANE CASCADE

A Thesis
Submitted to the Graduate Faculty
of the
North Dakota State University
of Agriculture and Applied Science

By

Alan James Perrault

In Partial Fulfillment of the Requirements
for the Degree of
MASTER OF SCIENCE

Major Department:
Mechanical Engineering

April 2019

Fargo, North Dakota

North Dakota State University
Graduate School

Title

Computational Simulations of Compressible Transitional Flows in a
Turbine Vane Cascade

By

Alan James Perrault

The Supervisory Committee certifies that this ***disquisition*** complies with North Dakota

State University's regulations and meets the accepted standards for the degree of

MASTER OF SCIENCE

SUPERVISORY COMMITTEE:

Dr. Bora Suzen
Chair

Dr. Jordi Estevadeordal

Dr. Om Yadav

Dr. Forrest Ames

Approved:

4/15/2019	Dr. Alan Kallmeyer
Date	Department Chair

ABSTRACT

In order to improve the efficiency and reduce the emissions of aircraft engines, new combustor designs have been developed to reduce outlet temperatures and increase mixing. At high altitudes, the low pressure and low Reynolds number flow would normally produce a laminar boundary layer on the turbine vanes. The increased turbulence generated by these newer combustors can cause transitional flow on the vane surfaces, which leads to increased heat transfer. Accurate computational simulations can reduce development costs by allowing rapid iteration of designs. Aerodynamic and heat transfer characteristics of the first stage stator vane from a high-altitude UAV has been computationally analyzed using ANSYS CFX. The computational results are compared with compressible flow experiments which were previously conducted at the University of North Dakota. The aerodynamic results show excellent agreement across the vane surface; however, some discrepancies are present in the transition region for the heat transfer results.

ACKNOWLEDGEMENTS

TABLE OF CONTENTS

LIST OF TABLES

LIST OF FIGURES

LIST OF ABBREVIATIONS

CCAST..Center for Computationally Assisted Science and Technology at NDSU

CFD...Computational fluid dynamics

DNS...Direct numerical simulation

HT ....High turbulence

LES ....Large eddy simulation

LT..Low turbulence

RANS...Reynolds-averaged Navier-Stokes

RMS ....Root mean square

SAS ....Scale-adaptive simulation

SST..Shear stress transport

UAV...Unmanned aerial vehicle

LIST OF SYMBOLS

c ....chord length, m

e ....internal energy

h ....heat transfer coefficient, W/m^2-K

k ....turbulent kinetic energy, m^2/s^2

K_t ....flow acceleration parameter, $\left(\dfrac{\nu}{U^2}\right)\left(\dfrac{dU}{ds}\right)$

l ....turbulence length scale, m

L_{ref} ....reference length, m

Lu ....turbulence energy scale, m

Ma ....Mach number, $\dfrac{u}{a}$

P_s ....static pressure, Pa

P_t ....total pressure, Pa

q'' ....heat flux from vane surface, W/m^2

Re ....Reynolds number, $\dfrac{\rho U L_{ref}}{\mu}$

S ....surface arc length, m

t ....time

Tu ....free stream turbulence intensity

u ....x-component of velocity (m/s)

u' ....streamwise fluctuation velocity, m/s

U ....streamwise velocity, m/s

U_∞ ....freestream velocity

v ....y-component of velocity (m/s)

v' ....normal fluctuation velocity, m/s

w ....z-component of velocity (m/s)

γ ....intermittency factor

ε ....turbulent dissipation rate, m^2/s^3

θ ....momentum thickness, m

μ ....molecular viscosity, Pa-s

μ_t ....eddy viscosity, Pa-s

v ....kinematic viscosity, $\dfrac{\mu}{\rho}$, m^2/s

v_t ....kinematic eddy viscosity, $\dfrac{\mu_t}{\rho}$, m^2/s

ρ ....density, kg/m^3

τ_w ....wall shear

ω ....turbulent eddy frequency, s^{-1}

Ω ....total pressure loss coefficient, $\dfrac{P_{T,in} - P_{T,ex}}{P_{T,in} - P_{s,ex}}$

1. INTRODUCTION AND RESEARCH OBJECTIVES

When designing new components for a gas turbine engine, development costs can be reduced by replacing physical models with computational fluid dynamics (CFD) simulations early in the design process. Recent developments in gas turbine technology have attempted to both increase the efficiency and reduce pollution from the exhaust. Two different problems that are actively being addressed are NO_x production and incomplete combustion. In order to reduce the production of NO_x within aircraft engines, designers have increased the amount of excess air within the combustion chamber. By pushing more air through the engine, the exhaust temperature can be reduced. To promote more complete combustion, recent engines have been designed to increase the turbulence level within the combustion chamber. This additional turbulence can lead to increased heat transfer to the first stage stator vanes (Ames, Argenziano, & Wang 2004). Both of these modifications make the flow within a gas turbine more complex. For simulation results to be accurate, the designers need models which can accurately handle the turbulence within the flow as well as the transitional regions as the flow transitions from laminar to turbulent.

Throughout the years, many different turbulence models have been developed which can accurately predict many different types of turbulent flows. For the cases that will be examined as part of this research, the Shear Stress Transport (SST) turbulence model (Menter, 1994) will be used. It has been shown to accurately predict many different types of flows (Bardina, Huang, & Coakley, 1997). The transition model examined as part of this research is the γ-Re_θ transition model (Menter et al., 2006). This model has been shown to accurately predict transition within a flow over a wide range of Reynolds numbers and Mach numbers (Suzen & Huang, 2005). Previous research has shown; however, that as the Reynolds number and Mach number increase,

1

the γ-Re$_\theta$ transition model over predicts heat transfer in low speed, incompressible flows (Kingery, Suzen, & Ames, 2010).

  The goal of this research is to validate the SST turbulence model and the γ-Re$_\theta$ transition model for use in simulating the first stage stator vane from a high-altitude UAV. The low pressure at high altitudes produces a low Reynolds number flow within the turbine. The Reynolds number is low enough that the start of the boundary layer on the vane is laminar. Under high enough free stream turbulence levels, the boundary layer will experience a transition to fully turbulent flow. Accurately predicting the start of transition and the length of the transitional region presents a challenge for the current turbulence and transition models, so it makes an excellent validation case study.

2. INTRODUCTION TO TURBULENCE AND TRANSITION

2.1. Turbulent Flow

Fluid flow can either be laminar or turbulent. Laminar flow is smooth and well-ordered while turbulent flow has many random and chaotic fluctuations. These fluctuations can include changes in velocity, pressure, and temperature among other things. Fully laminar flow is mostly a theoretical construct as most real flows have at least a small amount of turbulence. The random nature of a turbulent flow makes it impossible to produce an analytical solution for the governing equations for turbulent flow.

2.1.1. Introduction to Turbulent Flow

Engineers and scientists have been studying turbulent flow phenomenon for many years. As most real flows are turbulent, it is important area of consideration for many design problems. With how important turbulence is, it is surprisingly difficult to pin down an exact definition. Osborn Reynolds described the difference between laminar and turbulent flow as such (Reynolds, 1883):

> *"... the internal motion of water assumes one or other of two broadly distinguishable forms—either the elements of the fluid follow one another along lines of motion which lead in the most direct manner to their destination, or they eddy about in sinuous paths the most indirect possible."*

While this provides a simplistic description of turbulence, it is not a definition. Hinze (1959) provides a better definition that more fully describes what is happening in a turbulent flow field. According to Hinze's definition, "Turbulent fluid motion is an irregular condition of the flow in which the various quantities show a random variation with time and space coordinates, so that

statistically distinct average values can be discerned" (Hinze, 1959). Although this definition covers the most important aspect of turbulent flow, it is by no means all inclusive.

As eluded to in Hinze's definition, turbulent flow includes random fluctuations in the field variables from a discernable mean value. There are also other aspects of turbulent flow, suggested by Frank White (2006), which are also important. The random fluctuations occur as a part of eddies within the flow field. These eddies range in size. Larger eddies correspond to larger fluctuations from the mean values. As the eddies become smaller, the fluctuations decrease until they become zero. The turbulent motion is also self-sustaining with new eddies being formed as other eddies dissipate and disappear. The turbulent eddies also increase mixing within the flow which accelerates the diffusion of mass, momentum, and energy (White, 2006).

2.1.2. Turbulent Length Scales

Turbulence occurs on a continuum with a wide range of different length scales rather than having discrete size steps. The largest turbulent eddies within a flow have characteristic length (ℓ) and velocity (v) scales on the same order of magnitude as the length (L) and velocity (U) scales of the mean flow. Due to gradients in the mean flow, these large eddies are pulled and distorted by a process called vortex stretching. Angular momentum is conserved during the vortex stretching process which causes the eddy diameter to shrink and the rotational velocity to increase. These larger eddies in turn affect smaller eddies, causing them to stretch and distort. Through this process, called the energy cascade, kinetic energy is passed from larger to smaller eddies (Versteeg & Malalasekera 2007). The transfer of kinetic energy continues all the way down to the smallest scale eddies within the flow field.

The size of the smallest eddies within a turbulent flow is controlled by viscous dissipation. The universal equilibrium theory, proposed by Kolmogorov in 1941, says that the

4

smallest eddies are in a state where their rate of receiving kinetic energy from larger eddies is approximately equal to the rate of viscous dissipation as heat (Kolmogorov, 1941). Based on this theory, it can be inferred that the scale of the smallest eddies will be controlled by the rate energy is transferred from larger to smaller eddies (ε) and the kinematic viscosity (v) of the fluid. Using dimensional analysis, the Kolmogorov length (η) time (τ) and velocity (υ) scales can be defined and are shown in equation (2.1).

$$\eta \equiv \left(\frac{v^3}{\varepsilon} \right)^{\frac{1}{4}}, \quad \tau \equiv \left(\frac{v}{\varepsilon} \right)^{\frac{1}{2}}, \quad \upsilon = \left(v\varepsilon \right)^{\frac{1}{4}} \tag{2.1}$$

Although these scales are fairly small, they are significantly larger than the molecular scale. This allows a continuum approach to be used for turbulence modeling (Wilcox, 2006).

2.1.3. Equations of Motion for Fluid Flow

A discussion on turbulent flow would be incomplete without first examining the governing equations of fluid flow. These equations are formed from three different principles. The first is conservation of mass, which says that mass cannot be created nor destroyed. The second is the conservation of momentum. This is derived from Newton's second law, which states the net force on an object is equal to object's mass times its acceleration. The final principle is the conservation of energy, which states energy cannot be created or destroyed.

The full conservation of mass equation for a compressible and three-dimensional flow field is shown in equation (2.2). This equation is also known as the continuity equation.

$$\frac{\partial \rho}{\partial t} + \left[\frac{\partial (\rho u)}{\partial x} + \frac{\partial (\rho v)}{\partial y} + \frac{\partial (\rho w)}{\partial z} \right] = 0 \tag{2.2}$$

The conservation of momentum equation is a vector equation with three different components, x, y, and z. The three components of the conservation of momentum are shown in

5

equations (2.3), (2.4), and (2.5). These equations are also known as the Navier-Stokes equations, after the physicists who originally derived them.

$$\rho \frac{Du}{Dt} = \rho g_x - \frac{\partial p}{\partial x} + \frac{\partial}{\partial x}\left(2\mu \frac{\partial u}{\partial x} + \lambda \mathrm{div}\mathbf{V}\right) + \frac{\partial}{\partial y}\left[\mu\left(\frac{\partial u}{\partial y} + \frac{\partial v}{\partial x}\right)\right] + \frac{\partial}{\partial z}\left[\mu\left(\frac{\partial w}{\partial x} + \frac{\partial u}{\partial z}\right)\right] \qquad (2.3)$$

$$\rho \frac{Dv}{Dt} = \rho g_y - \frac{\partial p}{\partial y} + \frac{\partial}{\partial x}\left(\mu\left(\frac{\partial v}{\partial x} + \frac{\partial u}{\partial y}\right)\right) + \frac{\partial}{\partial y}\left[2\mu \frac{\partial v}{\partial y} + \lambda \mathrm{div}\mathbf{V}\right] + \frac{\partial}{\partial z}\left[\mu\left(\frac{\partial v}{\partial z} + \frac{\partial w}{\partial y}\right)\right] \qquad (2.4)$$

$$\rho \frac{Dw}{Dt} = \rho g_z - \frac{\partial p}{\partial z} + \frac{\partial}{\partial x}\left(\mu\left(\frac{\partial w}{\partial x} + \frac{\partial u}{\partial z}\right)\right) + \frac{\partial}{\partial y}\left[\mu\left(\frac{\partial v}{\partial z} + \frac{\partial w}{\partial y}\right)\right] + \frac{\partial}{\partial z}\left[2\mu \frac{\partial w}{\partial z} + \lambda \mathrm{div}\mathbf{V}\right] \qquad (2.5)$$

Both the conservation of mass equation and the conservation of momentum equations can be condensed and rewritten in vector form. In vector form, the equations are

$$\frac{D\rho}{Dt} + \rho \,\mathrm{div}\mathbf{V} = 0 \qquad (2.6)$$

$$\rho \frac{D\mathbf{V}}{Dt} = \rho \boldsymbol{g} - \nabla p + \frac{\partial}{\partial x_j}\left[\mu\left(\frac{\partial v_i}{\partial x_j} + \frac{\partial v_j}{\partial x_i}\right) + \delta_{ij}\lambda \,\mathrm{div}\,\mathbf{V}\right] \qquad (2.7)$$

The last governing equation, the conservation of energy, is shown in equation (2.8).

$$\rho \frac{D}{Dt}\left(e + \frac{p}{\rho}\right) = \frac{Dp}{Dt} + \mathrm{div}\left(k\nabla T\right) + \tau'_{ij}\frac{\partial u_i}{\partial x_j} \qquad (2.8)$$

The conservation of energy equation is based on the First Law of Thermodynamics, which states the change in energy of a system is equal to the net energy and work in and out of the system. This equation can be further simplified using other relationships, depending on the type of flow. One simplification is replacing the internal energy with enthalpy, which can be related using equation (2.9). Enthalpy can be used to calculate the flow work done by a fluid passing through an open system. In many cases, it will be more useful than internal energy alone.

$$h = \left(e + \frac{p}{\rho}\right) \qquad (2.9)$$

The last term in equation (2.8) is called the dissipation function and is defined as

$$\Phi = \tau'_{ij} \frac{\partial u_i}{\partial x_j} \tag{2.10}$$

With both substitutions, the final form of the conservation of energy equation is

$$\rho \frac{Dh}{Dt} = \frac{Dp}{Dt} + \text{div}(k\nabla T) + \Phi \tag{2.11}$$

Once you have the governing equations, they can be used as is or they can be further simplified by making certain assumptions about the flow being analyzed. Two common assumptions are that of constant density (ρ) or incompressible flow and constant viscosity (μ). All real flows are at least somewhat compressible, but for low velocity flows and most liquids, the error from assuming incompressible instead of compressible flow is minimal. The governing equations with the constant density and constant viscosity assumptions are

$$\text{div } \mathbf{V} = 0 \tag{2.12}$$

$$\rho \frac{D\mathbf{V}}{Dt} = \rho \mathbf{g} - \nabla p + \mu \nabla^2 \mathbf{V} \tag{2.13}$$

$$\rho c_p \frac{DT}{Dt} \approx \text{div}(k\nabla T) \tag{2.14}$$

One additional assumption that is commonly made is that of constant thermal conductivity. Thermal conductivity primarily depends on the material temperature; therefore, constant thermal conductivity is a valid assumption for constant temperature flows or flows with small temperature changes. The incompressible heat-convection equation (White, 2006), which assumes constant density and thermal conductivity, is shown in equation (2.15).

$$\rho c_p \frac{DT}{Dt} \approx k\nabla^2 T \tag{2.15}$$

2.1.4. Reynolds-Averaged Equations

Within turbulent flow, the different flow properties exhibit random fluctuations over time. This can include the pressure and temperature as well as the three components of velocity. In order to handle the random fluctuations, a statistical method is required to solve the governing equations. It is most convenient to use an approach first proposed by Osborne Reynolds in 1895, where the turbulent flow properties are split into two parts, a mean or average part and fluctuating turbulent part. An example be seen in equation (2.16) for the u velocity, where $\bar{u}$ is the mean velocity and u' is the fluctuating velocity. A similar equation can be written for all of the other flow variables.

$$u(x) = \bar{u}(x) + u'(x) \tag{2.16}$$

The contrast between $\bar{u}$ and u' is shown in Figure 2.1, which has a set of overlaid instantaneous velocity profiles on the left and the corresponding average boundary layer profile on the right. It is much easier to deal with the average boundary layer profile on the right.
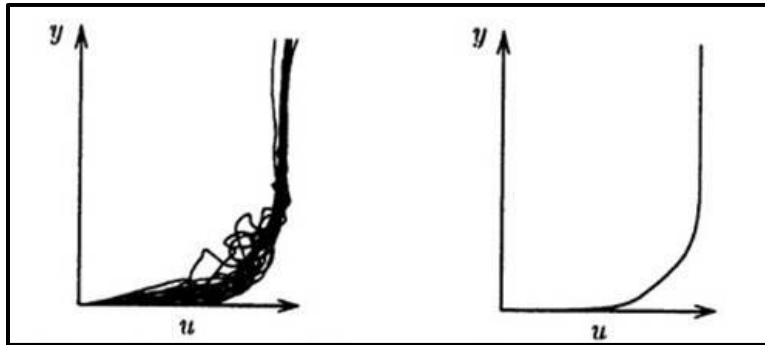
Figure 2.1. Instantaneous (left) and averaged (right) velocity profiles (Wilcox, 2006)

There are three main forms of Reynolds averaging that are useful for turbulence modeling: time averaging, spatial averaging, and ensemble averaging. Time averaging is the most commonly used form of averaging because it appropriate for stationary turbulence. This means the flow being analyzed is steady state and independent of time, covering most turbulent

flows in engineering. For this type of averaging, a flow variable is given as *f(x,t)* and its average is $F_T(x)$, which is given by

$$F_T(x) = \lim_{T \to \infty} \frac{1}{V} \int_t^{t+T} f(x,t) dt \tag{2.17}$$

The second type of averaging is spatial averaging. This type of averaging is used for homogenous turbulence, which, on average, is uniform in all directions. It is calculated by taking a volume integral over all the coordinates within the flow domain. The spatial average (F_V) can be calculated as

$$F_V(t) = \lim_{V \to \infty} \frac{1}{V} \iiint_V f(x,t) dV \tag{2.18}$$

The last type of averaging is ensemble averaging (F_E). This is most general type of averaging. If *N* identical experiments are completed, with only small random changes, and *f(x,t)* = $f_n(x,t)$ for the *n*ᵗʰ experiment, the ensemble average can be calculated using

$$F_E(x,t) = \lim_{N \to \infty} \frac{1}{N} \sum_{n=1}^{N} f_n(x,t) \tag{2.19}$$

The ergodic hypothesis states that all three types of averaging are equal for turbulence that is both stationary and homogeneous (Wilcox, 2006). Time averaging is the most applicable for engineering problems, so it will be used for the development of the Reynolds averaged governing equations. The governing equations for incompressible flow are shown in Equations (2.20) and (2.21).

$$\frac{\partial u_i}{\partial x_i} = 0 \tag{2.20}$$

$$\rho \frac{\partial u_i}{\partial t} + \rho u_j \frac{\partial u_i}{\partial x_j} = -\frac{\partial p}{\partial x_i} + \frac{\partial \tau_{ij}}{\partial x_j} \tag{2.21}$$

9

In these equations, u_i is velocity, x_i is position, p is pressure, ρ is density and τ_{ij} is the viscous stress tensor defined by

$$\tau_{ij} = 2\mu s_{ij} \tag{2.22}$$

Where μ is the viscosity and s_{ij} is the strain-rate tensor defined by

$$s_{ij} = \frac{1}{2}\left(\frac{\partial u_i}{\partial x_j} + \frac{\partial u_j}{\partial x_i}\right) \tag{2.23}$$

The strain-rate tensor is symmetric for simple viscous fluids, so $s_{ij} = s_{ji}$ and $\tau_{ij} = \tau_{ji}$. The convective term of the momentum equation can be rewritten in conservative form using conservation of mass, Equation (2.24). This helps to simplify the process of calculating the time averages.

$$u_j \frac{\partial u_i}{\partial x_j} = \frac{\partial}{\partial x_j}\left(u_j u_i\right) - u_i \frac{\partial u_j}{\partial x_j} = \frac{\partial}{\partial x_j}\left(u_j u_i\right) \tag{2.24}$$

Equations (2.21), (2.22), and (2.23) can be combined to give the Navier-Stokes equation in conservative form.

$$\rho \frac{\partial u_i}{\partial t} + \rho \frac{\partial}{\partial x_j}\left(u_j u_i\right) = -\frac{\partial p}{\partial x_i} + \frac{\partial}{\partial x_j}\left(2\mu s_{ij}\right) \tag{2.25}$$

The two velocity components shown in Equation (2.16) can be substituted into the governing equations. Then the governing equations are time averaged, yielding the Reynolds averaged equations of motion in conservative form, which are as follows

$$\frac{\partial \bar{u}_i}{\partial x_i} = 0 \tag{2.26}$$

$$\rho \frac{\partial \bar{u}_i}{\partial t} + \rho \frac{\partial}{\partial x_j}\left(\bar{u}_j \bar{u}_i - \overline{u'_j u'_i}\right) = -\frac{\partial \bar{p}}{\partial x_i} + \frac{\partial}{\partial x_i}\left(2\mu \bar{s}_{ji}\right) \tag{2.27}$$

The time averaged conservation of mass equation is nearly the same as its instantaneous counterpart, Equation (2.25). The only difference is the instantaneous velocity is replaced with the mean velocity. The Navier-Stokes equations are similar in that all the instantaneous quantities have now become time averaged quantities; however, there is one new term $-\overline{u_i' u_j'}$. A more popular form of the Navier-Stokes can be written using equation (2.24) in reverse.

$$\rho \frac{\partial \overline{u}_i}{\partial t} + \rho \overline{u}_j \frac{\partial \overline{u}_i}{\partial x_j} = -\frac{\partial \overline{p}}{\partial x_i} + \frac{\partial}{\partial x_j} \left(2\mu \overline{s}_{ji} - \rho \overline{u_j' u_i'} \right) \tag{2.28}$$

Equation (2.28) is usually called the Reynolds-averaged Navier-Stokes (RANS) equation.

The quantity $-\rho \overline{u_i' u_j'}$ is called the Reynolds stress tensor. This new term, comprised of fluctuating velocity components, is the fundamental problem of turbulence modeling (Wilcox, 2006). The term as it appears in equation (2.28) without density is the specific Reynolds stress tensor and is

$$t_{ij} = -\overline{u_i' u_j'} \tag{2.29}$$

The specific Reynolds stress tensor is symmetric, such that $t_{ij} = t_{ji}$, so this means 6 additional unknowns are added to our system of equations. There is not a corresponding increase in the number of equations, nor is there an analytical method for calculating the different tensor values. This is the turbulence closure problem. The primary goal of turbulence modeling is to model the specific Reynolds stress tensor. By closing the system in this manner, it is possible to solve the governing equations for turbulent flow.

2.2. Transition from Laminar to Turbulent Flow

In many cases, fluid flows are treated as either fully turbulent or fully laminar. This has the benefit of simplifying an analysis; however, it is not always accurate. Many different flows can be transitional in nature, changing from laminar to fully turbulent. For many applications,

flow transition may have a negligible effect on the final system performance, but in other cases transitional flows may be extremely important. Gas turbines are one area where transitional flow can have a large effect on performance. While the overall flow through a gas turbine is extremely turbulent, the boundary layer flow across the turbine's individual blades can be laminar, turbulent, or transitional (Mayle, 1991).

The Reynolds number, which is the ratio of inertial forces to viscous forces within a flow, can provide some guidance as to the type of flow that is occurring. If the Reynolds number is small, the viscous forces dominate. The turbulent fluctuations within the flow are damped out by the viscous forces, resulting in laminar flow. If the Reynolds number is large, the inertial forces dominate, which results in unimpeded turbulent fluctuations and turbulent flow. Transitional flow occurs at a range of Reynolds numbers in between laminar and turbulent Reynolds numbers. There are no exact Reynolds numbers that guarantee whether a flow is laminar or turbulent. For many types of flows, there are guidelines to help make reasonable assumptions, but the actual flow will be influenced by the specifics of the situation. Laminar flow can be maintained to a much higher than normal Reynolds number if extreme care is taken to reduce free stream turbulence levels and other possible disturbances. Similarly, fully turbulent flow can be present at much lower than normal Reynolds numbers if there is high free stream turbulence levels or a tripping mechanism is used.

2.2.1. Modes of Transition

There are three different common modes of transition: natural transition, bypass transition, and separated flow transition. The type of transition a flow experiences will depend on different parameters of the flow, such as pressure gradient and the free stream turbulence levels.

2.2.1.1. Natural Transition

Natural transition occurs in boundary layer flows with low free stream turbulence levels. The flow will usually begin as stable, laminar flow, and the boundary layer will grow until a critical Reynolds number based on the momentum thickness is reached. At that point, the boundary layer will start to become unstable and two-dimensional disturbances, known as Tollmien-Schlichting waves, will develop. This is followed by further instability growth with the formation of three-dimensional eddies and vortices. Next, the eddies and vortices breakdown into three-dimensional fluctuations and spots of highly turbulent flow appear. The spots grow and expand into each other until the boundary layer is comprised of fully turbulent flow (White, 2006) (Mayle, 1991). The stages of natural transition are shown in Figure 2.2.
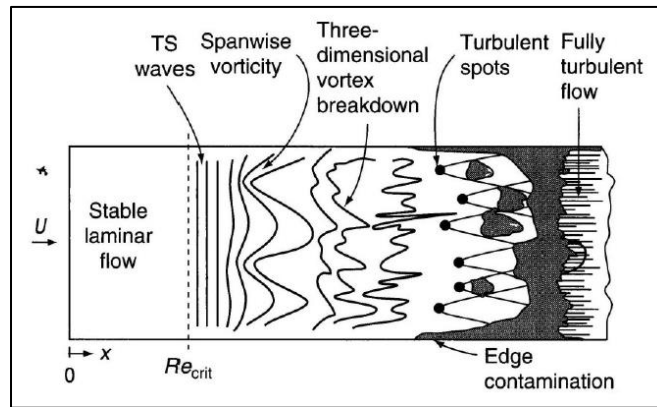
Figure 2.2. Stages of natural transition (White, 2006)

2.2.1.2. Bypass Transition

Bypass transition, as the name suggests, skips over the first three stages of natural transition. The initial Tollmien-Schlichting waves are not present and turbulent spots within the boundary layer are the main indicator of the onset of turbulent flow. Bypass transition is generally due to some sort external stimuli, such as a high free stream turbulence level or surface roughness. With high free stream turbulence levels, it is believed that the turbulent eddies within

13

the free stream enter the boundary layer and accelerate the formation of turbulent spots (Volino and Simon, 1991).

2.2.1.3. Separated-Flow Transition

If a laminar flow separates from a surface, either due to a tripping mechanism or an adverse pressure gradient, a transition to turbulent flow may occur above the laminar separation bubble. The different natural transition processes may or may not be present during this type of transition. At the end of the separation bubble, the flow reattaches as fully turbulent. Figure 2.3 shows transitional flow around a laminar separation bubble.
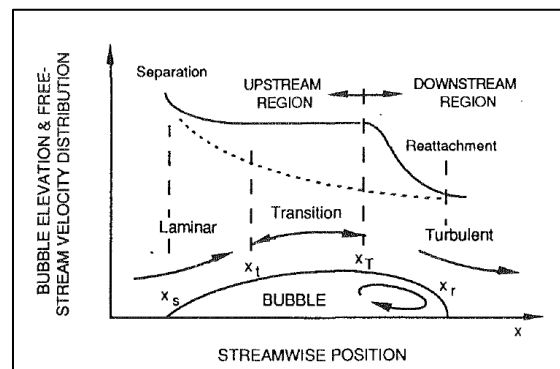
Figure 2.3. Separated-flow transition (Mayle, 1991)

Separated-flow transition is important for turbomachinery applications. It can occur at the blades leading edge or along the suction surface where the pressures are low. Separation bubbles can be either long or short. Short separation bubbles have minimal effect on the surface pressure distribution and cause a quick transition from laminar to turbulent flow. If accounted for in the design process, short separation bubbles can help to increase a turbine's efficiency. Long transition bubbles also cause a transition to turbulence, but they have a more significant effect on the surface pressure distribution. Long separation bubbles can have negative effect on turbine performance, up to and including stall (Mayle, 1991).

14

2.2.1.4. Periodic-Unsteady Transition

Periodic-unsteady transition occurs in gas turbines when the wake or trailing shock wave from an upstream blade row hits the downstream blade row. Due to the rotational nature of the gas turbine, the wake blade interaction location is constantly changing, leading to periodic unsteady flow with the gas turbine. This can cause sudden transitions from laminar to turbulent flow where the wake or shock wave interacts with the downstream blade. As the wake passes, the flow can switch back to laminar flow (Mayle, 1991).

2.2.1.5. Reverse Transition

Reverse transition or relaminarization is the opposite of turbulent transition. In this process, turbulent flow transitions back to laminar flow due to a rapid acceleration in flow velocity. In gas turbines, this can occur near the trailing edge of the pressure surface and leading edge of the suction surface (Mayle, 1991).

2.2.2. Factors Affecting Flow Transition

There are multiple different factors that affect the transition from laminar to turbulent flow. These can include the pressure gradient, free stream turbulence level, compressibility, surface roughness, and surface curvature.

2.2.2.1. Pressure Gradient

The pressure gradient experienced by a flow can have a large effect on the transition to turbulence depending on the free stream turbulence level. For low turbulence levels, the pressure gradient has a much more significant effect on transition. For zero pressure gradient and favorable pressure gradient flows at low turbulence levels, the transition to turbulence can be delayed or even prevented if the acceleration parameter is high enough. At high turbulence levels, the free-stream turbulence level is the most important factor affecting the transition to

turbulence (Mayle, 1991). Adverse pressure gradients cause a much shorter and earlier transition region than what occurs under a favorable or zero pressure gradient. This is accompanied by an increase in the formation rate of turbulent spots (Gostelow, Blunden, & Walker, 1994).

2.2.2.2. Free Stream Turbulence

Free stream turbulence is the other important factor affecting a flow transition from laminar to turbulence. The most important aspect is the turbulence level although the turbulent length scale is also important. As the turbulence level increases, the turbulent spot production rate also increases. This speeds up the natural transition process, causing transition at much smaller Reynolds numbers based on the momentum thickness. At high enough turbulence levels, the natural transition process will be bypassed (Mayle. 1991).

2.2.2.3. Compressibility

There are two factors within a compressible flow that are relevant to transition; the first is the effect on Mach number on the production of turbulent spots within the boundary layer. Previous experimental work shows that higher Mach numbers lead to a delayed transition and lower turbulent spot formation rate. This effect is small when compared to the influences of free stream turbulence level and pressure gradient. The second factor is the interaction of localized shockwaves with the laminar boundary layer. The shock wave can stir up the boundary layer either causing it to become turbulent through a bypass or separated flow mode (Mayle, 1991).

2.2.2.4. Surface Roughness

Surface roughness also influences the transition of a flow from laminar to turbulent. For most flows, a larger surface roughness will cause transition to occur earlier and at a smaller Reynolds number based on the momentum thickness. Surface roughness is more important at

low free stream turbulence levels. At higher free stream turbulence, the turbulence level will force an earlier transition regardless of surface roughness (Mayle, 1991).

2.2.2.5. Surface Curvature

At low turbulence levels, surface curvature can also affect the transition to turbulence. Convex surfaces only show a slight delay in the transition from laminar to turbulence. The centrifugal forces the flow experiences as it travels around the convex surface mildly stabilize the flow field (Schlichting, 1979). Concave surfaces can either delay transition or speed it up depending on the amount of curvature and the free stream turbulence. The effects of both concave and convex surfaces on transition are minor compared to the effects of pressure gradient and free stream turbulence level (Mayle, 1991).

3. TURBULENCE AND TRANSITION MODELING

3.1. Turbulence Modeling

As previously shown in Section 2.1.4., the governing equations for turbulent flow can be transformed into the Reynolds-averaged Navier-Stokes (RANS) equations using a time averaging technique. These new equations can be an extremely powerful tool for analyzing a wide variety of flow fields; however, they also introduce additional unknowns in terms of the Reynolds stress tensors. There exists no analytical solution for these stress tensors; therefore, they must be modeled in order to solve the governing equations. Many different models have been proposed by engineers and scientists over the years, and some of the most relevant models will be examined in detail.

3.1.1. Model Levels

In order to solve the turbulent boundary layer equations, a way to calculate the term $-\overline{u_i' u_j'}$ is needed. The term $-\rho \overline{u_i' u_j'}$ as it appears in Equation (2.28), is the Reynolds stress tensor also called the turbulent shear stress. This allows for a comparison to shear stress for laminar flow. For laminar flow, the shear stress is proportional to the velocity gradient and the molecular viscosity. The Boussinesq assumption says that the same relationship applies to turbulent shear stress if the molecular viscosity is replaced with eddy viscosity (Hoffman & Chiang, 1996). This is shown in Equation (3.1), where v_t is the eddy viscosity.

$$\tau_t = \rho v_t \frac{\partial U}{\partial y} \tag{3.1}$$

Another concept that used to help to model Reynolds stress tensor is the Prandtl mixing length, first introduced by Prandtl. This assumes that a lump of fluid travels a finite distance

before a collision occurs and the lump disperses, losing its identity. The mixing length is the distance this lump of fluid travels.

The simplest turbulence models, called RANS zero-equation models, utilize both the Boussinesq assumption and Prandtl mixing length theory. In these types of models, simple algebraic relations are used to solve for the eddy viscosity and the mixing length. Two common zero equation models are the Cebeci-Smith model (Smith & Cebeci, 1957) and the Baldwin-Lomax model (Baldwin & Lomax, 1978). Both models are empirical formulations that have been fine-tuned using data from different experiments. Both models are useful for specific types of flows as long as the flows are similar to the original experiments used to develop the models (Wilcox, 2006).

The next step up from the zero-equation models are RANS one-equation models. One-equation models typically add a partial differential equation for a velocity scale (Hoffmann & Chiang, 1998). The velocity scale most commonly used is the turbulent kinetic energy k which is defined as

$$k = \frac{1}{2}\left(u'^2 + v'^2 + w'^2\right) \tag{3.2}$$

One-equation turbulence models that solve the turbulent kinetic energy equation are considered incomplete because they still relate the turbulence length scale to a flow dimension (Wilcox 2006). This type of one-equation model is rarely used. One-equation turbulence models that solve a partial differential equation based on eddy viscosity are more useful as the turbulence length is determined as part of the solution process. An example of this type of turbulence model is the Spalart-Allmaras one-equation turbulence model (Spalart & Allmaras, 1994).

19

The previous types of turbulence models are useful for certain type of flows. However, due to their limited applicability, they are not as commonly used today. They have been superseded by two-equation turbulence models. These types of models solve a partial differential equation for the turbulent kinetic energy and another partial differential equation for a variable related to the turbulence length scale. Three of the most common two-equation turbulence models will be examined in more detail.

3.1.2. *k-ε* Models

The k-ε turbulence model is one of the most common two-equation turbulence models. There are many different formulations that have been proposed over the years, but the most common versions are those of Jones and Launder (1972), and Launder and Sharma (1974). The version of Launder and Sharma is presented here. The k-ε turbulence is based on two partial differential equations that are used to solve for turbulent kinetic energy (*k*) and the dissipation of turbulence (*ε*). Using these variables, the eddy viscosity can be calculated by Equation (3.3).

$$\mu_t = C_\mu f_\mu \rho \frac{k^2}{\varepsilon} \tag{3.3}$$

The model coefficient (C_μ) is an empirical constant determined from an equilibrium analysis at high Reynolds numbers. The damping function (f_μ), Equation (3.4), is modeled in terms of a turbulent Reynolds number (Re_t), Equation (3.5).

$$f_\mu = \exp\left(\frac{-3.4}{\left(1+0.02\,Re_t\right)^2}\right) \tag{3.4}$$

$$Re_t = \frac{\rho k^2}{\mu\varepsilon} \tag{3.5}$$

The following partial differential equations govern the transport of turbulent kinetic energy and turbulent dissipation in the k-ε turbulence model (Bardina, Huang, & Coakley, 1997).

20

$$\frac{\partial \rho k}{\partial t} + \frac{\partial}{\partial x_j}\left[\rho U_j \frac{\partial k}{\partial x_j} - \left(\mu + \frac{\mu_t}{\sigma_k}\right)\frac{\partial k}{\partial x_j}\right] = \tau_{ij}S_{ij} - \rho\varepsilon + \phi_k \tag{3.6}$$

$$\frac{\partial \rho \varepsilon}{\partial t} + \frac{\partial}{\partial x_j}\left[\rho U_j \varepsilon - \left(\mu + \frac{\mu_t}{\sigma_\varepsilon}\right)\frac{\partial \varepsilon}{\partial x_j}\right] = C_{\varepsilon 1}\frac{\varepsilon}{k}\tau_{ij}S_{ij} - C_{\varepsilon 2}f_2\rho\frac{\varepsilon^2}{k} + \phi_\varepsilon \tag{3.7}$$

The damping function in the turbulent dissipation equation is

$$f_2 = 1 - 0.3\exp\left(-\mathrm{Re}_t^2\right) \tag{3.8}$$

The explicit wall terms are

$$\phi_k = 2\mu\left(\frac{\partial\sqrt{k}}{\partial y}\right)^2 \tag{3.9}$$

$$\phi_\varepsilon = 2\mu\frac{\mu_t}{\rho}\left(\frac{\partial^2 u_s}{\partial y^2}\right)^2 \tag{3.10}$$

u_s is the flow velocity parallel to the wall. The purpose of the explicit wall terms is to allow zero to be used as the wall boundary condition for both turbulent kinetic energy and the dissipation of turbulence. The constants for this turbulence model are

$$C_{\varepsilon 1} = 1.45; \quad C_{\varepsilon 2} = 1.92; \quad C_\mu = 0.09; \quad \sigma_k = 1.0; \quad \sigma_\varepsilon = 1.3; \mathrm{Pr}_t = 0.9 \tag{3.11}$$

3.1.3. *k-ω* Models

The k-ω turbulence model is similar to the k-ε turbulence model. There are multiple different k-ω turbulence models. The model presented here is the Wilcox model as documented by Bardina, Huang, and Coakley (1997). The k-ω turbulence model does not require wall damping and provides better near wall results than the k-ε turbulence model. The two partial differential equations are used to solve for the turbulent kinetic energy (*k*) and the turbulent kinetic energy specific dissipation rate (*ω*). The relationship for the eddy viscosity is shown in Equation (3.12).

$$\mu_t = \frac{\rho k}{\omega} \,, \tag{3.12}$$

The transport equations for turbulent kinetic energy and specific dissipation rate are as follows

$$\frac{\partial \rho k}{\partial t} + \frac{\partial}{\partial x_j}\left[\rho U_j k - \left(\mu + \sigma^* \mu_t\right)\frac{\partial k}{\partial x_j}\right] = \tau_{tij} S_{ij} - \beta^* \rho \omega k \tag{3.13}$$

$$\frac{\partial \rho \omega}{\partial t} + \frac{\partial}{\partial x_j}\left[\rho U_j \omega - \left(\mu + \sigma \mu_t\right)\frac{\partial \omega}{\partial x_j}\right] = \alpha \frac{\omega}{k} \tau_{tij} S_{ij} - \beta \rho \omega^2 \tag{3.14}$$

And the required constants are

$$\alpha = \frac{5}{9}; \quad \beta = \frac{3}{40}; \quad \beta^* = \frac{9}{100}; \quad \sigma = \frac{1}{2}; \quad \sigma^* = \frac{1}{2}; \quad \text{Pr}_t = 0.9 \tag{3.15}$$

3.1.4. Shear Stress Transport Model

The k-ω shear stress transport (SST) turbulence model is a hybrid model developed by Florian Menter (1994). It is primarily based on the k-ω turbulence model but incorporates a blending function to transition from the k-ω turbulence model near the wall to a k-ω based formulation of the k-ε turbulence model in the free stream. By combining both turbulence models, it is possible to avoid some of the problems with each. The k-ω turbulence model does an excellent job in the near wall region but shows an extreme sensitivity in the wake region to the free stream specific turbulence dissipation value (Menter, 1994). The k-ε turbulence model does not have the same problem with free stream values, so it is preferable to use it outside the boundary layer. Both turbulence models together allow the SST turbulence model to perform well in cases of adverse pressure gradients and separated flows.

The eddy viscosity, which has been modified from the original k-ω formulation in order to limit the max possible eddy viscosity, is shown below in Equation (3.16).

22

$$\mu_t = \frac{\rho k / \omega}{\max\left[1; \Omega F_2 / (a_1 \omega)\right]}; \quad a_1 = 0.31$$

(3.16)

The blending function (F_2) is based the distance from the wall (y).

$$F_2 = \tanh\left\{\left(\max\left[2\frac{\sqrt{k}}{0.09\omega y}; \frac{500\mu}{\rho y^2 \omega}\right]\right)\right\}$$

(3.17)

The two transport equations for SST turbulence model are shown below. Equation (3.18) governs the transport of turbulent kinetic energy and is similar to the turbulent kinetic energy equation for the k-ω turbulence model. Equation (3.19) governs the transport of the specific dissipation of turbulence.

$$\frac{\partial \rho k}{\partial t} + \frac{\partial}{\partial x_j}\left[\rho U_j k - (\mu + \sigma_k \mu_t)\frac{\partial k}{\partial x_j}\right] = \tau_{tij}S_{ij} - \beta^* \rho \omega k$$

(3.18)

$$\frac{\partial \rho \omega}{\partial t} + \frac{\partial}{\partial x_j}\left[\rho U_j \omega - (\mu + \sigma_\omega \mu_t)\frac{\partial \omega}{\partial x_j}\right] = P_\omega - \beta \rho \omega^2 + 2(1 - F_1)\frac{\rho \sigma_{\omega 2}}{\omega}\frac{\partial k}{\partial x_j}\frac{\partial \omega}{\partial x_j}$$

(3.19)

For both transport equations, function F_1 serves as a blending function to smoothly switch from the model coefficients of the original k-ω turbulence model in the near wall region to the k-ε turbulence model coefficients at the edge of the boundary layer.

$$F_1 = \tanh\left\{\left(\min\left[\max\left[\frac{\sqrt{k}}{0.09\omega y}; \frac{500\mu}{\rho y^2 \omega}\right]; \frac{4\rho\sigma_{\omega 2}k}{CD_{k\omega}y^2}\right]\right)^4\right\}$$

(3.20)

$$CD_{k\omega} = \max\left[\frac{2\rho\sigma_{\omega 2}}{\omega}\frac{\partial k}{\partial x_j}\frac{\partial \omega}{\partial x_j}; 10^{-20}\right]$$

(3.21)

The model coefficients are transformed using the following function based on the blending function (F_1) (Menter, 1994)

$$\phi = F_1\phi_1 + (1 - F_1)\phi_2 \quad \text{where} \quad \phi = \{\sigma_k, \sigma_\omega, \beta, \gamma\}$$

(3.22)

23

ϕ_1 represents any of the constants from the original k-ω turbulence model and ϕ_2 represents any of the model constants of the transformed k-ε turbulence model.

One modification to the SST turbulence model is a correction for curvature. This helps to adjust the original turbulence model to account for the effects of curvature on the turbulent boundary layer. Spalart and Shur (1997) published the original curvature correction model for the Spalart-Allmaras one-equation turbulence model (Spalart & Allmaras, 1994). In their correction, they multiplied the production term in the Spalart-Allmaras model by a rotation function which is defined as (Spalart & Shur, 1997)

$$f_{rotation} = (1 + c_{r1}) \frac{2r^*}{1 + r^*} \left(1 - c_{r3} \tan^{-1} (c_{r2} \bar{r}) \right) - c_{r1} \tag{3.23}$$

The Spalart and Shur (1997) curvature correction was adapted by Smirnov and Menter (2009) for use with the SST two-equation turbulence model. In order to ensure numerical stability and to prevent over production of turbulence, the rotation function needed to be bound between zero and 1.25 (Smirnov & Menter, 2009). This is expressed as

$$f_{r1} = \max \left\{ \min (f_{rotation}, 1.25), 0.0 \right\} \tag{3.24}$$

This is incorporated into the original SST model as

$$\frac{\partial (\rho k)}{\partial t} + \frac{\partial (\rho u_j k)}{\partial x_j} = P_k f_{r1} - \beta^* \rho \omega k + \frac{\partial}{\partial x_j} \left[\mu_{effective} \frac{\partial k}{\partial x_j} \right] \tag{3.25}$$

$$\frac{\partial (\rho \omega)}{\partial t} + \frac{\partial (\rho u_j \omega)}{\partial x_j} = \alpha \frac{\rho P_k}{\mu_t} f_{r1} - D_\omega + Cd_\omega + \frac{\partial}{\partial x_j} \left[\mu_{effective} \frac{\partial \omega}{\partial x_j} \right] \tag{3.26}$$

The arguments for the rotation function are r^* and $\bar{r}$, which are defined as the following for the SST turbulence model.

$$r^* = \frac{S}{\Omega} \tag{3.27}$$

$$\bar{r} = 2\Omega_{ik}S_{jk}\left[\frac{DS_{ij}}{Dt} + \left(\varepsilon_{imn}S_{jn} + \varepsilon_{jmn}S_{in}\right)\Omega_m^{rot}\right]\frac{1}{\Omega D^3} \tag{3.28}$$

Where

$$S_{ij} = \frac{1}{2}\left(\frac{\partial u_i}{\partial x_j} + \frac{\partial u_j}{\partial x_i}\right) \tag{3.29}$$

$$\Omega_{ij} = \frac{1}{2}\left(\left(\frac{\partial u_i}{\partial x_j} - \frac{\partial u_j}{\partial x_i}\right) + 2\varepsilon_{mji}\Omega_m^{rot}\right) \tag{3.30}$$

$$S^2 = 2S_{ij}S_{ij} \tag{3.31}$$

$$\Omega^2 = 2\Omega_{ij}\Omega_{ij} \tag{3.32}$$

$$D^2 = \max\left(S^2, 0.09\omega^2\right) \tag{3.33}$$

And the empirical constants are

$$c_{r1} = 1.0; \quad c_{r2} = 2.0; \quad c_{r3} = 1.0 \tag{3.34}$$

Ω_m^{rot} is defined rotation rate of the reference frame for the calculations.

The modified SST turbulence model with the curvature correction model was tested against several different experimental cases involving a curved flow field. For many of the cases, the results showed a noticeable improvement over the original SST turbulence model results (Smirnov & Menter, 2009).

As implemented in ANSYS CFX (ANSYS, 2012), the curvature correction model utilizes a constant (*C*) in order allow adjustment of the sensitivity of the correction. This is implemented as shown in Equation (3.35), and then f_{r1} is replaced with $\tilde{f}_r$ in Equations (3.25) and (3.26).

$$\tilde{f}_r = \max\left[0, 1 + C\left(f_{r1} - 1\right)\right] \qquad (3.35)$$

3.1.5. Other Simulation Techniques

In addition to using turbulence models to model the Reynolds stress tensor in the RANS equations, there are also other CFD techniques that can be used to simulate a flow field. Currently the RANS equations are the most popular for industrial applications because they are the least computationally expensive. A RANS simulation deals solely with the mean flow properties. All of the different turbulence scales are modeled rather than needing to be resolved within the simulation.

There are other simulation techniques that attempt to solve the original, unaveraged Navier-Stokes equations. Direct numerical simulation (DNS) solves the original three-dimensional time dependent Navier-Stokes equations over the entire flow field. It attempts to resolve all scales of turbulence within the flow field, which requires an extremely fine grid, increasing the computational requirements. It is estimated that for a Reynolds number of 104, a DNS simulation needs to have at least 109 node points (Versteeg & Malalasekera, 2007). Higher Reynolds numbers would require even more node points. DNS has been used for research purposes, but the high computational cost currently makes it impractical for industrial uses.

Another simulation technique that has seen some use is large eddy simulation (LES). LES is cross between DNS and RANS. Large eddies within the flow field are solved from the Navier-Stokes equations while smaller eddies are modeled. A spatial filtering operation is used to separate the large eddies from the small eddies. Anything smaller than the length specified by the filter is destroyed and needs to be modeled with a sub-grid-size turbulence model (Versteeg & Malalasekera, 2007). Modeling the smallest eddies allows for a coarser mesh than that required for a

comparable DNS simulation. In the future, as additional research is completed and computers continue to become more powerful, both DNS and LES will likely become more widely used.

A third technique is a scale-adaptive simulation (SAS). SAS is a hybrid model for use in transient simulations. It utilizes a RANS turbulence model in steady regions of the flow field and then dynamically switches to LES-like behavior in unsteady detached regions of the flow field (Menter & Egorov, 2005). The von Karman length scale controls how the flow is modeled allowing the switch from RANS to LES-like behavior to occur independent of the grid. The SAS model was originally created with a one-equation RANS turbulence model (Menter, Kuntz, & Bender, 2003) and later expanded to work with the SST two-equation turbulence model (Menter & Egorov, 2005).   The goal of the SAS model is to better capture unsteady turbulent structures within a flow field. In a RANS simulation, the averaging process smooths out many of the smaller turbulent structures only leaving the very largest scales. With the SAS hybrid model, the transition to LES-like behavior allows smaller turbulent structures to develop and influence the flow field.

The SST-SAS model uses a governing equation for turbulent eddy frequency that is similar to the original equation from the base SST model; however, it includes an additional source term (Q_{sas}) (ANSYS, 2012). The modified turbulent kinetic energy and turbulence eddy frequency equations are

$$\frac{\partial \rho k}{\partial t} + \frac{\partial}{\partial x_j}\left(\rho U_j k\right) = P_k - \rho c_\mu k \omega + \frac{\partial}{\partial x_j}\left[\left(\mu + \frac{\mu_t}{\sigma_k}\right)\frac{\partial k}{\partial x_j}\right] \tag{3.36}$$

$$\frac{\partial \rho \omega}{\partial t} + \frac{\partial}{\partial x_j}\left(\rho U_j \omega\right)$$
$$= \alpha \frac{\omega}{k} P_k - \rho \beta \omega^2 + Q_{SAS} + \frac{\partial}{\partial x_j}\left[\left(\mu + \frac{\mu_t}{\sigma_\omega}\right)\frac{\partial \omega}{\partial x_j}\right] + \left(1 - F_1\right)\frac{2\rho}{\sigma_{\omega 2}\omega}\frac{\partial k}{\partial x_j}\frac{\partial \omega}{\partial x_j} \tag{3.37}$$

27

The additional source term for the SST-SAS model (Egorov & Menter, 2007) is

$$Q_{SAS} = \max\left[\rho\zeta_2\kappa S^2\left(\frac{L}{L_{vK}}\right)^2 - C\frac{2\rho k}{\sigma_\Phi}\max\left(\frac{1}{\omega^2}\frac{\partial\omega}{\partial x_j}\frac{\partial\omega}{\partial x_j}, \frac{1}{k^2}\frac{\partial k}{\partial x_j}\frac{\partial k}{\partial x_j}\right), 0 \right] \tag{3.38}$$

The model constants are

$$\zeta_2 = 3.51; \ \sigma_\Phi = 2/3; \ C = 2; \ \kappa = 0.41 \tag{3.39}$$

The length scale of the modeled turbulence is

$$L = \frac{\sqrt{k}}{c_\mu^{1/4}\omega} \tag{3.40}$$

The von Karman length scale is

$$L_{vK} = \frac{\kappa S}{|U''|} \tag{3.41}$$

The scalar invariant of the strain rate tensor, S, is

$$S = \sqrt{2S_{ij}S_{ij}}; \ S_{ij} = \frac{1}{2}\left[\frac{\partial U_i}{\partial x_j} + \frac{\partial U_j}{\partial x_i}\right] \tag{3.42}$$

Finally, the second derivative can be calculated using equation (3.43) for a three-dimensional flow field.

$$|U''| = \sqrt{\sum_{(i)}\left(\frac{\partial^2 U_i}{\partial x_j\partial x_j}\right)^2} \tag{3.43}$$

In order to control the high wave number damping, an upper limit placed on the von Karman length scale.

$$L_{vK} = \max\left(\frac{\kappa S}{|U''|}, C_s\Delta\sqrt{\frac{\kappa\zeta_2}{(\beta/c_\mu) - \alpha}}\right) \tag{3.44}$$

Δ is the grid cell size, which is calculated using the control volume size (Ω_{cv}).

28

$$\Delta = \Omega_{CV}^{1/3} \tag{3.45}$$

This limiter also helps to limit the equilibrium eddy viscosity. If a balance is assumed between the production and destruction of turbulent kinetic energy, the equilibrium eddy viscosity can be calculated as

$$\mu_t^{eq} = \rho \left(\sqrt{\left((\beta/c_\mu) - \alpha \right) / (\kappa \zeta_2)} L_{vK} \right)^2 S \tag{3.46}$$

The goal of the limiter is to ensure that the equilibrium eddy viscosity remains larger then LES subgrid-scale eddy viscosity.

$$\mu_t^{eq} \geq \mu_t^{LES} \tag{3.47}$$

3.2. Transition Modeling using Intermittency

In addition to turbulence models, models for predicting the transition from laminar to turbulent flow are also required in order to accurately simulate many different types of flow. For a transition model to be useful for CFD, it must not require excessive computations and it must be compatible with the solution methods currently in use. The transition predictions should also be accurate for as many different types of flows as possible. All of these are similar to the requirements for a good turbulence model.

Two previously developed methods for predicting transition are stability theory equations, which involve solving stability equations in the streamwise direction in order to determine where transition begins (Michel, 1951), (Eppler, 1978), and the e^n method, which uses empirical correlations (van Ingen, 2008), (Smith & Gramberoni, 1956). Neither of these methods will work with current CFD methods. Both methods require the mean flow field to be solved before they can be used to predict transition (Suzen, Huang, Hultgren, & Ashpis, 2001).

Some work has also been done to use low-Reynolds number turbulence models in order to predict the transition. In most cases, the models fail to accurately predict both the transition location and length of transition. Westin and Henkes (1997) provide a comparison between the results from different turbulence models and the T3-series of transitional flow experiments (Westin & Henkes, 1997) (Savill, 1993). Another method to predict transition is the concept of intermittency (γ) which can be used to blend the laminar and turbulent regions of a flow together. This concept provides the backbone of the transition model used in the current research.

3.2.1. Transition Model Development

One of the earliest studies of intermittency was conducted by Dhawan and Narasimha (1958). They examined the boundary layer during transition on a flat plate. From those results, they were able to propose a generalized intermittency function (Dhawan & Narasimha, 1958). Chen and Thyson (1971) furthered this work by developing an intermittency function for an axisymmetric body which could be reduced to match the intermittency function of Dhawan and Narasimha for a flat plate (Chen & Thyson, 1971). Further improvements based on the previous work were published by Solomon, Walker, and Gostelow (1995). They developed a new method for calculating the intermittency based on the local pressure gradients within the transitional boundary layer. Their model uses experimental correlations to adjust turbulent spot growth parameters (Solomon, Walker, & Gostelow, 1995).

Steelent and Dick (1996) developed an intermittency transport equation which they coupled with two sets of conditioned Navier-Stokes equations. In order to model the turbulent portion of the flow, they used the k-ε turbulence model. Their intermittency distribution matched with intermittency distribution of Dhawan and Narasimha (1958). This method worked for different pressure gradients; however, the second set of Navier-Stokes equations made it

30

incompatible with common CFD methods. The other downside to their intermittency transport

equation is that it only predicted streamwise variation in intermittency, ignoring any possible

cross-stream variation (Steelent & Dick, 1996).

Another variation for the transport of intermittency was proposed by Cho and Chung

(1992). They developed a k-ε-γ turbulence model which was tested with various free shear

flows. They added a third differential equation for the transport of intermittency to the two other

equations from the standard k-ε turbulence model. This resulted in an excellent agreement

between the intermittency factor and the comparable experimental data (Cho & Chung, 1992).

Further improvements were made by Suzen and Huang (1999). They proposed a new

transport model that combined aspects of both Steelent and Dick's (1996), and Cho and Chung's

(1992) models. This allowed the new model to reproduce Dhawan and Narasimha's (1958)

intermittency distribution in the streamwise direction as well as matching the variation in the

cross-stream direction. By blending the older models, the goal was to be able to predict

transition for a wide variety of flows. The intermittency for this model is incorporated into the

calculations by multiplying the eddy viscosity from the turbulence model calculations as shown

in Equation (3.48).

$$\mu_t^* = \gamma \mu_t \qquad\qquad (3.48)$$

Including the intermittency with the eddy viscosity leads to a much simpler solution process that

can used with existing CFD codes, as opposed to some of the previous methods which required

solving multiple coupled Navier-Stokes equations (Suzen & Huang, 1999). This model has been

validated against the T3- series experiments of Savill (1993) and the low-pressure turbine

experiments of Simon, Qui, and Yuan (2000).

Suzen and Huang's transition model showed that intermittency could be used to predict transition for a variety of different flow conditions. The γ-Re_θ transition model further improves on the previous models (Suzen & Huang, 2005). Like the previous models, a transport equation for intermittency is used. In addition, there is also a transport equation for the transition onset momentum thickness Reynolds number. This second transport equation helps capture the non-local influence of the turbulence intensity as well combining the empirical correlation with the transition onset criteria in the intermittency equation. The model is coupled with the SST turbulence model and serves as the switch to turn on the turbulence production term as the flow moves past the transition location (Menter & Langtry, 2012). Because this method uses only local variables, it is well suited for the parallel Navier-Stokes solvers used in many CFD codes.

The current formulation for the γ-Re_θ transition model combines locally formulated transport equations with experimental correlations. The transition to turbulence is triggered by the vorticity or strain rate Reynolds number, which is defined as

$$\mathrm{Re}_v = \frac{\rho y^2}{\mu}\left|\frac{\partial u}{\partial y}\right| = \frac{\rho y^2}{\mu} S \tag{3.49}$$

Where y is the distance to the wall and S is the shear strain rate. Since all variables are local quantities, the vorticity Reynolds number can be easily calculated by parallel solvers. A scaled vorticity Reynolds number profile in a Blasius boundary layer is shown in Figure 3.1.
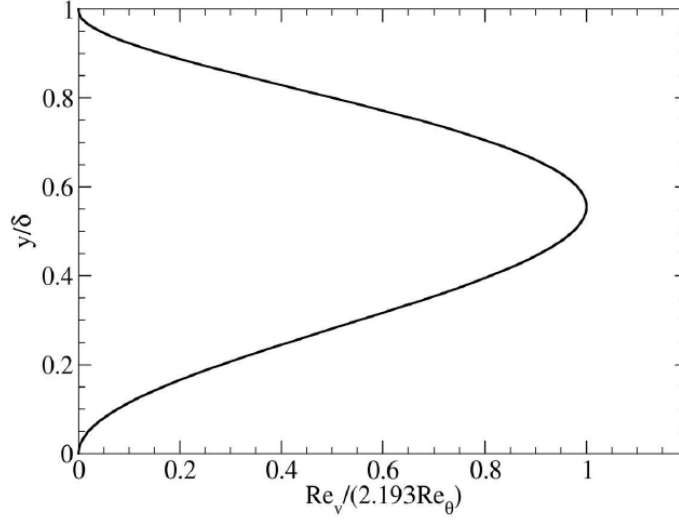
Figure 3.1. Re_v profile for Blasius boundary layer (Menter & Langtry, 2012)

The scaling is done so that the maximum vorticity Reynolds number in the boundary layer is one. This can be achieved by dividing the Blasius velocity profile by the corresponding momentum thickness Reynolds number and a constant of 2.193. The relationship can be shown as

$$\text{Re}_\theta = \frac{\max\left(\text{Re}_v\right)}{2.193} \qquad (3.50)$$

The relative error between Re_θ and Re_v is usually less than 10% for moderate pressure gradients, which is not a problem for most calculations (Menter & Langtry, 2012).

3.2.2. γ-Re_θ Model Equations

The γ-Re_θ transition model is based on two transport equations governing the transport of intermittency (γ) and the transport of the transition momentum thickness Reynolds number (Re_θ). This section will explain the mathematical formulation of these transport equations and how they are coupled with the SST turbulence model in order to model transitional flows (Menter & Langtry, 2012).

The transport equation for the intermittency (γ), is given as

$$\frac{\partial\left(\rho\gamma\right)}{\partial t}+\frac{\partial\left(\rho U_j\gamma\right)}{\partial x_j}=P_\gamma-E_\gamma+\frac{\partial}{\partial x_j}\left[\left(\mu+\frac{\mu_t}{\sigma_f}\right)\frac{\partial\gamma}{\partial x_j}\right]\qquad(3.51)$$

where the transition sources are defined as

$$P_{\gamma1}=F_{length}c_{a1}\rho S\left[\gamma F_{onset}\right]^{0.5}\left(1-c_{e1}\gamma\right)\qquad(3.52)$$

S is the strain rate magnitude. The length of transition is controlled by an empirical correlation (F_{length}). E_γ is the destruction/relaminarization source, which is defined as

$$E_\gamma=c_{a2}\rho\Omega\gamma F_{turb}\left(c_{e2}\gamma-1\right)\qquad(3.53)$$

where Ω is the vorticity magnitude. The transition onset is controlled by vorticity Reynolds number (Re_v) and the following functions

$$Re_V=\frac{\rho y^2 S}{\mu}\qquad(3.54)$$

$$F_{onset1}=\frac{Re_v}{2.193\,Re_{\theta c}}\qquad(3.55)$$

$$F_{onset2}=\min\left(\max\left(F_{onset1},F_{onset1}^4\right),2.0\right)\qquad(3.56)$$

$$R_T=\frac{\rho k}{\mu\omega}\qquad(3.57)$$

$$F_{onset3}=\max\left(1-\left(\frac{R_T}{2.5}\right)^3,0\right)\qquad(3.58)$$

$$F_{onset}=\max\left(F_{onset2}-F_{onset3},0\right)\qquad(3.59)$$

$Re_{\theta c}$ is the critical Reynolds number where intermittency begins to increase in the laminar boundary layer (Menter & Langtry, 2012). $\tilde{R}e_{\theta t}$ is the transition momentum thickness Reynolds number. The $Re_{\theta c}$ and F_{length} correlations are both a function of $\tilde{R}e_{\theta t}$.

The correlation for F_{length} based on $\tilde{R}e_{\theta t}$ was developed using the T3B, T3A, T3A-(Savill, 1993) and the Schubauer and Klebanoff (1955) test cases and is defined as

$$
F_{length} =
\begin{cases}
\left[398.198*10^{-1}+\left(-119.270*10^{-4}\right)\tilde{Re}_{\theta t}+\left(-132.567*10^{-6}\right)\tilde{Re}_{\theta t}^{2}\right], & \tilde{Re}_{\theta t}<400 \\
\left[263.404+\left(-123.939*10^{-2}\right)\tilde{Re}_{\theta t}+\left(119.548*10^{-5}\right)\tilde{Re}_{\theta t}^{2}+\left(-101.695*10^{-8}\right)\tilde{Re}_{\theta t}^{3}\right], & 400\leq\tilde{Re}_{\theta t}<596 \\
\left[0.5-\left(\tilde{Re}_{\theta t}-596.0\right)*\left(3.0*10^{-4}\right)\right], & 596\leq\tilde{Re}_{\theta t}<1200 \\
\left[0.3188\right], & 1200\leq\tilde{Re}_{\theta t}
\end{cases}
\tag{3.60}
$$

The correlation between $Re_{\theta c}$ and $\tilde{R}e_{\theta t}$ is defined as

$$
Re_{\theta c}=
\begin{cases}
\left[\tilde{Re}_{\theta t}-\left(\begin{array}{l}396.035*10^{-2}+\left(-120.656*10^{-4}\right)\tilde{Re}_{\theta t}+\left(868.230*10^{-6}\right)\tilde{Re}_{\theta t}^{2} \\ +\left(-696.506*10^{-9}\right)\tilde{Re}_{\theta t}^{3}+\left(174.105*10^{-12}\right)\tilde{Re}_{\theta t}^{4}\end{array}\right)\right] & \tilde{Re}_{\theta t}\leq1870 \\
\left[\tilde{Re}_{\theta t}-\left(593.11+\left(\tilde{Re}_{\theta t}-1870.0\right)*0.482\right)\right] & \tilde{Re}_{\theta t}>1870
\end{cases}
\tag{3.61}
$$

Equation (3.62) lists all the constants for the intermittency equation.

$$
C_{a1}=2.0;\quad C_{e1}=1.0;\quad C_{a2}=0.06;\quad C_{e1}=50.0;\quad \sigma_{f}=2.0;
\tag{3.62}
$$

If a flow is transitioning due to separation, the following modification can be used

$$
\gamma_{sep}=\min\left(s_{1}\max\left[0,\left(\frac{Re_{\upsilon}}{3.235\,Re_{\theta c}}\right)-1\right]F_{reattach},2\right)F_{\theta t}
\tag{3.63}
$$

$$
F_{reattach}=e^{-\left(\frac{R_{T}}{20}\right)^{4}}
\tag{3.64}
$$

$$
\gamma_{eff}=\max\left(\gamma,\gamma_{sep}\right)
\tag{3.65}
$$

$$
s_{1}=2
\tag{3.66}
$$

The equation governing the transport of the transition momentum thickness Reynolds number $\tilde{R}e_{\theta t}$ is

$$
\frac{\partial\left(\rho\tilde{Re}_{\theta t}\right)}{\partial t}+\frac{\partial\left(\rho U_{j}\tilde{Re}_{\theta t}\right)}{\partial x_{j}}=P_{\theta t}+\frac{\partial}{\partial x_{j}}\left[\sigma_{\theta t}\left(\mu+\mu_{t}\right)\frac{\partial\tilde{Re}_{\theta t}}{\partial x_{j}}\right]
\tag{3.67}
$$

35

where the source term ($P_{\theta t}$), is defined as

$$P_{\theta t} = c_{\theta t} \frac{\rho}{t} \left(\mathrm{Re}_{\theta t} - \tilde{\mathrm{Re}}_{\theta t} \right) \left(1.0 - F_{\theta t} \right) \tag{3.68}$$

$$t = \frac{500 \mu}{\rho U^2} \tag{3.69}$$

The time scale (t) is required for dimensional reasons. The blending function ($F_{\theta t}$) is used to turn

the source term on and off in the boundary layer. It is zero in the freestream and one in the

boundary layer, which allows $\tilde{Re}_{\theta t}$ to diffuse from the freestream. The blending function is

formulated as

$$F_{\theta t} = \min \left(\max \left[F_{wake} e^{-\left(\frac{y}{\delta} \right)^4}, 1.0 - \left(\frac{\gamma - 1/c_{e2}}{1.0 - 1/c_{e2}} \right)^2 \right], 1.0 \right) \tag{3.70}$$

where

$$\delta = \frac{50 \Omega y}{U} \delta_{BL} ; \quad \delta_{BL} = \frac{15}{2} \theta_{BL} ; \quad \theta_{BL} = \frac{\tilde{Re}_{\theta t} \mu}{\rho U} \tag{3.71}$$

$$F_{wake} = e^{-\left(\frac{\mathrm{Re}_{\omega}}{1E+5} \right)^2} ; \quad \mathrm{Re}_{\omega} = \frac{\rho \omega y^2}{\mu} \tag{3.72}$$

The constants for the $\tilde{Re}_{\theta t}$ equation are

$$c_{\theta t} = 0.03 ; \quad \sigma_{\theta t} = 2.0 ; \tag{3.73}$$

The onset of transition is calculated with an empirical correlation based on the following two

parameters

$$\lambda_{\theta} = \frac{\rho \theta^2}{\mu} \frac{dU}{ds} \tag{3.74}$$

$$Tu = 100 \frac{\sqrt{2k/3}}{U} \tag{3.75}$$

36

For numerical stability, the acceleration parameter (λ_θ), the turbulence intensity (Tu), and the empirical correlation should be held within the following limits

$$-0.1 \leq \lambda_\theta \leq 0.1; \quad Tu \geq 0.027; \quad \mathrm{Re}_{\theta t} \geq 20; \tag{3.76}$$

Finally, the γ-Re$_\theta$ transition model can be combined with the SST turbulence model by replacing the original production (P_k) and destruction (D_k) terms with new terms based on the intermittency.

$$\frac{\partial}{\partial t}(\rho k) + \frac{\partial}{\partial x_j}(\rho u_j k) = \tilde{P}_k - \tilde{D}_k + \frac{\partial}{\partial x_j}\left[(\mu + \sigma_k \mu_t)\frac{\partial k}{\partial x_j}\right] \tag{3.77}$$

$$\tilde{P}_k = \gamma_{eff} P_k \tag{3.78}$$

$$\tilde{D}_k = \min\left(\max\left(\gamma_{eff}, 0.1\right), 1.0\right) D_k \tag{3.79}$$

In order to achieve the best result with this model, the y+ value of the first grid point away from a wall should be approximately one. If it is significantly higher (>5), the transition location will shift upstream (Menter & Langtry, 2012).

3.2.3. γ-Re$_\theta$ Model Validation

In order to show that a transition model is accurate, it needs to be validated against a wide variety of different types of flows. This should include simple flows, such as flat plate experiments, as well as more complex flows that are similar to the type of flow of interest. For this research, the flow of interest is a gas turbine stator vane. Some of the experiments that have been run are listed here.

- Flat plate experiments (Schubauer & Klebanoff, 1955)

- ERCOFTAC benchmarks (Savill, 1993)

- Low-pressure turbine experiments (Simon, Qiu, & Yuan, 2000)

- PAK-B blade experiments (Lake, King, & Rivir, 1999), (Huang, Corke, & Thomas, 2003), (Volino, 2002)

- Unsteady wake-blade interactions (Kaszeta, Simon, & Asphis, 2001), (Stieger, Hollis, & Hodson, 2004)

A comparison between the computational results for the γ-Re$_\theta$ transition model and the listed experiments have been presented by Suzen and Huang (2005), Menter et al. (2006), and Menter and Langtry (2012). For all of these cases, there is a good agreement between the computational and experimental results. All of these cases help to validate the γ-Re$_\theta$ transition model and show that it can provide accurate transition predictions.

4. UND COMPRESSIBLE FLOW EXPERIMENTS

This section covers the compressible flow wind tunnel located at the University of North Dakota. The wind tunnel was used for the experimental testing of a first stage stator vane. The experiments were conducted to determine the aerodynamic loading of the vane and the effects of turbulence level and transitional flow on the heat transfer from the vane's surface.

4.1. Wind Tunnel Characteristics

The wind tunnel at University of North Dakota is constructed using a positive displacement rotary blower, also known as a Roots blower. The wind tunnel can be run at a steady state condition, and the pressure ratio and the flow speed can be varied independently. This is different from the most common type of transonic wind tunnel, which utilize a blow down technique. The design allows the wind tunnel to achieve exit chord Reynolds numbers ranging from 90,000 to 1,000,000. The exit Mach numbers can range from 0.5 up to 0.9 (Mihelish & Ames, 2013).

In order to dampen the pressure oscillations from the blower, insulated damping tanks are place both upstream and downstream. Due to the size of the tanks, insulation is necessary to reduce the thermal lag within the system. After the outlet damping tank is the flow conditioning unit. This helps to smooth out the flow and generate a uniform flow field. Between the flow conditioning unit and the test section, there is a nozzle. The nozzle can be a smooth contraction which is used for low turbulence tests. The nozzle can also be swapped out for a mock combustor in order to generate a high turbulence flow field within the test section. At the exit of the test section is a traversing system which is used to take pressure measurements within the flow field. Finally, the flow is routed back around to the damping tank at the inlet to the blower. A full schematic of the wind tunnel is shown in Figure 4.1.
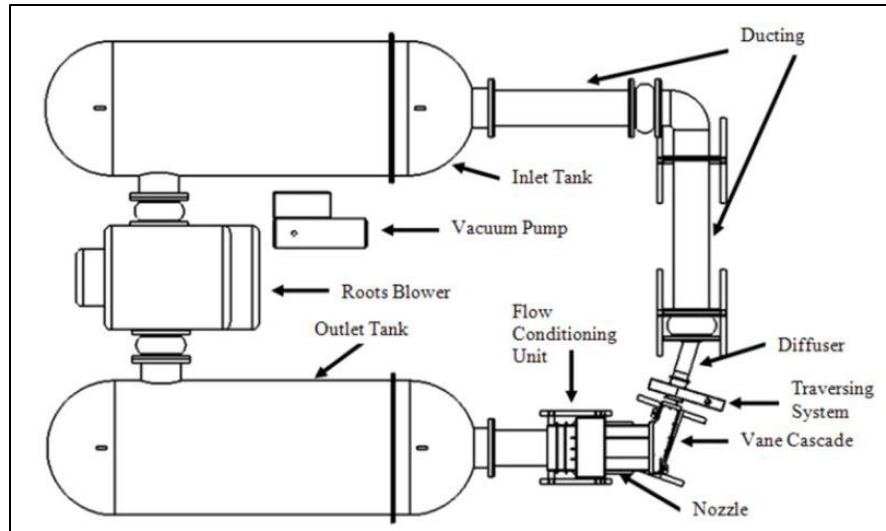
Figure 4.1. Schematic of closed-loop high-speed low Reynolds number flow facility with linear vane cascade test section (Mihelish & Ames, 2013)

4.2. Compressible Flow Vane Cascade Experiments

The compressible flow vane cascade tested the first stage stator vane from a high-altitude UAV. The experimental vane has true chord length of 12.1 cm, which is 2.8 times scale, and an axial chord length of 5.93 cm. The cascade is shown in Figure 4.2 and consists of four vanes. The top and bottom vanes are only partial vanes with the missing portions containing bleed valves. These valves were used to adjust the incoming flow and ensure consistent flow around all the vanes. The third vane from the bottom was the instrumented vane from which all vane data was collected. At one-quarter axial chord upstream and one-quarter axial chord downstream from the vanes are static pressure wall taps. These were used to measure the variation in the flow field.

Two separate experiments were run with the cascade. The first experiment examined the aerodynamic losses within the cascade. The instrumented vane for this experiment had 40 mid span static pressure taps to measure the pressure around the vane's surface. For this experiment, four different Reynolds numbers, 90,000, 180,000, 360,000, and 720,000, and three different exit

Mach numbers, 0.7, 0.8, and 0.9, were tested. For each condition, a high (9%) and low (0.8%)

turbulence condition were also tested. In total, 24 different aerodynamic cases were examined.

Each case provided the upstream and downstream static pressure along the wall, the pressure

loading on the vane, and the loss contours at the exit of the cascade.
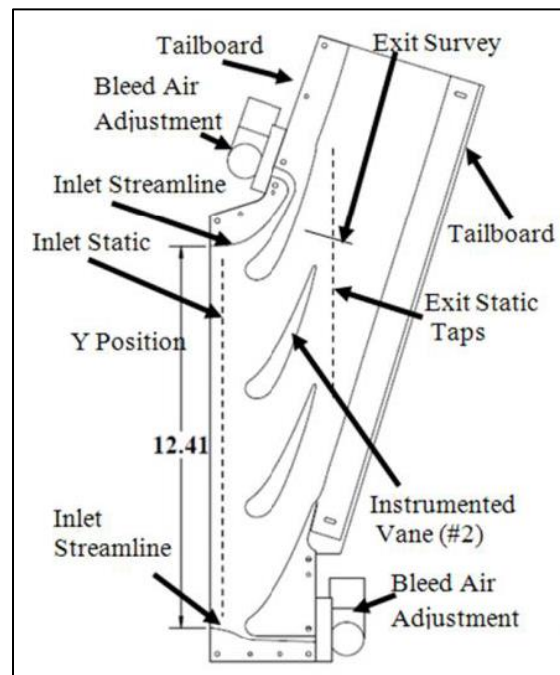
Figure 4.2. Schematic of linear cascade test section (Mihelish & Ames, 2013)

The second experiment examined the heat transfer from the vane surface. The

instrumented vane for this experiment had 40 fine wire type K thermocouples cast into the

surface. The surface was then covered Inconel foil which was used to apply a constant uniform

heat flux to the surface. Five different Reynolds numbers, 90,000, 180,000, 360,000, 720,000,

and 1,000,000, and three different exit Mach numbers, 0.7, 0.8, and 0.9 were tested. For each

condition, a high (9%) and low (0.8%) turbulence condition were also tested. Each case also

required a run with the unheated vane in order to determine the adiabatic wall temperature. In

total, 30 different heat transfer cases were examined.

5. METHODS OF CFD COMPUTATION AT NDSU

5.1. Hardware and Software Descriptions

All the computations for this project were completed on the Thunder cluster at the Center

for Computationally Assisted Science and Technology (CCAST), North Dakota State University.

The entire Thunder cluster contains 105 nodes and 3,040 processing cores with an estimated

peak performance of 150 TFLOPS (CCAST, 2018).   The CFD group within the Mechanical

Engineering Department has a condominium with priority access to 10 nodes and 200

processors. All the computations were completed on the Thunder cluster with either 100 or 200

processors. A picture of the Thunder cluster after renovations in 2018 is shown in Figure 5.1.
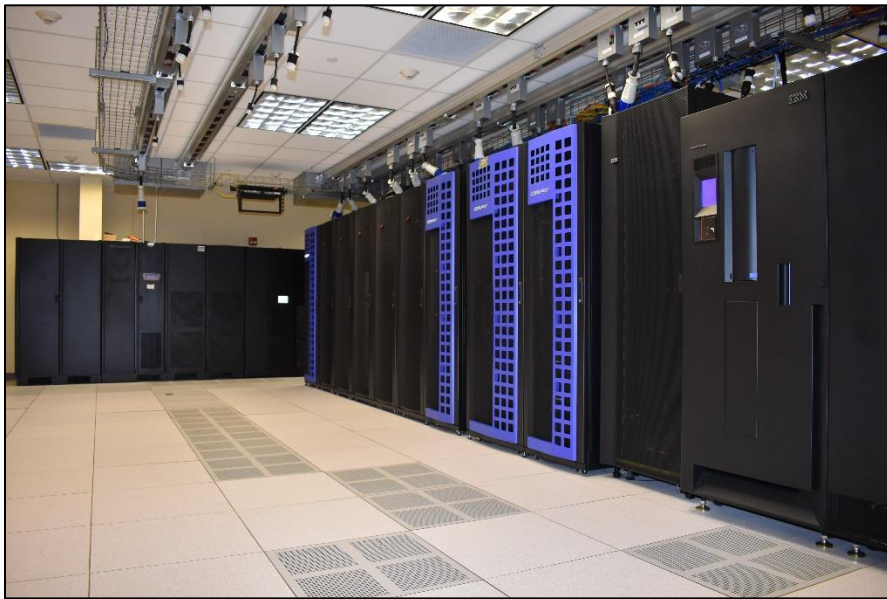
Figure 5.1. The Thunder cluster, photo courtesy of CCAST/NDSU

The geometry for the problem was modeled in Solidsworks. The meshes were built using

ANSYS Meshing. All the computations were completed using ANSYS CFX. ANSYS CFX is a

robust solver that was originally designed for use in simulating rotating machinery. It is also a

parallel solver code, which allows it to efficiently utilize all 200 processors available on the

Thunder Cluster. For both these reasons, ANSYS CFX is well suited for simulating the turbine

vanes examined for this thesis. All the turbulence and transition models used in this research are also implemented in ANSYS CFX. Post processing was completed using ANSYS CFD Post and Tecplot.

5.2. Flow Field Geometry and Mesh Generation

For the stator vane, 3D CAD models of the wind tunnel test section were provided by UND. These were used by Jamison Huber (Huber, 2013) to create the original flow field geometry and mesh for the CFD simulations. Additional adjustments to the mesh were completed by Alex Flage (Flage, 2015). The previous geometry with the low turbulence nozzle is shown in Figure 5.2.
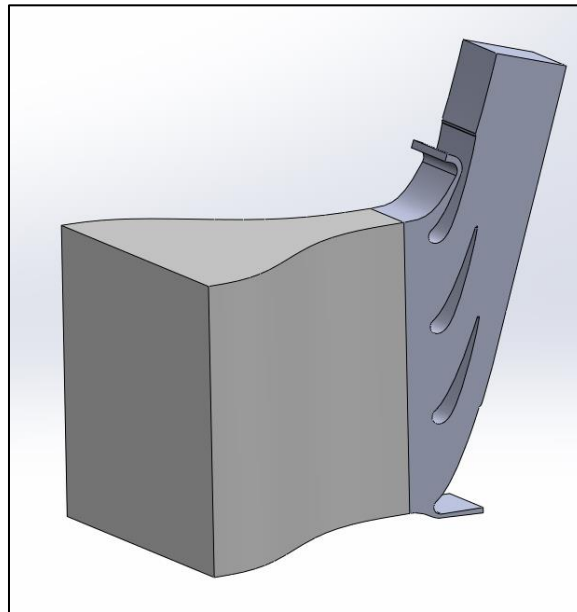
Figure 5.2. Previous low turbulence compressible flow geometry (Flage, 2015)

Additional modifications were made to the simulation flow field geometry for the current research in order to improve the final simulation results. In the original geometry, sonic flow was occurring in the suction and pressure bleeds, leading to a choked condition. The updated geometry reduced the length of the both bleeds, eliminating the diverging portion near the bleed outlets. The main outlet was also changed. Instead of having the outlet perpendicular to the exit

flow, the boundary was changed so it was parallel with vane cascade. The updated high and low

turbulence geometries are shown in Figure 5.3.
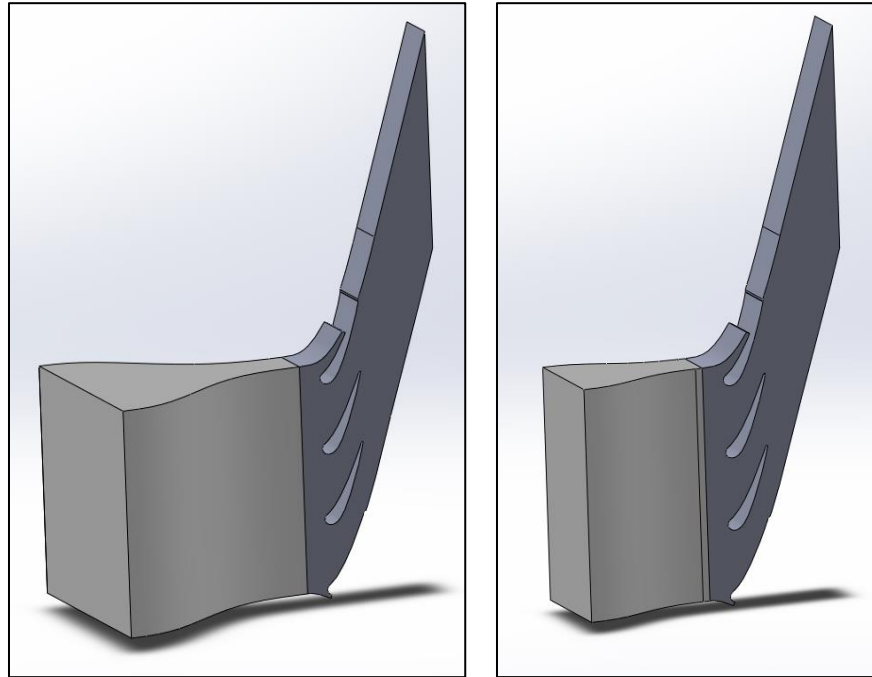
Figure 5.3. Final compressible flow vane cascade geometry for low (left) and high (right)
turbulence settings

The mesh for the updated geometry was further refined from the older mesh used by

(Flage, 2015). The original mesh had a body sizing of 6 mm throughout the domain and a single

body of influence around the vanes with a sizing of 1.5 mm. For the new mesh, the body sizing

was left the same. The old body of influence was split into three separate parts. The two bleeds

were each given their own body of influence with a sizing of 0.5 mm, allowing the mesh density

in those areas to be increased. The middle section of the original body of influence was left at

the 1.5 mm sizing it previously had. A new body of influence was also added to the outlet of the

geometry with a sizing of 3 mm to give increased mesh resolution in that area as well. The

bodies of influence used in generating the mesh are shown in Figure 5.4.
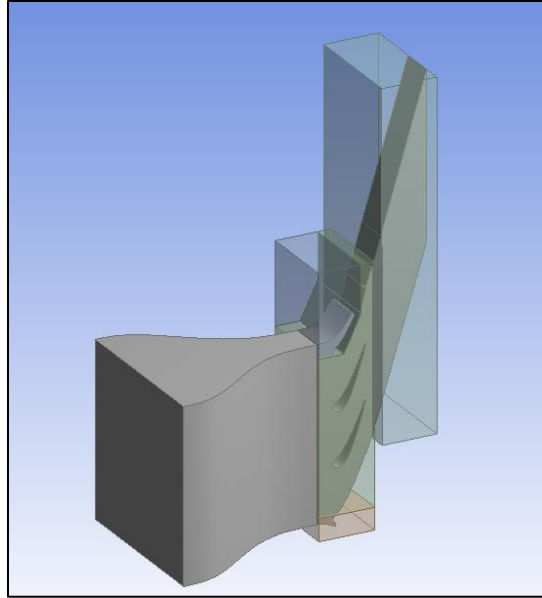
Figure 5.4. Bodies of influence used for mesh generation

Additional changes also included adding wall sizings to the sides, top, and bottom of the domain in order to partially capture boundary layer growth as air travels through the domain. The side walls were given a face sizing of 0.8 mm and the top and bottom were given sizings of 1.5 mm. All of the remaining mesh parameters were left unchanged from the previous mesh, with a face sizing on the vane surfaces of 0.75 mm and a first layer height of 1.5×10^{-6} m for the vane inflation (Flage 2015). The first layer height for the inflation layer around the vanes was left unchanged. Different first layer heights were tested during mesh refinement, but the current first layer height, which provided a y+ around 0.3, was shown to provide the best results for the heat transfer simulations. A first layer y+ value near one provides the best results with the SST turbulence model (Menter, 1994). The mesh parameters for the low turbulence and high turbulence geometries were the same. The low turbulence mesh was slightly larger due to the larger inlet nozzle. The mesh is shown in Figures 5.5 and 5.6.
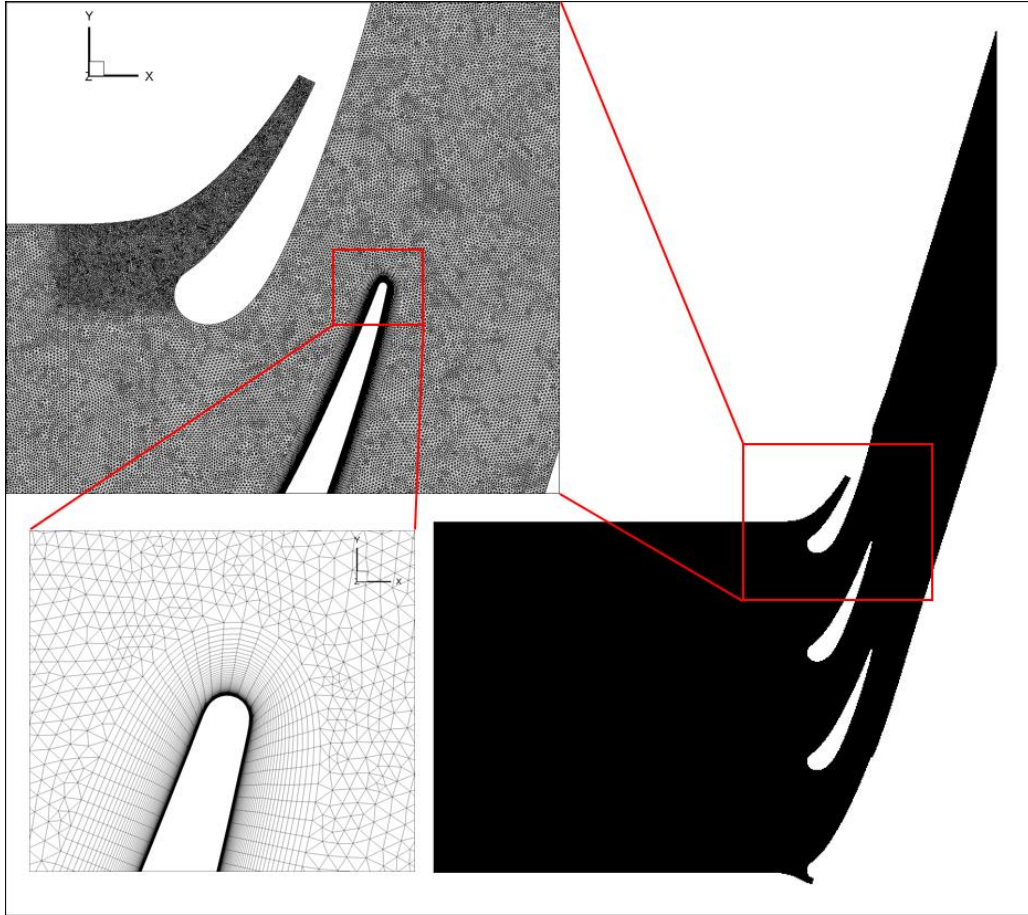
Figure 5.5. Compressible flow vane mesh side view with vane zoomed view
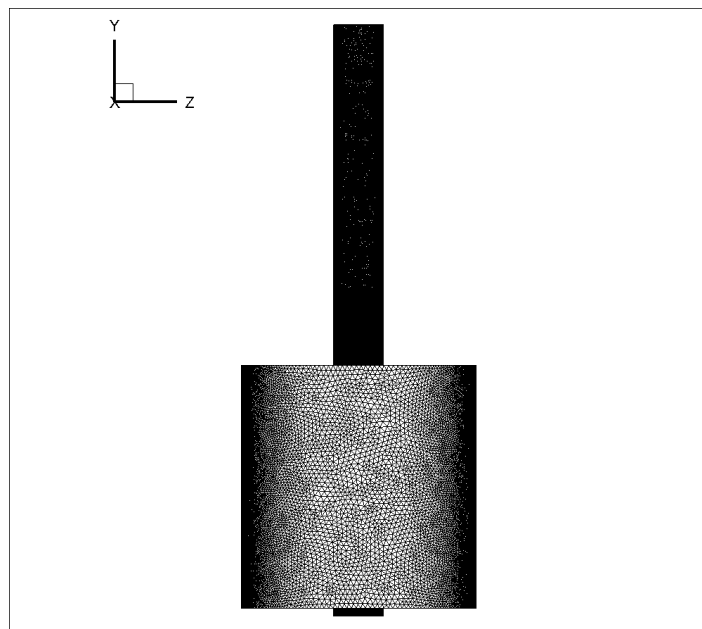
Figure 5.6. Compressible flow vane mesh inlet view

Two different studies were completed with this geometry, an aerodynamic loading study and a heat transfer study. For both studies, three different Mach numbers were tested: 0.7, 0.8, and 0.9. For the aerodynamic loading study, four different Reynolds numbers were tested: 90,000, 180,000, 360,000, and 720,000. The heat transfer study added a fifth Reynolds number of 1,000,000. Two different turbulence levels were also tested, a high turbulence (HT) setting of 9% and a low turbulence (LT) setting of 0.8%. In total, 23 different aerodynamic loading cases and 27 different heat transfer cases were run. All the cases are listed in Tables 5.1 and 5.2.

Table 5.1. Aerodynamic loading study cases

Mach Number	Turbulence Level	Reynolds Numbers
0.7	Low Turbulence	90K, 180K, 360K, 720K
	High Turbulence	90K, 180K, 360K, 720K
0.8	Low Turbulence	90K, 180K, 360K
	High Turbulence	90K, 180K, 360K, 720K
0.9	Low Turbulence	90K, 180K, 360K, 720K
	High Turbulence	90K, 180K, 360K, 720K

Table 5.2. Heat transfer study cases

Mach Number	Turbulence Level	Reynolds Numbers
0.7	Low Turbulence	90K, 180K, 360K, 720K, 1000K
	High Turbulence	90K, 180K, 360K, 720K, 1000K
0.8	Low Turbulence	90K, 180K, 360K, 1000K
	High Turbulence	90K, 180K, 360K, 720K, 1000K
0.9	Low Turbulence	180K, 360K, 720K, 1000K
	High Turbulence	180K, 360K, 720K, 1000K

5.3. Boundary Conditions and Setup Parameters

The boundary conditions for the simulations were based as much as possible on the experimental data collected during the experiments at UND. The following list of variables were directly measured during the experiments:

- Total Temperature

- Total Pressure

- Static Pressure

- Static Temperature

These variables were measured at a quarter chord upstream, downstream, and on the surface of the vane. From these variables, the following quantities can be calculated:

- Reynolds Number

- Mach Number

- Velocity

In order to run the simulations in ANSYS CFX, the following variables are needed as inputs for the boundary conditions:

- Reference (Domain) Pressure

- Inlet Relative Pressure

- Inlet Total Temperature

- Turbulence Kinetic Energy (k)

- Turbulent Eddy Frequency (ω)

- Outlet Relative Pressure

- Outlet Static Temperature

- Suction and Pressure Bleed Relative Pressure

- Heat Flux on Heated Vane Surface

The boundaries for the simulation are shown in Figure 5.7. The domain pressure for each simulation was set as the outlet static pressure from the experiment. The inlet relative pressure was set by subtracting the experimental outlet static pressure from the experimental inlet total pressure. The inlet total temperature was set the same as the experimental total temperature.
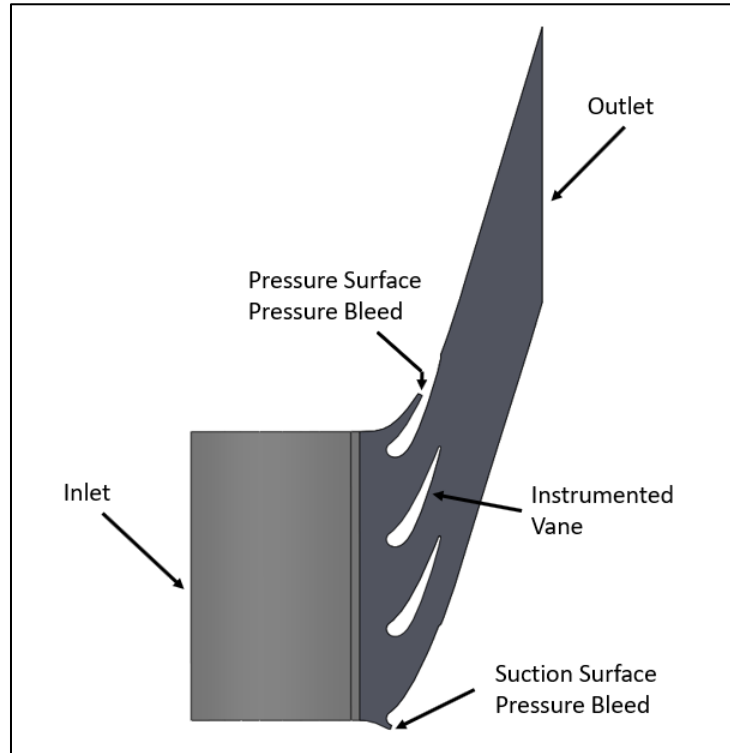
Figure 5.7. Boundaries for the CFD simulation

The outlet pressure for the simulations was originally set as zero relative pressure in order to match the outlet static pressure measured in the experiment. Due to the difference in locations between the static taps at a quarter axial chord downstream and the simulation outlet, the zero relative pressure resulted in too low of a Mach number at a quarter chord downstream of the vane cascade. The outlet pressure was iteratively adjusted. By lowering the outlet pressure, the downstream static pressure profile and the pressure profile on the vane surface were matched.

No information was available on the pressures at the suction and pressure bleeds from the experiment. In order to get a uniform flow field, the bleed pressures were adjusted so the pressure distributions on the top and bottom partial vanes were similar to pressure distribution from the instrumented vane.

The turbulence intensities for the experiment were reported at a quarter chord upstream from the vane cascade. These were converted into turbulent kinetic energy and the governing equation for the turbulent kinetic energy was simplified and solved in order to estimate the required turbulent kinetic energy at the domain inlet. The estimation did not work, because the decay rate of the turbulent kinetic energy was lower for the simulations then it was for the estimation. The result of the estimation was that the high turbulence simulations were experiencing a turbulence intensity of ~12.5% rather than the 9% reported from the experiments and the low turbulence cases were experiencing a turbulence intensity of ~2.5% rather than 0.8%. In order to correct the turbulence level, the inlet turbulent kinetic energy was iteratively lowered. The iteration procedure helped to match the turbulence intensity between the simulation and experiment. The low turbulence cases showed excellent agreement for the heat transfer results; however, the high turbulence cases were still transitioning too early.

For the high turbulence cases, lower turbulence intensities were tested in order to match the transition on the suction surface. At various turbulence intensities between 6% and 7.5%, the high turbulence cases showed excellent agreement between the simulation and experimental results. Although the results were much better, the lower turbulence intensities were significantly different than the reported turbulence intensities and could not be justified. In the final reported results for the high turbulence cases, the turbulence intensity was left as 9% at a quarter axial chord upstream of the vane cascade unless otherwise specified.

All of the simulations used the SST turbulence model and the γ-Re_θ transition model. For the high turbulence cases, the curvature correction model for the SST turbulence model was also activated. The advection scheme and turbulence numerics were both set to high resolution to achieve the maximum possible accuracy. Most simulations achieved the final target RMS residual of 1e-6. There were a few simulations where one or more equations were not fully converged. In these cases, the conservation of mass solution either flat lined or showed small oscillations around 3e-6. In all cases, the final RMS residuals were below 4e-6. Air ideal gas was used as the simulation fluid within ANSYS CFX in order to properly model the fluid as compressible.

6. RESULTS AND DISCUSSION OF THE FIRST STAGE STATOR VANE

SIMULATIONS

Two different studies were conducted with the first stage stator vane, an aerodynamic

loading study and heat transfer study. The results at the vane surface for both studies are

presented in terms of the surface arc position (S) in meters. Zero S is the stagnation point on the

leading edge of the vane. Positive S corresponds to the lower, suction, surface of the vane, and

negative S is the upper, pressure, surface of the vane. The definition of the surface arc is shown

in Figure 6.1.
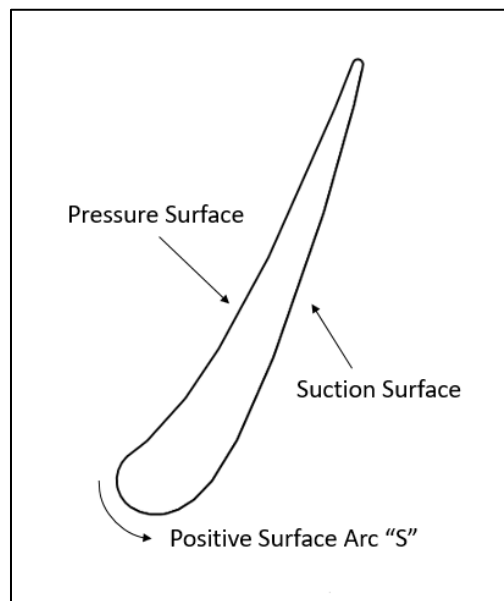
Figure 6.1. Vane surface arc definition

6.1. Aerodynamic Loading Study Results

The aerodynamic study consists of 23 different RANS steady state simulations. For all of

the aerodynamic cases, the upstream static pressure profiles from the experiments were measured

at a one-quarter axial chord upstream from the leading edge of the vanes. The downstream static

pressure profiles were measured at one-quarter axial chord downstream from the trailing edge

plane of the vanes. Both the upstream and downstream static pressure profiles from the

simulations were compared with the experimental pressure distributions. This was done to

ensure the simulations matched with the experimental conditions as closely as possible. Figure

6.2 shows the coordinate system and locations for measuring the static pressure profiles. Figure

6.3 shows the upstream and downstream static pressure profiles superimposed over the pressure

contour plot for the 360,000 Reynolds number and 0.8 Mach number case at high turbulence.

The pressure profile data was extracted from the computational domain along the vertical axis

for the individual pressure plots. From this, it can be seen where the pressure peaks and valleys

occur within the cascade.
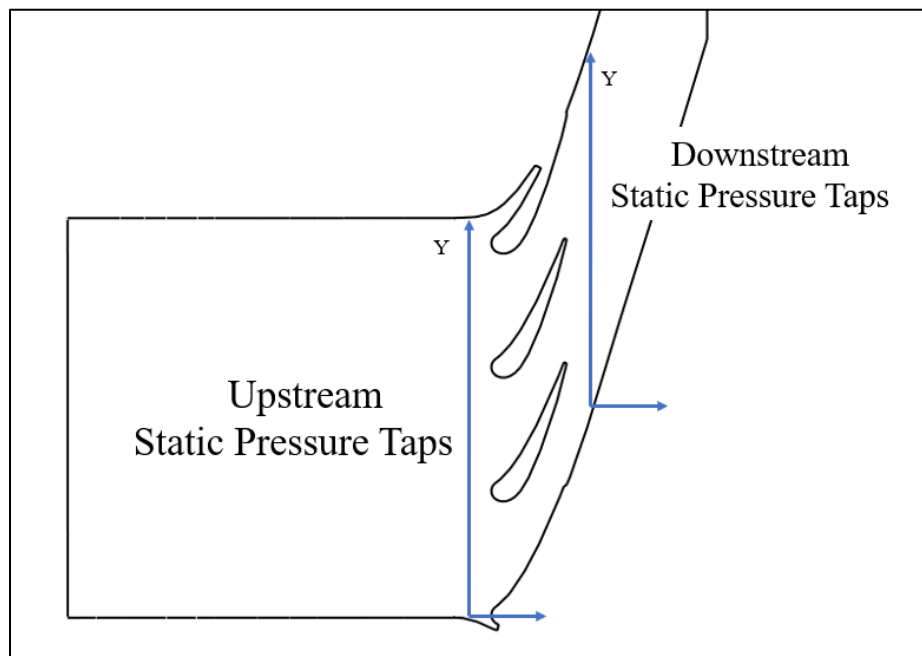
Figure 6.2. Static pressure tap locations and coordinate system

53
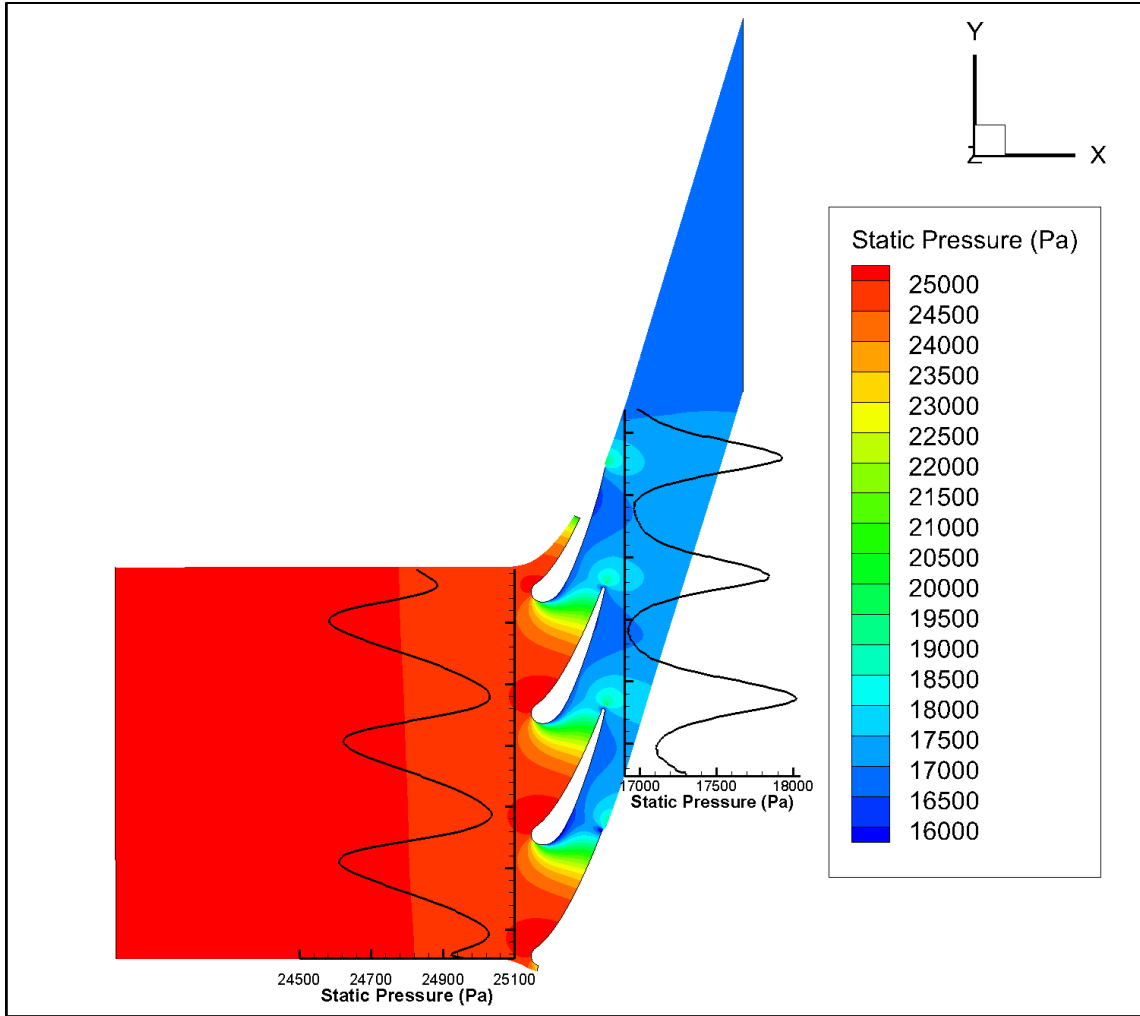
Figure 6.3. Static pressure contour plot for Re = 360,000, Ma = 0.8, and high turbulence

Figures 6.4 and 6.5 show the static pressure profiles at a quarter chord upstream of the

vane cascade. In all cases, the CFD results provided a close match to the experimental pressure

profiles. No special adjustments to the inlet boundary conditions were required to match the

upstream pressure profiles. The pressure and suction bleed pressure adjustments only had minor

effects on the very top and bottom of CFD pressure distributions.
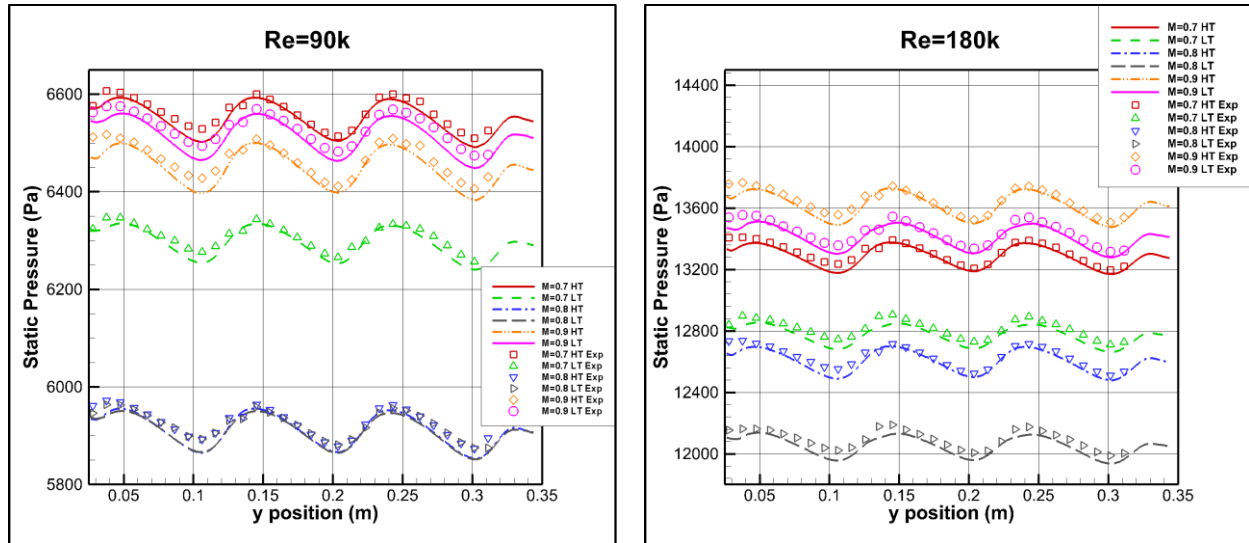
Figure 6.4. Upstream static pressure distributions for Re = 90,000 (left) and Re = 180,000 (right)
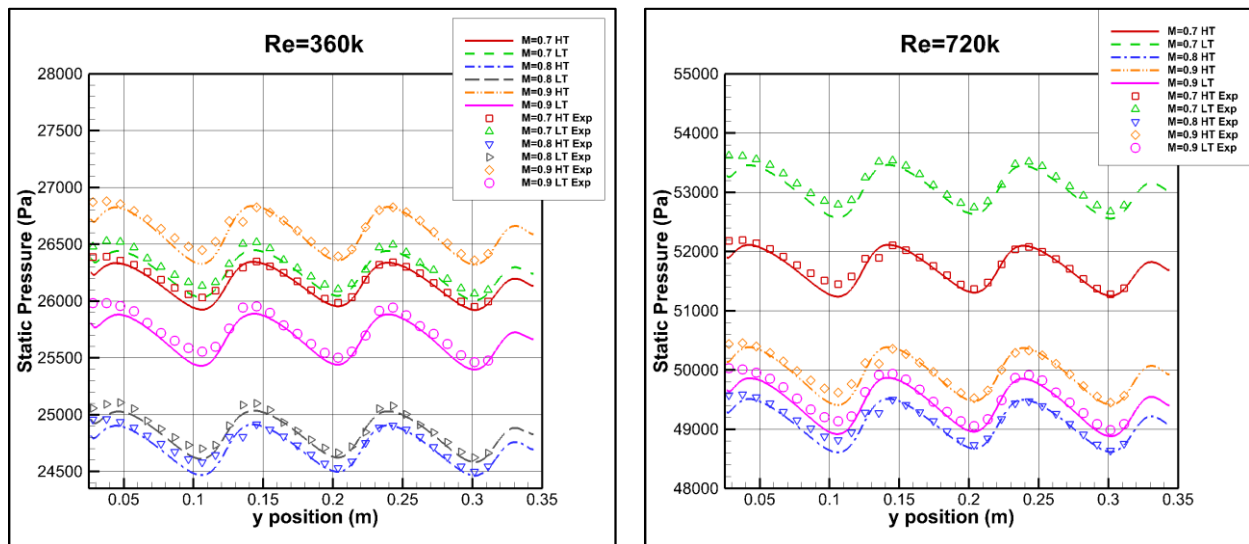
Figure 6.5. Upstream static pressure distributions for Re = 360,000 (left) and Re = 720,000 (right)

Pressure distributions at a quarter axial chord downstream on the vane cascade were used to adjust the cascade exit Mach number. The experimental pressure distributions showed a decreasing trend as you move vertically up the cascade. This was partially matched by the CFD results at the 90,000 and 180,000 Reynolds numbers shown in Figures 6.6. Although they both exhibited a downward trend it was not as steep as the experimental results. The CFD results for

the 360,000 and 720,000 Reynolds number cases did not follow the trend of the experimental data. Their pressure distributions remained more horizontal, showing no downward trend, shown in Figure 6.7. The exit pressure was matched near the highest pressure peak for all cases as this provided the best vane loading results.
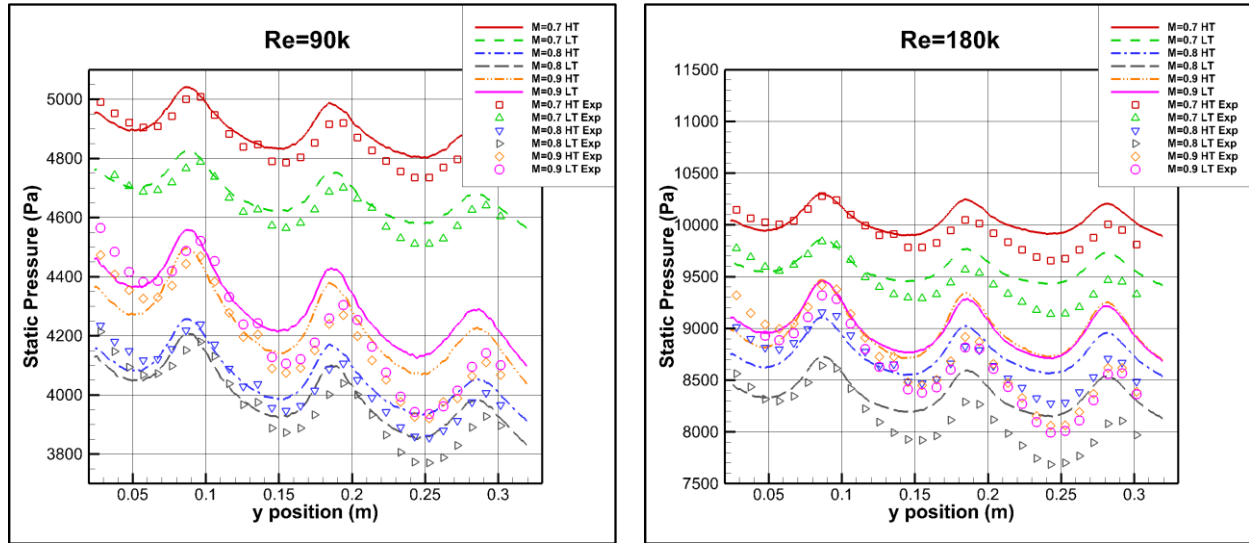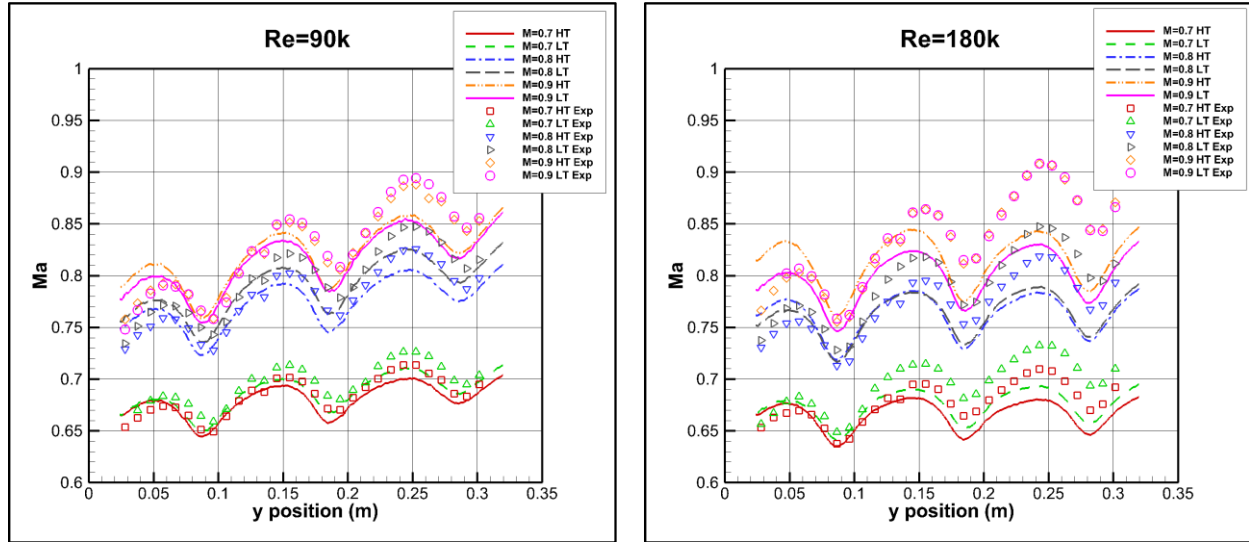

Figure 6.6. Downstream static pressure distributions for Re = 90,000 (left) and Re = 180,000 (right)
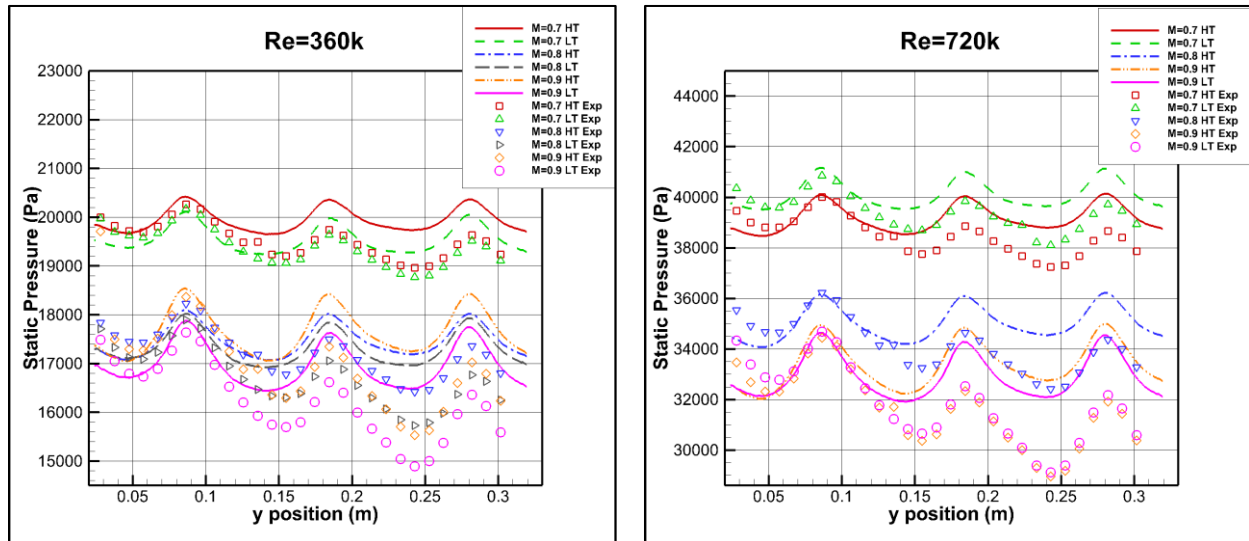
Figure 6.7. Downstream static pressure distributions for Re = 360,000 (left) and Re = 720,000 (right)

It is believed that that the downstream pressure profile discrepancy at the higher

Reynolds numbers is related to differences in the downstream turning angle. The turning angle

calculated at the same location as the downstream static pressure profiles can be seen in Figure

6.8. For the 90,000 and 180,000 Reynolds number cases, the turning angle is larger near the

bottom of the cascade and the peak turning angles decrease as you move up the cascade; this

corresponds with the lower static pressure. For the 360,000 and 720,000 Reynolds number

cases, the peak turning angle is nearly the same across the cascade, which also matches the static

pressure profiles.
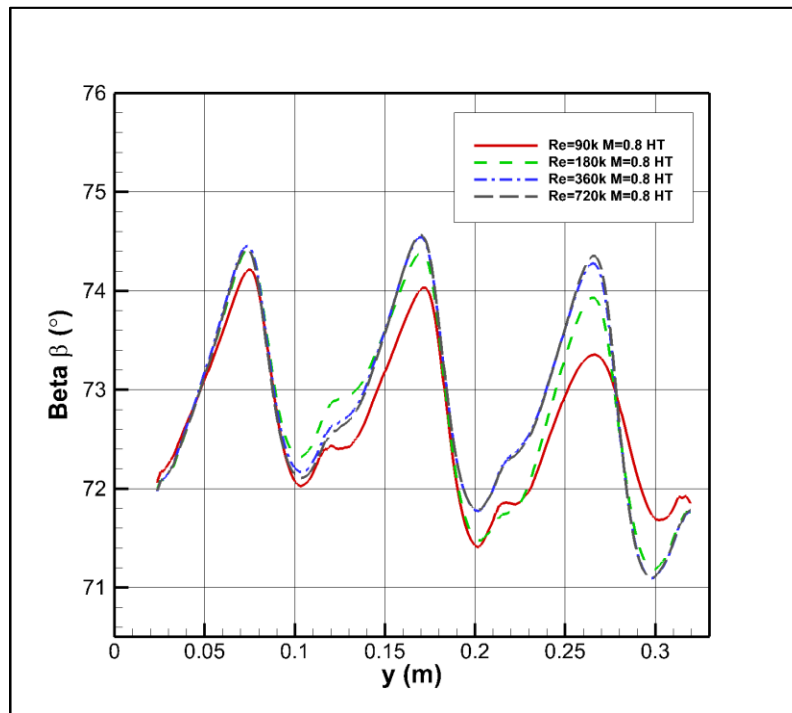
Figure 6.8. Downstream turning angles for various Reynolds numbers at Ma = 0.8 and high
turbulence

In order to correct downstream static pressure discrepancy, the outlet geometry was

changed from perpendicular to the flow to parallel to the vane cascade. This change did have a

noticeable effect on the lower Reynolds number cases. A comparison between the previous

results of (Flage, 2015), which used the perpendicular outlet, and the current work, which uses a

parallel outlet is shown in Figure 6.9. One other possible modification is to adjust the bleed pressures. This was attempted during testing, but no changes to the downstream pressure profile were visible regardless of the relative pressure at the bleed outlets. Currently, there are no other available methods to correct the static pressure profile discrepancy.
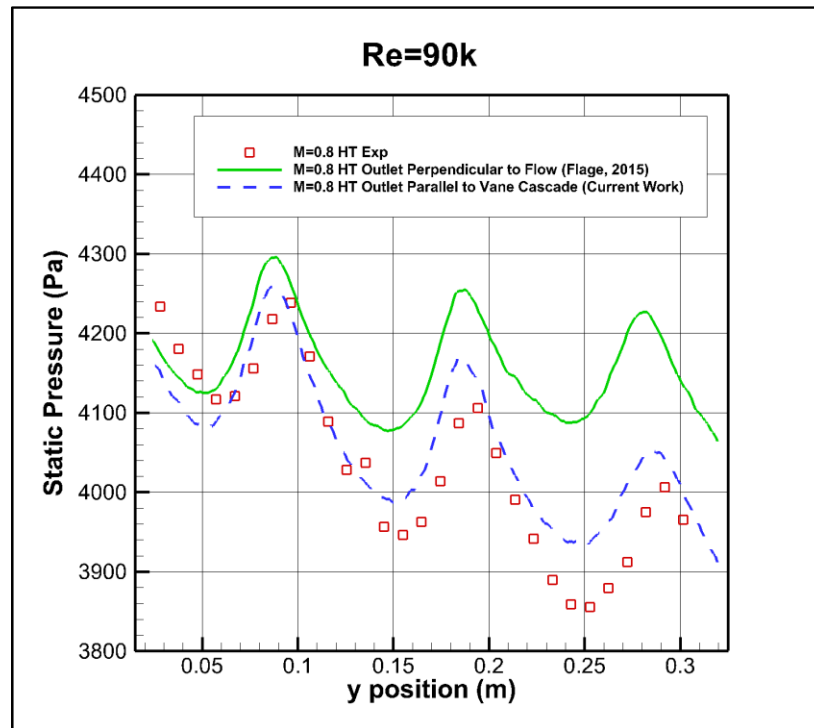
Figure 6.9. Downstream static pressure profile comparison for different outlet geometries for Re = 90,000 and Ma = 0.8 at high turbulence

Figures 6.10 and 6.11 show the Mach number distribution of the flow at a quarter axial chord downstream of the vane cascade. The Mach number presented here is not a measured value; rather, it is calculated from the static pressure using an incompressible flow relationship. The experimental Mach numbers start low near the bottom of the cascade and then slowly increase as you move up the cascade. This is well captured by the computational results at a Reynolds number of 90,000 and partially captured at a Reynolds number of 180,000. At the higher numbers, the Mach number is horizontal and does not show the same trend. This is

58

consistent with the static pressure profiles. Correcting the static pressure profiles will also

correct the Mach number distribution.

Figure 6.10. Downstream Mach distributions for Re = 90,000 (left) and Re = 180,000 (right)
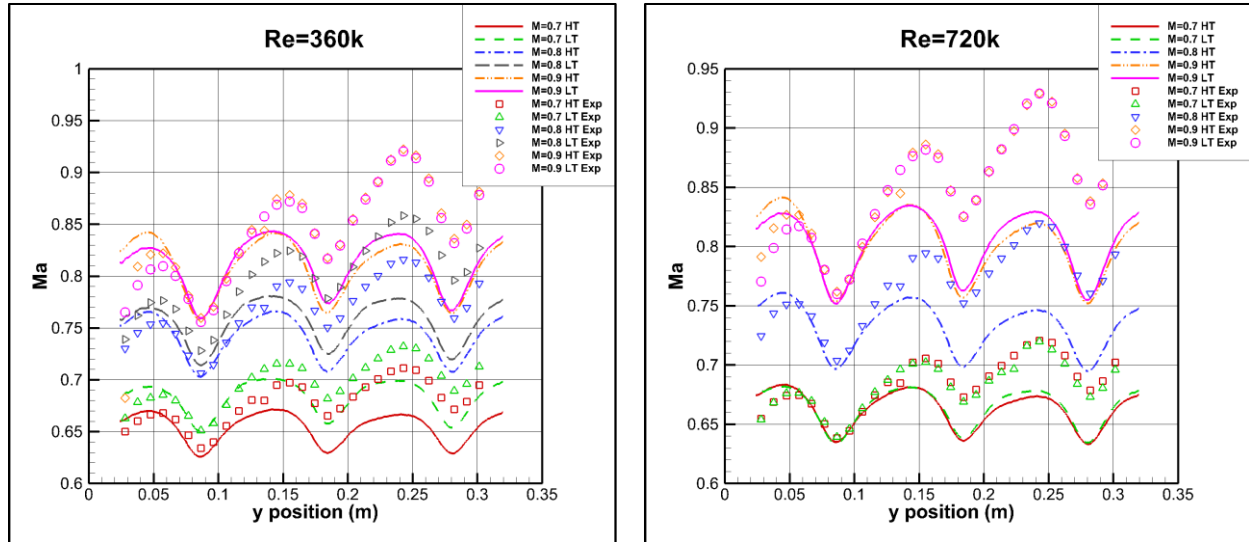
Figure 6.11. Downstream Mach distributions for Re = 360,000 (left) and Re = 720,000 (right)

Pressure Distributions on the instrumented vane surface are shown in Figures 6.12

through 6.15. These figures have been split into separate plots for the low turbulence and high

turbulence cases. After matching the upstream and downstream static pressure distributions

from the experiment, the surface pressure distributions from the CFD simulations show excellent

agreement with the experimental surface pressure distributions. The only exception is near the tail end of the suction surface. For both 720,000 Reynolds number cases and the high turbulence level 360,000 Reynolds number case, Figure 6.14 (left) and 6.15, there is a sudden increase in pressure that was not present in the experiments. The pressure increase is most likely due to the same cause of the over prediction of the static pressure distribution at a quarter axial chord downstream from the vanes. The pressure is over predicted near the top of the cascade, so the pressure on the vane surface needs to increase near tail end of the vane in order to match the downstream pressure.
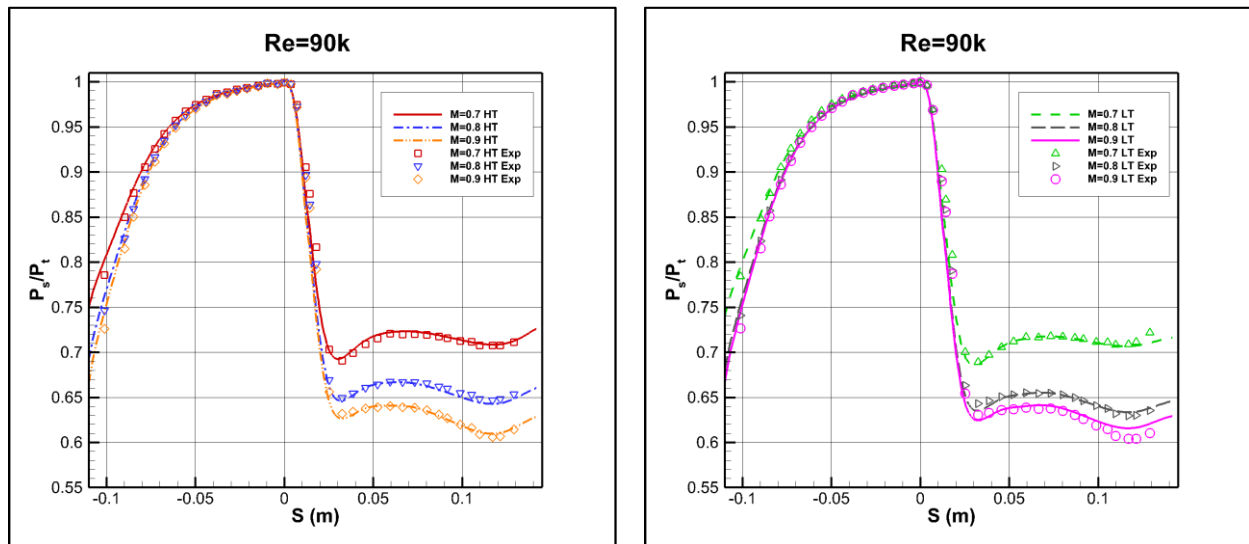
Figure 6.12. Vane pressure distributions for Re = 90,000 at high turbulence (left) and low turbulence (right)
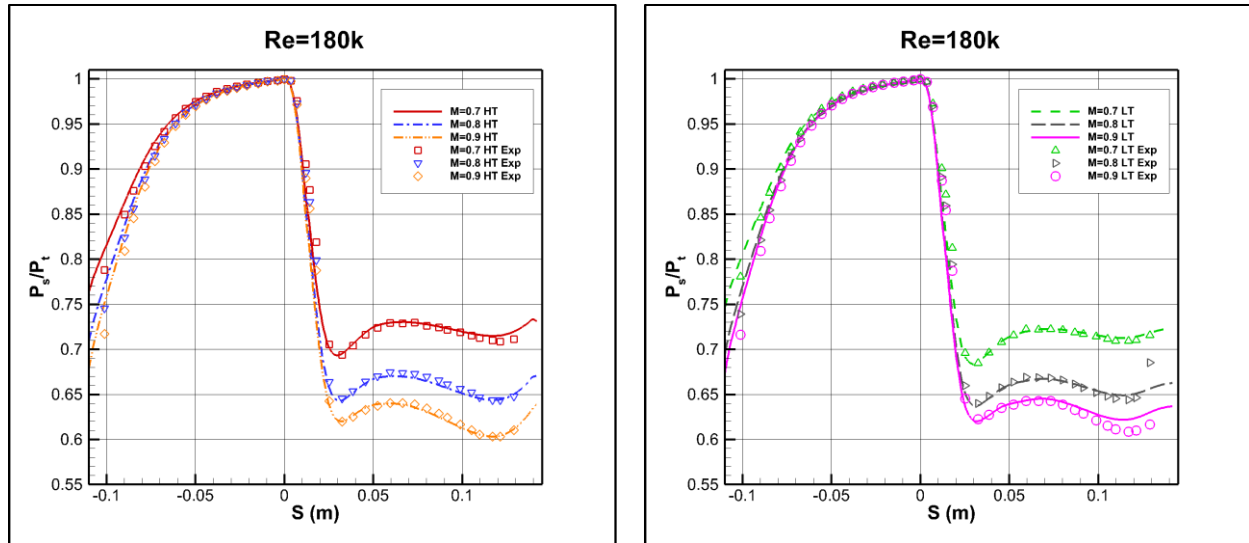
Figure 6.13. Vane pressure distributions for Re = 180,000 at high turbulence (left) and low turbulence (right)
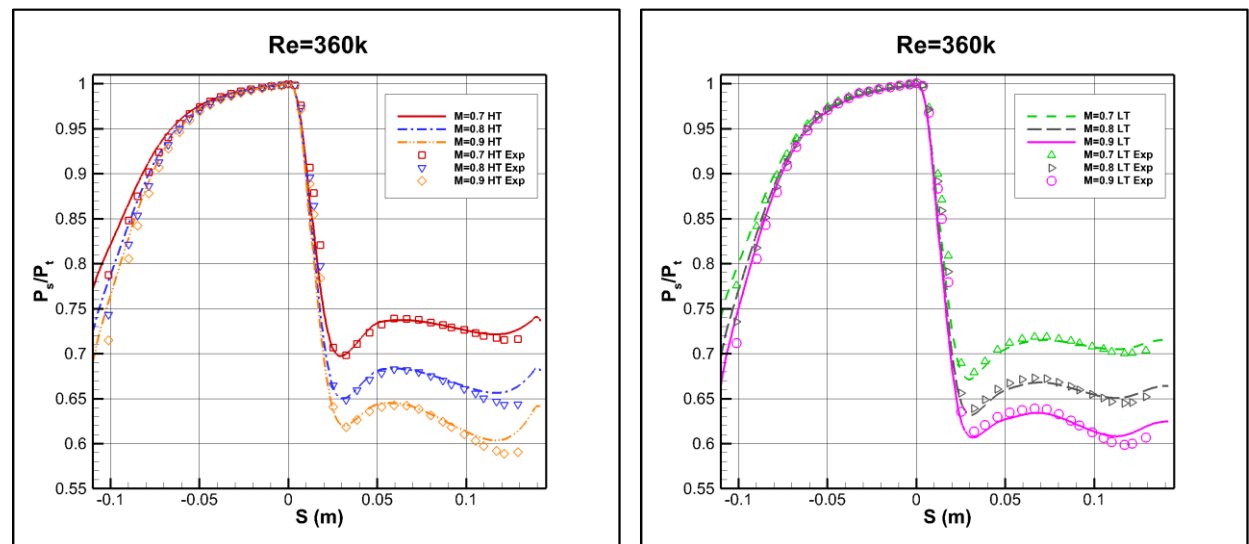
Figure 6.14. Vane pressure distributions for Re = 360,000 at high turbulence (left) and low turbulence (right)
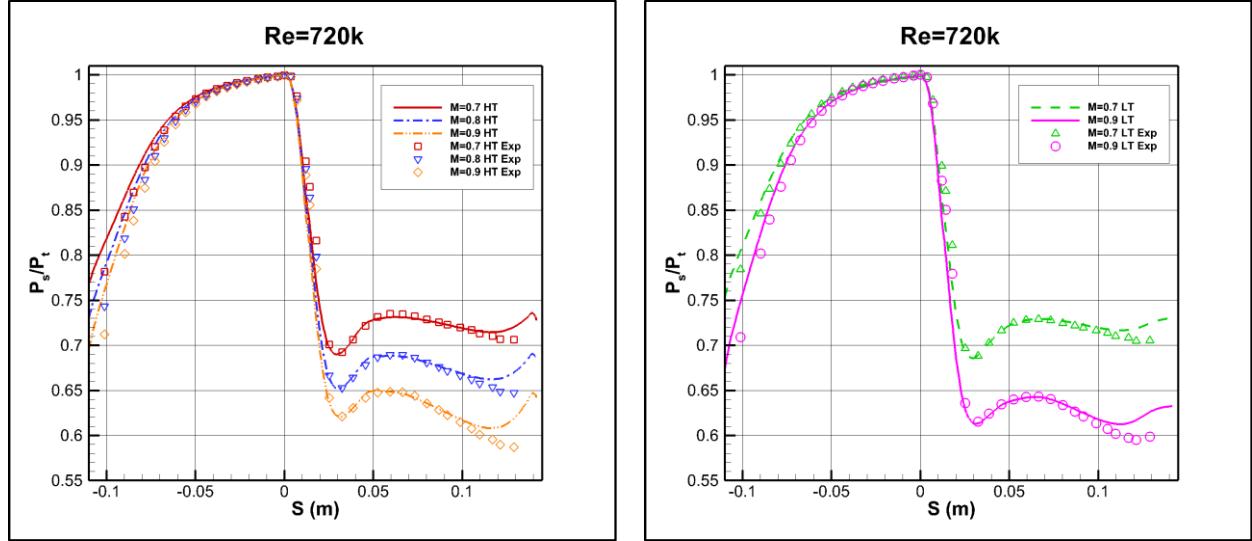
Figure 6.15. Vane pressure distributions for Re = 720,000 at high turbulence (left) and low turbulence (right)

At the outlet of the cascade, exit survey pressure measurements were taken in a plane perpendicular to the exit flow. These were used to calculate the total pressure loss coefficient, omega, downstream of the vane. Omega is defined as

$$\Omega = \frac{P_{T,in} - P_{T,ex}}{P_{T,in} - P_{s,ex}}$$
(6.1)

There was a large disagreement in the downstream total pressure loss coefficient contours between the experimental and computational results. The computational result showed a much stronger loss core near the wall as well as less swirling near the mid-passage. Figure 6.16 shows a sample comparison for the high turbulence, 180,000 Reynolds number, and 0.8 Mach number case.
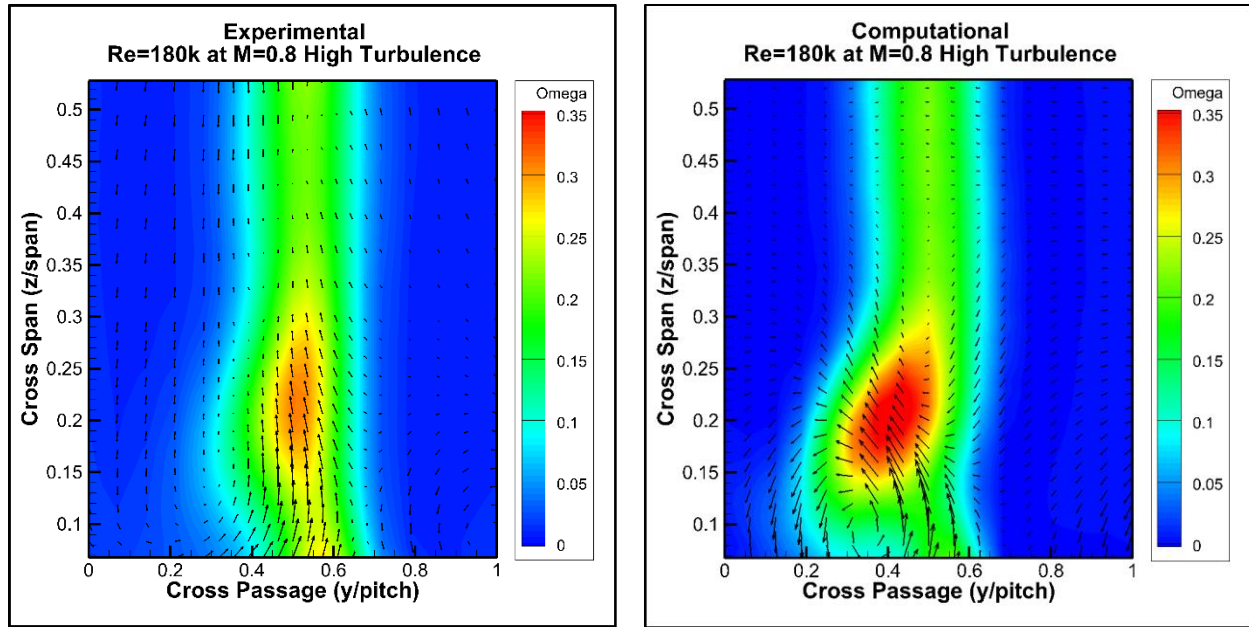
Figure 6.16. Exit survey total pressure loss coefficient for Re = 180,000, Ma = 0.8, and high turbulence, experimental (left) and computational (right)

The exit survey pressure profiles can also be condensed in into an average loss coefficient, omega bar, consisting of a mass weighted average of omega across the passage. All cases are compared in Figures 6.17 through 6.20. In most cases, Mach number causes small differences in the experimental results, but this is not captured in the computational results. Reynolds number and turbulence level have a larger effect on omega bar. There are a few possibilities for the discrepancy between the experimental and computational pressure loss coefficients. There could be unsteady vortex shedding off of the tail end of vane. This would disturb the downstream flow and it would not be captured by the steady state RANS simulation. There was also some unsteadiness reported from the experiment, although it was not captured in a way that could be reproduced in the simulations. This could also cause changes in the downstream flow that would not be captured by the steady state simulations.
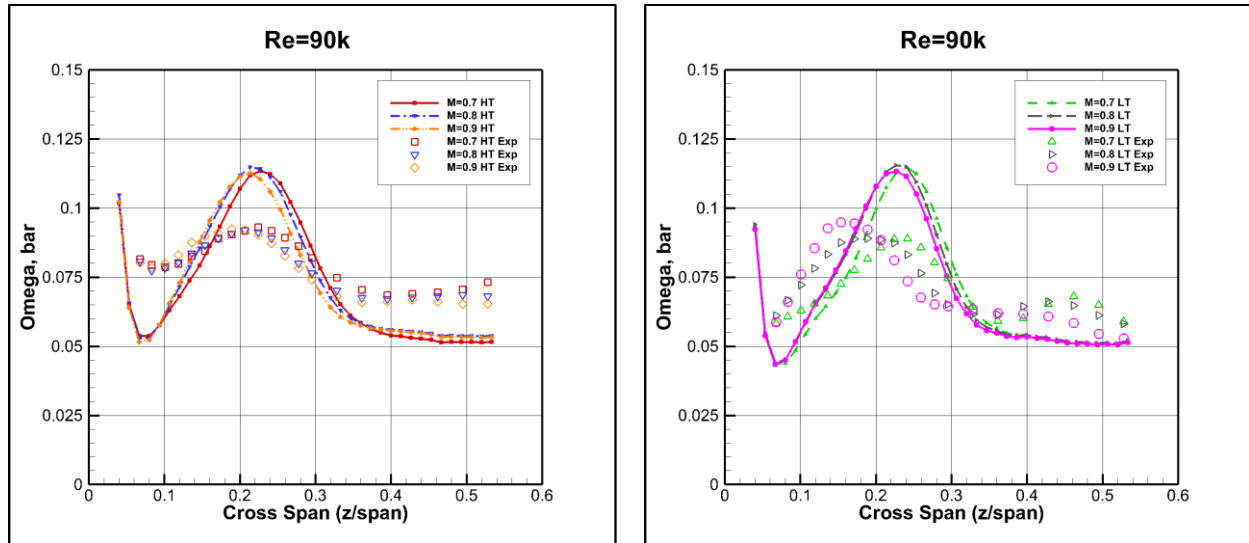
Figure 6.17. Cross-passage mass averaged total pressure loss coefficient versus span for Re = 90,000 at high turbulence (left) and low turbulence (right)
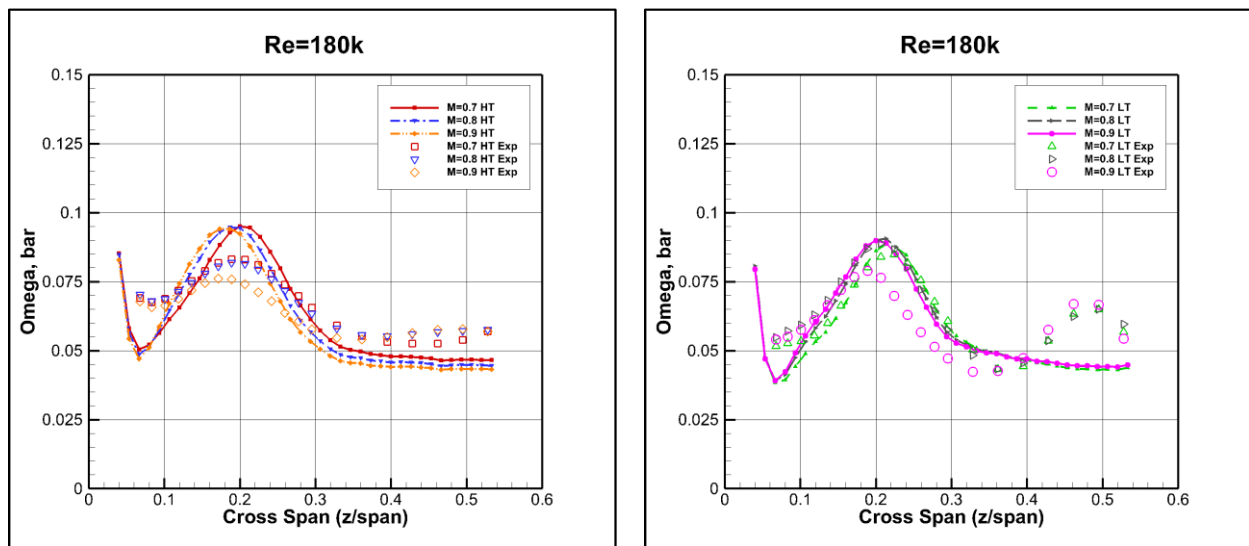

Figure 6.18. Cross-passage mass averaged total pressure loss coefficient versus span for Re = 180,000 at high turbulence (left) and low turbulence (right)
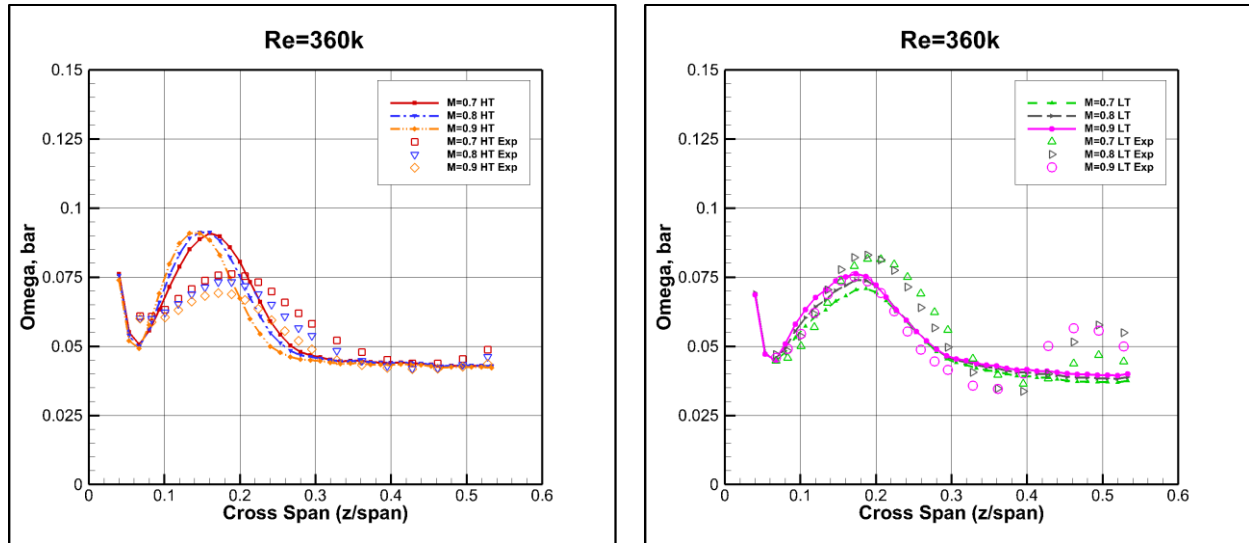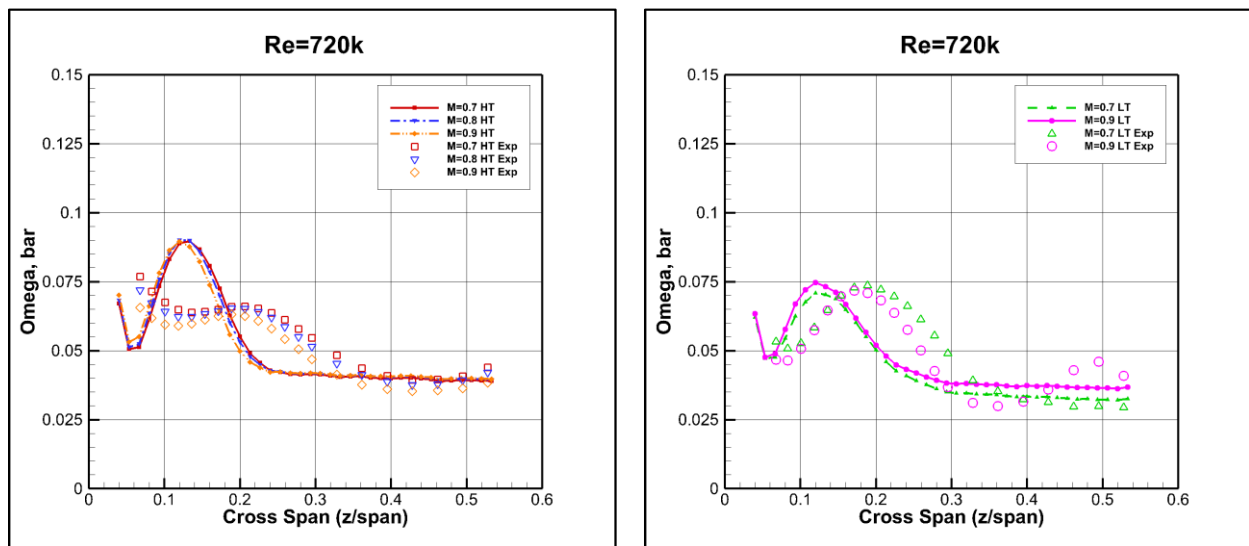
Figure 6.19. Cross-passage mass averaged total pressure loss coefficient versus span for Re = 360,000 at high turbulence (left) and low turbulence (right)

Figure 6.20. Cross-passage mass averaged total pressure loss coefficient versus span for Re = 720,000 at high turbulence (left) and low turbulence (right)

If the cross-passage mass averaged total pressure loss coefficient is replotted in terms of similar Mach number, shown in Figures 6.21 through 6.23, a few other trends become more apparent. As the Reynolds number increases, the peak loss coefficient decreases until you reach a Reynolds number of 360,000. For the high turbulence cases, the peak loss coefficient is over

predicted for all Reynolds numbers. With the low turbulence cases, the peak loss coefficient is

under predicted for the 360,000 and 720,000 Reynolds numbers, except at a Mach number of 0.9.
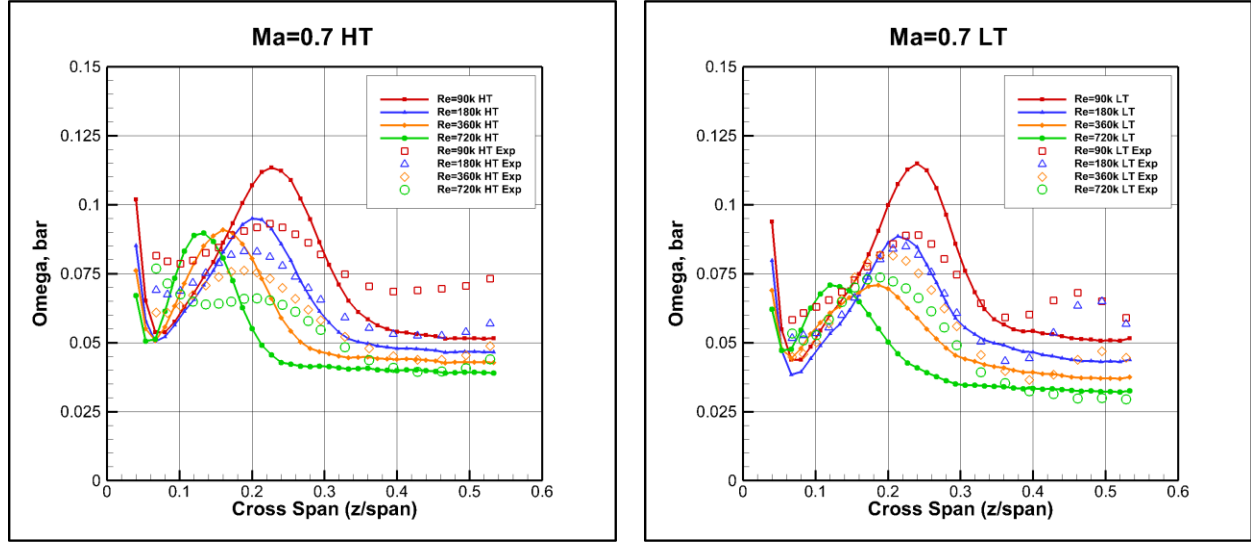

Figure 6.21. Cross-passage mass averaged total pressure loss coefficient versus span for Ma = 0.7 at high turbulence (left) and low turbulence (right)
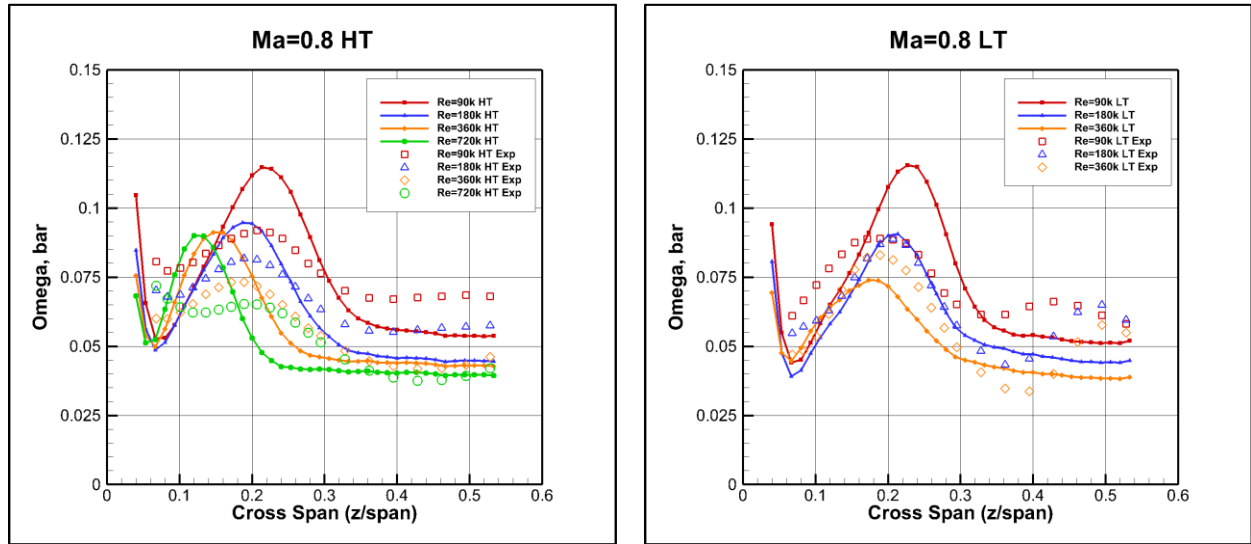

Figure 6.22. Cross-passage mass averaged total pressure loss coefficient versus span for Ma = 0.8 at high turbulence (left) and low turbulence (right)
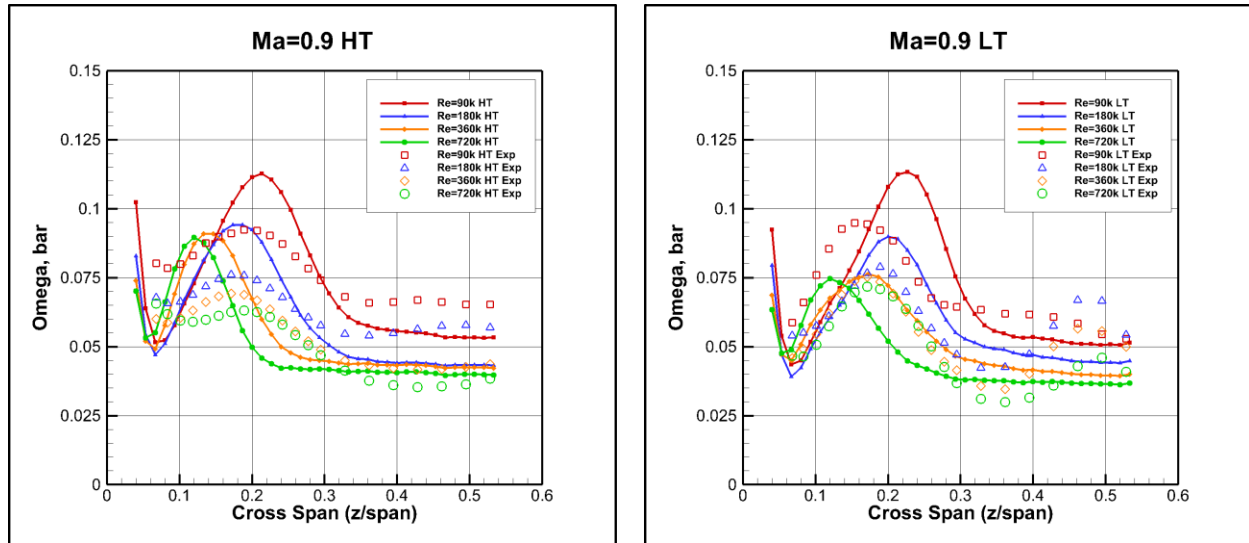
Figure 6.23. Cross-passage mass averaged total pressure loss coefficient versus span for Ma = 0.9 at high turbulence (left) and low turbulence (right)

During the exit survey, information was also recorded in order to calculate the turning angle of the flow. Mach number has a larger effect on the experimental results, but almost no effect on the computational results. The cross-passage mass averaged turning angles are shown in Figure 6.24 through 6.27. The largest error in the turning angle is near the wall, which is same area where the total pressure loss coefficient showed the largest error. It is believed this is related to the same cause of error in the total pressure loss coefficient.
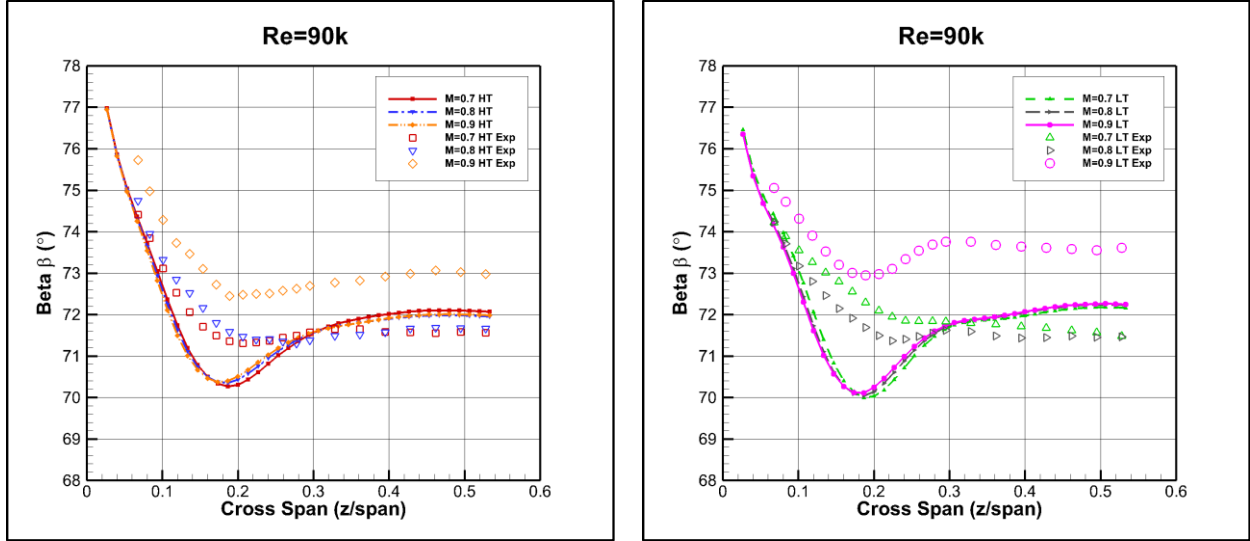
67

Figure 6.24. Cross-passage mass averaged turning angle versus span for Re = 90,000 at high turbulence (left) and low turbulence (right)
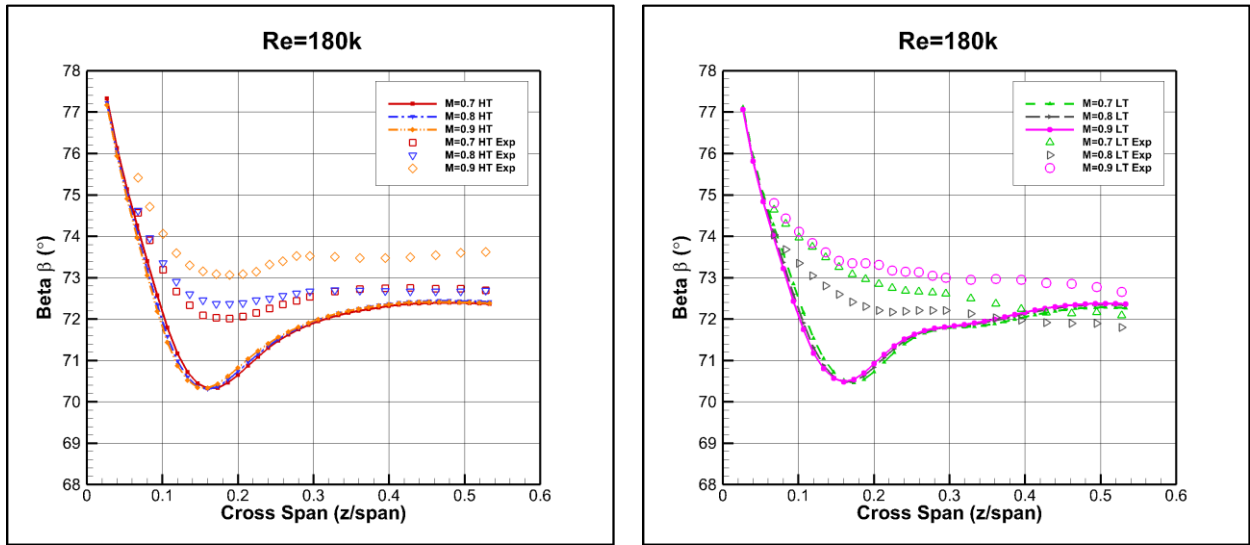

Figure 6.25. Cross-passage mass averaged turning angle versus span for Re = 180,000 at high turbulence (left) and low turbulence (right)
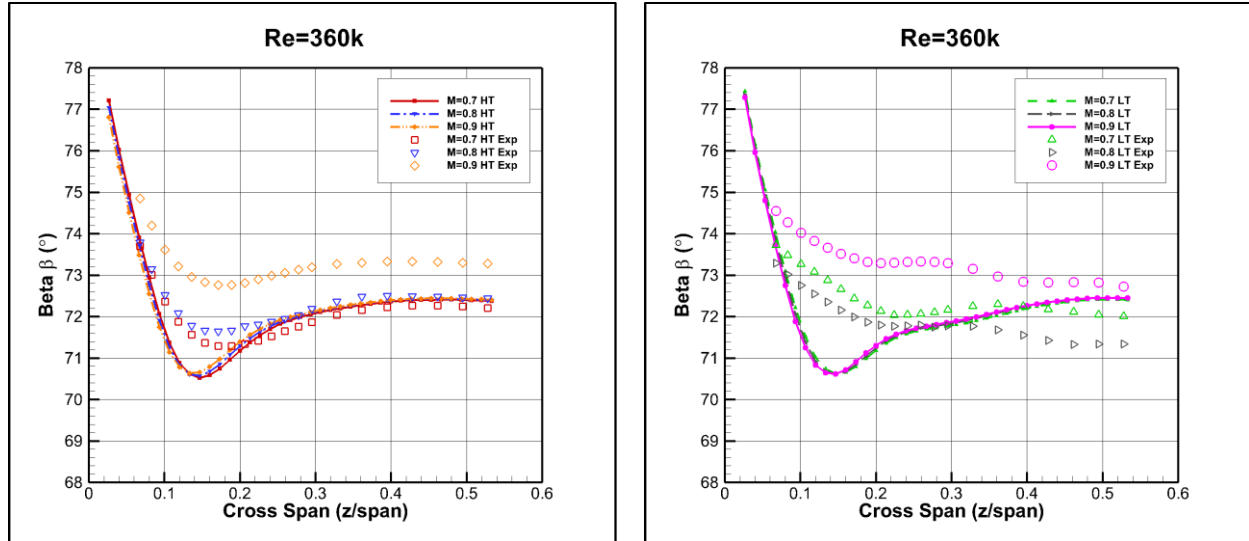
Figure 6.26. Cross-passage mass averaged turning angle versus span for Re = 360,000 at high turbulence (left) and low turbulence (right)
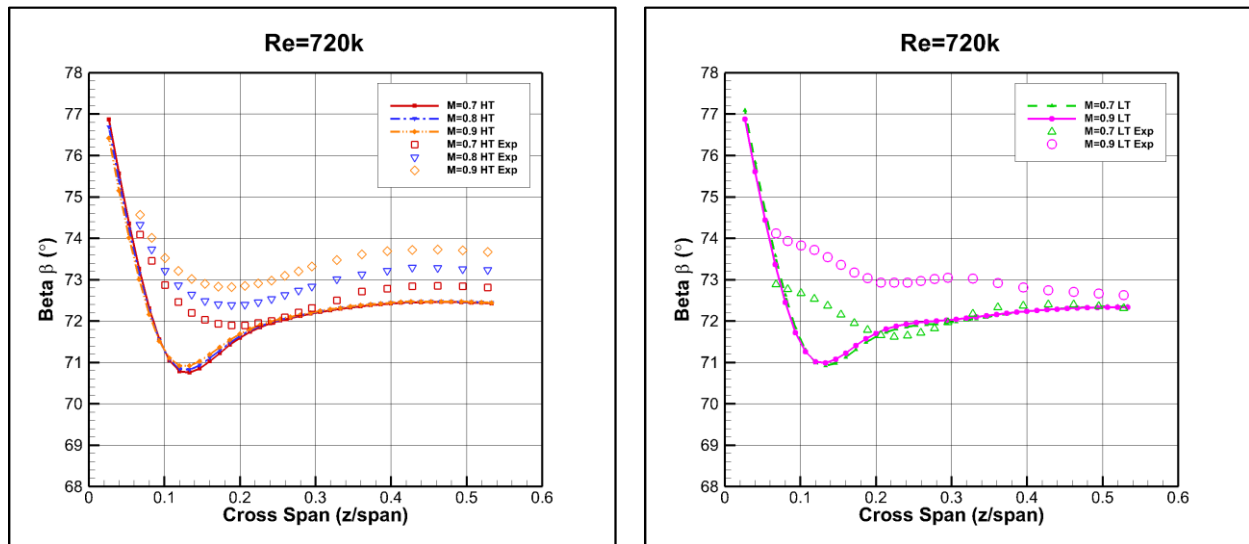

Figure 6.27. Cross-passage mass averaged turning angle versus span for Re = 720,000 at high turbulence (left) and low turbulence (right)

6.2. Heat Transfer Study Results

The heat transfer study used the same set of cases as the aerodynamic loading study with the addition of a fifth Reynolds number of 1,000,000. Information was unavailable for the Mach 0.9 cases at a Reynolds number of 90,000, so those two cases were not run. Less experimental data was also taken for the heat transfer case. Instead of full pressure distributions at a quarter

chord upstream and downstream, only a single upstream and downstream pressure were reported. Due to this lack of information, the downstream pressure matching is less exact than was possible for the aerodynamic loading cases.

The heat transfer coefficient can be calculated with the following equation

$$h = \frac{q''}{A_{vane} * (T_{heated} - T_{adiabatic})}$$

(6.2)

The heat flux (q'') is from the experiment and is based on the power required to heat the Inconel foil. Both a heated wall (T_{heated}) and adiabatic wall ($T_{adiabatic}$) temperature are needed in order to calculate the heat transfer coefficient. The second wall temperature required each simulation to be run twice instead of once like the aerodynamic loading study. The heat transfer coefficient on the instrumented vane surface is shown in Figures 6.28 through 6.32.
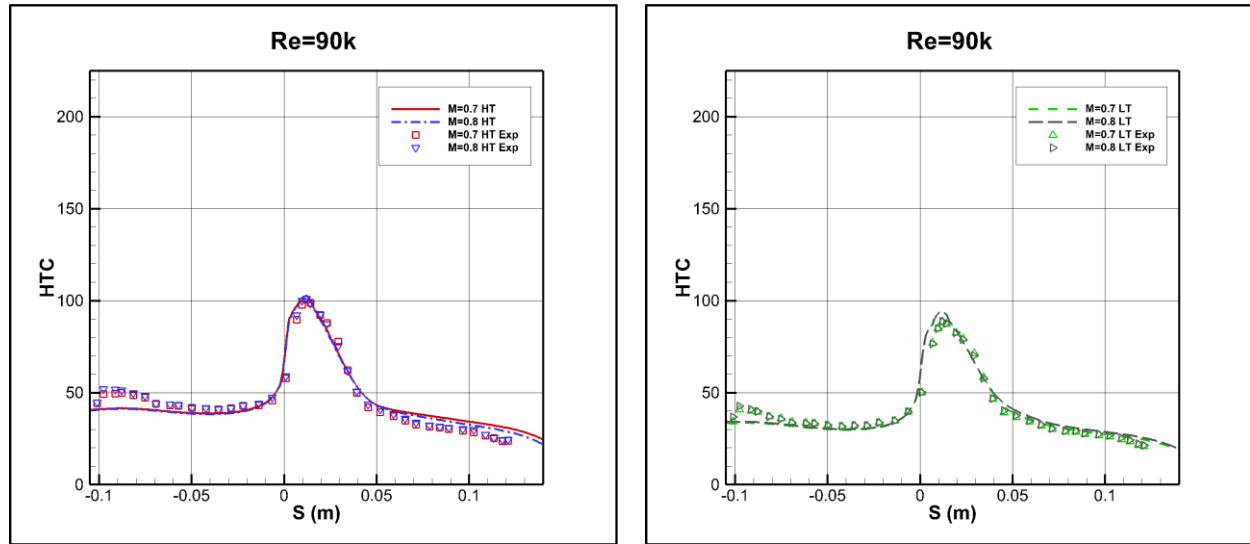

Figure 6.28. Heat transfer coefficient for Re = 90,000 at high turbulence (left) and low turbulence (right)
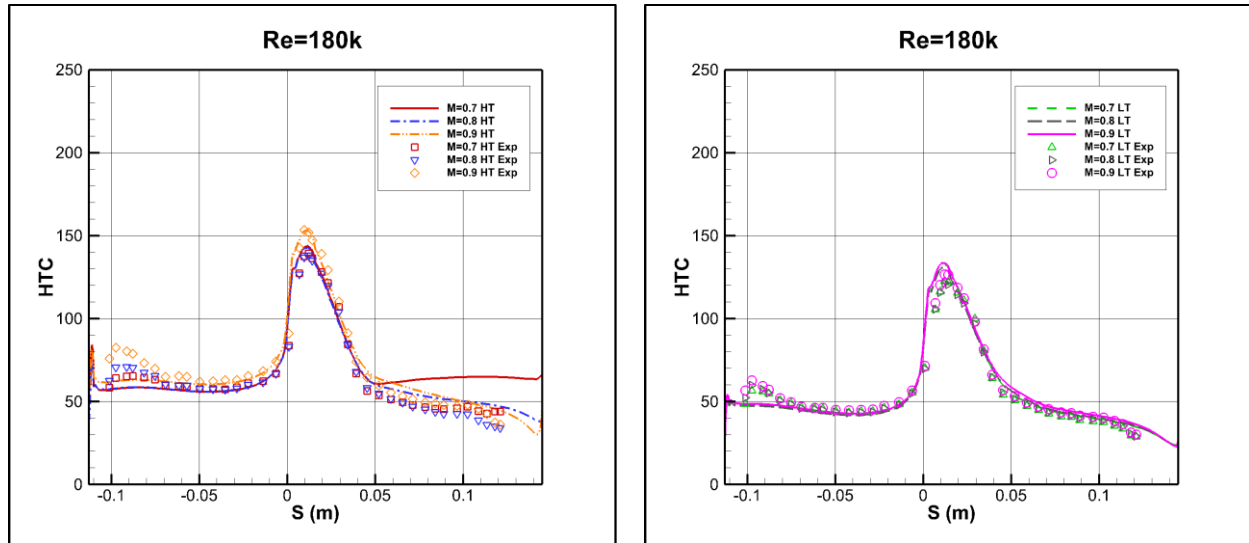
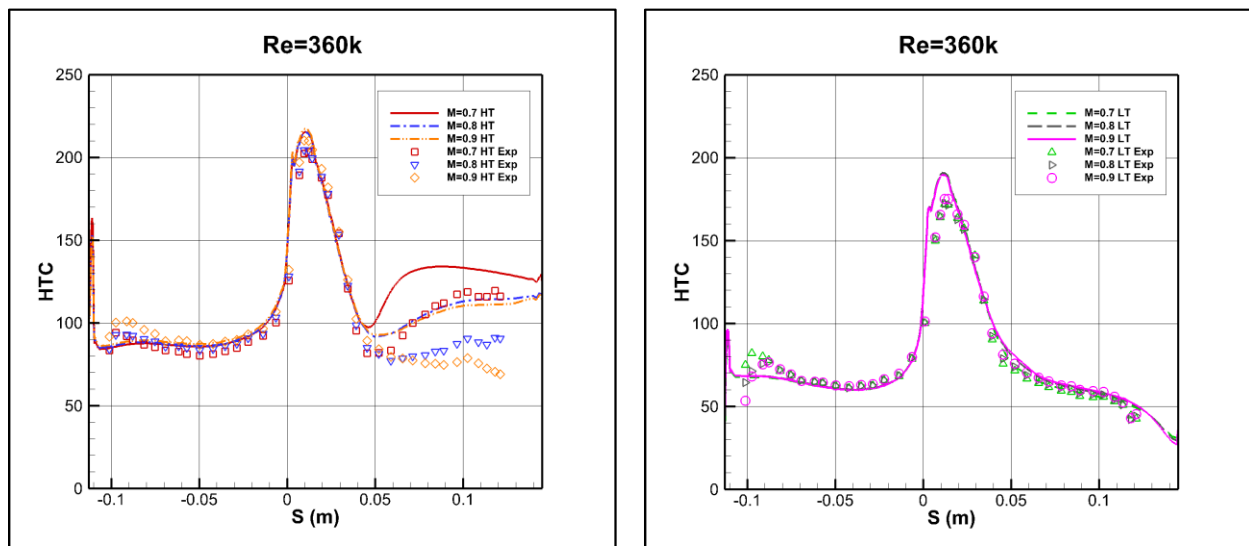Figure 6.29. Heat transfer coefficient for Re = 180,000 at high turbulence (left) and low turbulence (right)

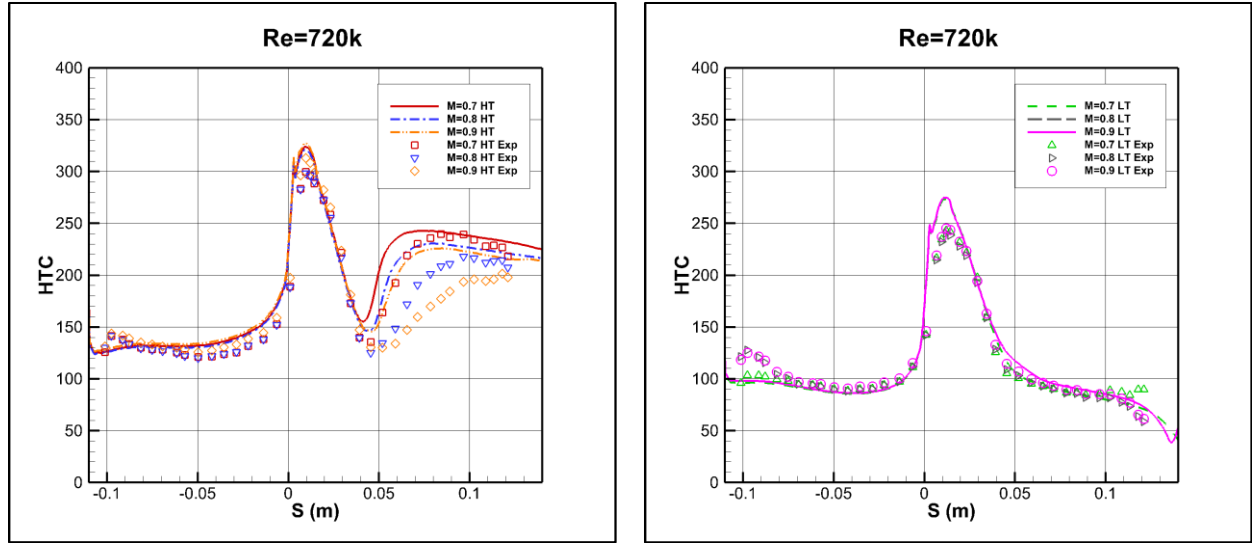Figure 6.30. Heat transfer coefficient for Re = 360,000 at high turbulence (left) and low turbulence (right)

Figure 6.31. Heat transfer coefficient for Re = 720,000 at high turbulence (left) and low turbulence (right)
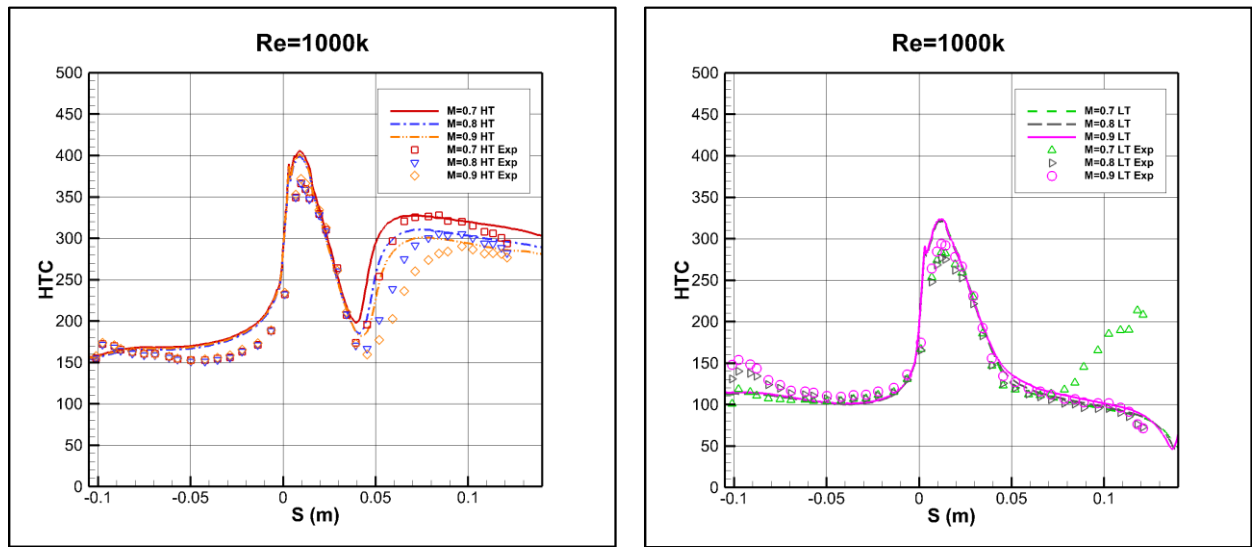
Figure 6.32. Heat transfer coefficient for Re = 1,000,000 at high turbulence (left) and low turbulence (right)

The best agreement is shown for the low turbulence level cases. Both the experiment and the simulation show laminar flow over the entire surface of the vane. For the high turbulence level cases, the flow starts to transition on the suction surface and the experiment and simulation disagree. At a Reynolds number of 90,000, both the simulation and the experiment agree that all cases remain laminar. At a Reynolds number of 180,000, the experiment still shows laminar

flow for all cases, but the simulation for a Mach number of 0.7 starts to show transition. Above a Reynolds number of 180,000, both the experiment and the simulation predict transition on the suction surface; however, the simulation predicts an early transition and in many cases over predicts the heat transfer on the vane suction surface.

If both the high turbulence cases and the low turbulence cases for the same Reynolds number are plotted together, the effect of turbulence on the boundary layer becomes more apparent. This is shown in Figures 6.33 through 6.37. At low Reynolds numbers, both the high turbulence and low turbulence cases remain completely laminar. As the Reynolds number increases, the simulations start to show transition at a Reynolds number of 180,000, Figure 6.34, and the experiments show transition beginning at a Reynolds number of 360,000, Figure 6.35. The high free stream turbulence level is disturbing the boundary layer flow at higher Reynolds numbers and forcing bypass transition on the vane suction surface.

Figure 6.33. Heat transfer coefficient for Re = 90,000, high and low turbulence combined

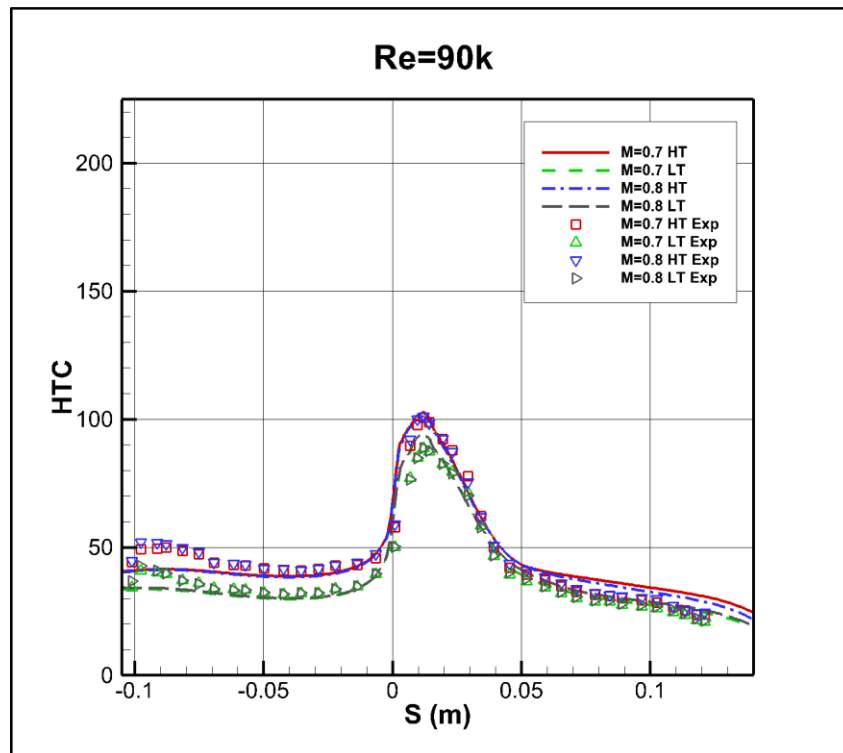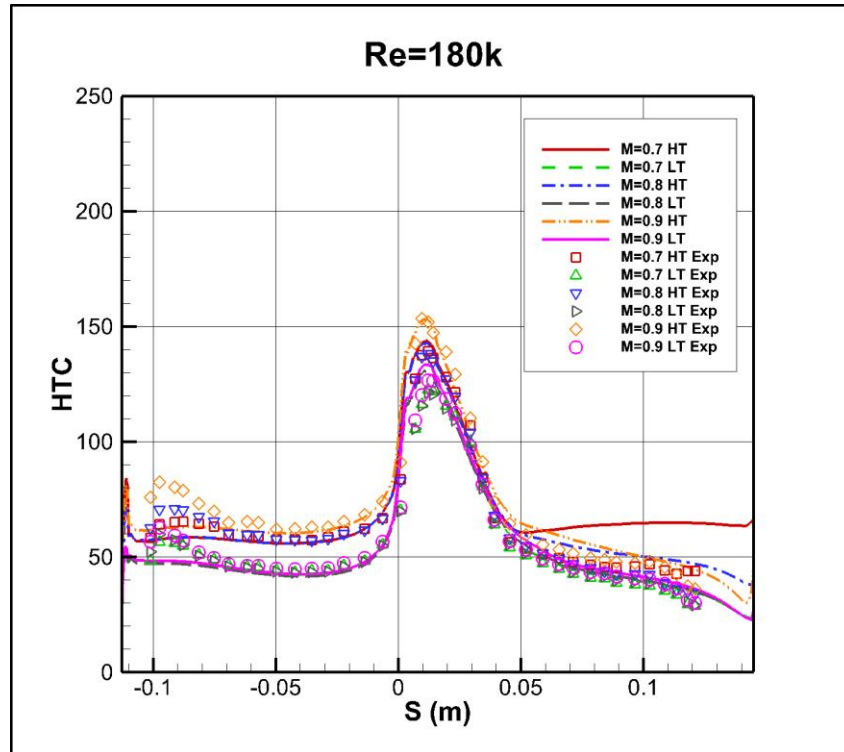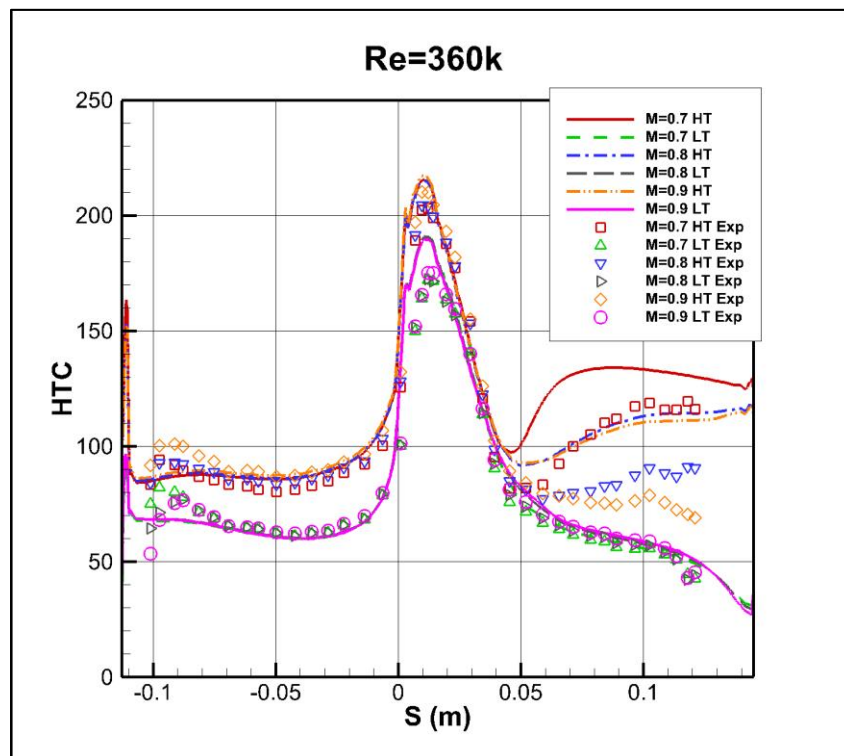Figure 6.34. Heat transfer coefficient for Re = 180,000, high and low turbulence combined

Figure 6.35. Heat transfer coefficient for Re = 360,000, high and low turbulence combined
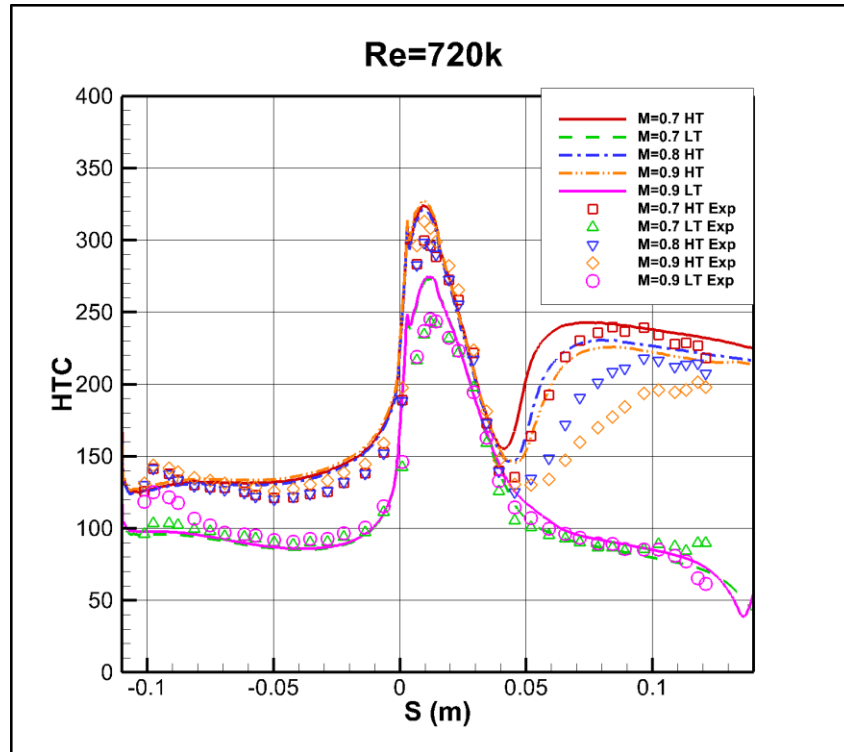
Figure 6.36. Heat transfer coefficient for Re = 720,000, high and low turbulence combined
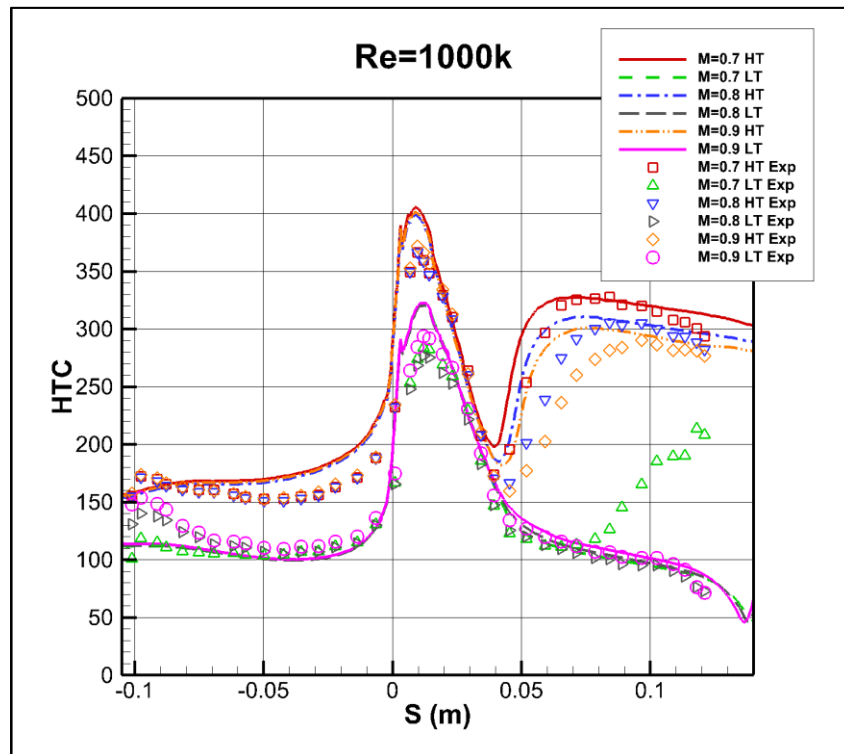
Figure 6.37. Heat transfer coefficient for Re = 1,000,000, high and low turbulence combined

The heat transfer coefficient can also be plotted by keeping the Mach number constant and varying the Reynolds number. This is shown in Figure 6.38 through 6.40. These plots show that as the Reynolds number increases, the heat transfer coefficient also increases. This effect is more significant for the high turbulence cases, with the transition region on the suction surface showing the largest increase. There is also a noticeable increase in the heat transfer coefficient for the low turbulence cases as well although not as significant as for the high turbulence cases.
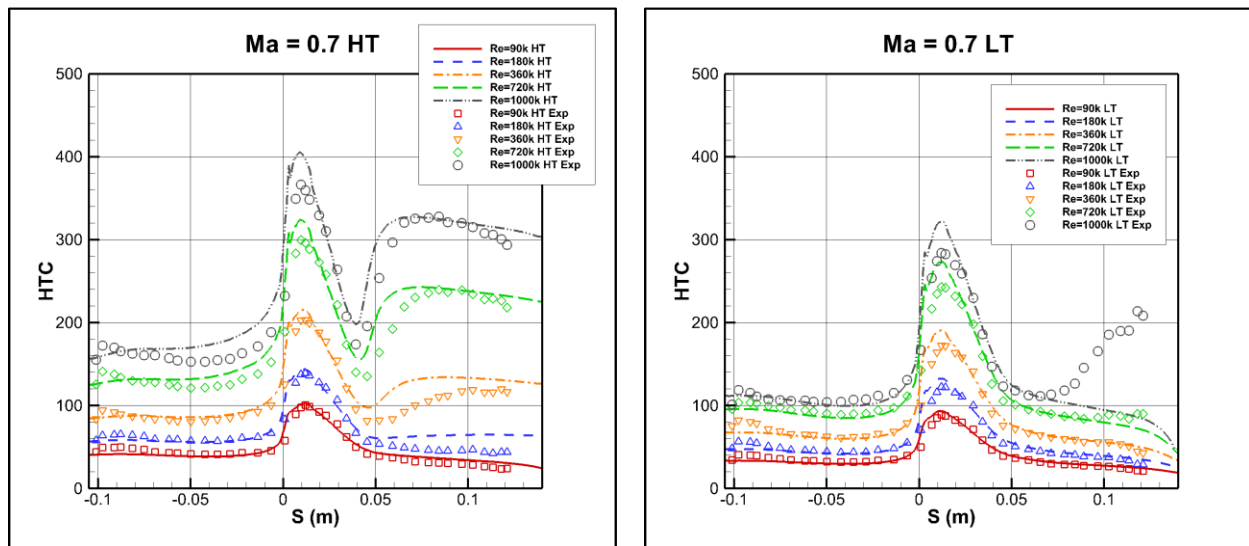
Figure 6.38. Heat transfer coefficient for Ma = 0.7 at high turbulence (left) and low turbulence (right)
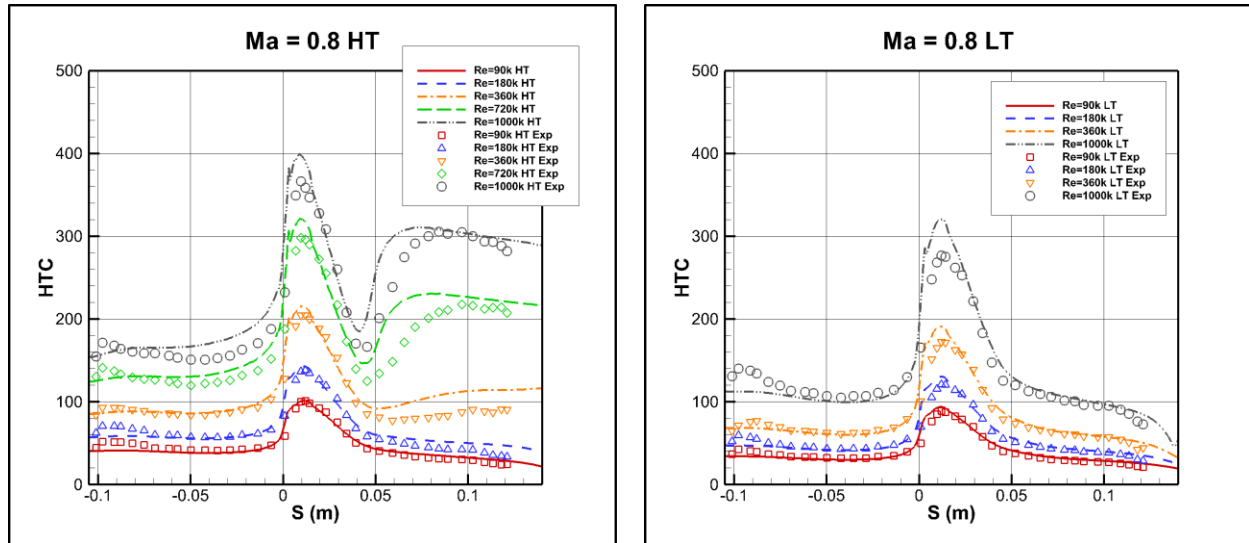
Figure 6.39. Heat transfer coefficient for Ma = 0.8 at high turbulence (left) and low turbulence (right)
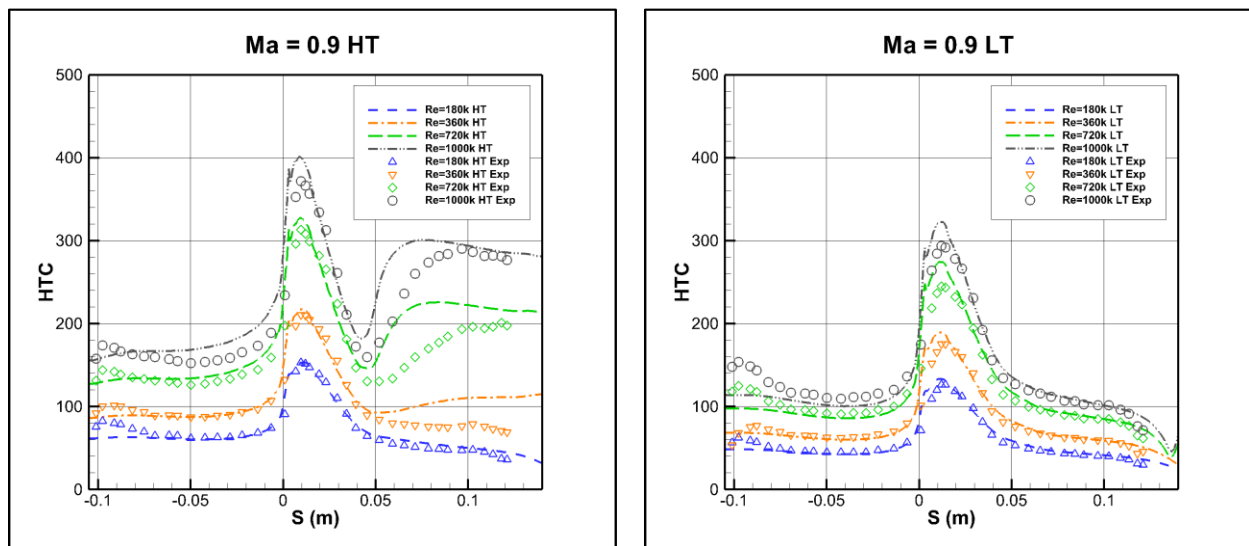
Figure 6.40. Heat transfer coefficient for Ma = 0.9 at high turbulence (left) and low turbulence (right)

A comparison between the 9% turbulence intensity and the lower adjusted 5.95% turbulence intensity is shown in Figure 6.41 for the 720,000 Reynolds number and 0.8 Mach number case. Figure 6.41 also includes a test of the curvature correction for the SST turbulence model discussed at the end of Section 3.1.4. ANSYS CFX includes a constant (*C*) that can be used adjust the sensitivity of the curvature correction. A value of one for *C* is the default and

77

applies the curvature correction as it was originally specified. Raising or lowering the *C* value

will increase or decrease the multiplier on the production term in the SST turbulence model.
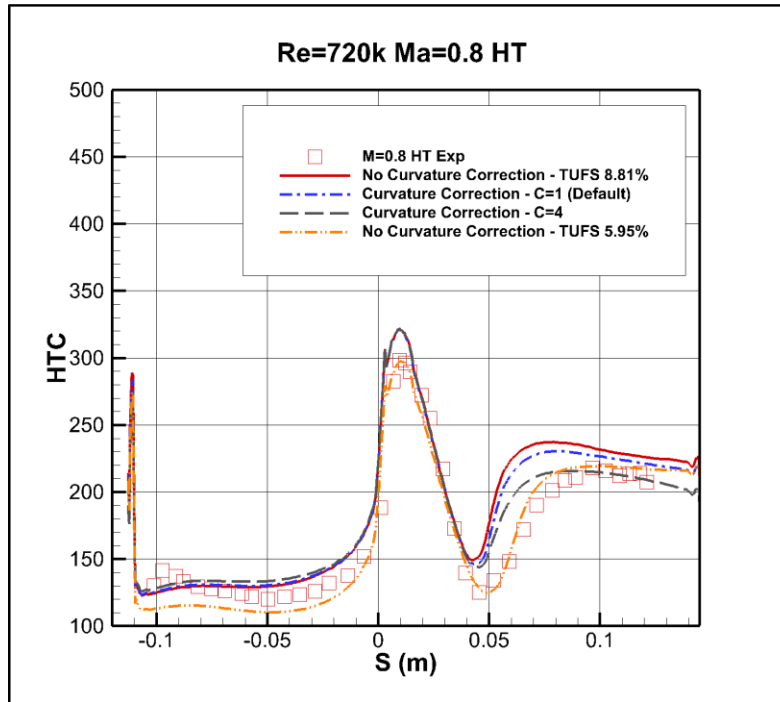
Figure 6.41. Heat transfer coefficient comparison for Re = 720,000 and Ma = 0.8

As can be seen in Figure 6.30, the curvature correction for the SST turbulence model

provides a small improvement to the heat transfer prediction in the fully turbulent region.

Including the curvature correction did not have a large effect on the transition point. Increasing

the adjustment constant further improved the heat transfer prediction in the fully turbulent

region; however, it did not change the transition location. Making this adjustment is not

recommended because the value of *C* is somewhat arbitrary, and values larger than one may lead

to a physically unrealistic value for the turbulence model production term.

It is believed that the discrepancy in the heat transfer prediction is due to two possible

causes. For the experiment, the turbulence intensity was only measured for a couple of cases and

then assumed to be the same for all of the cases run with the same inlet nozzle configuration.

This worked well for the low turbulence intensity cases because the turbulence level was low enough that it did not affect the boundary layer. At the higher turbulence levels, the turbulence intensity is large enough that it can force transition to occur. The SST turbulence model and the γ-Re_θ transition model are sensitive enough that small changes of 5% to 10% in the turbulence intensity can have a large effect on the predicted heat transfer. If the assumption of the same turbulence intensity is not correct, the predicted heat transfer will not be correct.

There may also be some problems with the turbulence and transition models themselves as well. The SST turbulence model and the γ-Re_θ transition model are currently the best models available for this type of flow. That does not mean that they are perfect or can predict every flow with 100% accuracy. This may be one of the flow cases where they fall somewhat short.

6.3. Scale Adaptive Simulation Results

In order to try to better capture any unsteady flow features downstream from the vane cascade, three different SAS simulations were run on two different test cases. An aerodynamic case was run twice for the 360,000 Reynolds number and 0.8 Mach number at high turbulence. The transient SAS simulations require a starting solution file. The first run started from the fully converged RANS steady state solution and the second run was started from an unconverged RANS steady state solution.

The goal of the SAS simulation for the aerodynamic case was to improve the total pressure loss coefficient contour downstream from the instrumented vane. It was hoped that the transient simulation would be able to capture any unsteady turbulent structures that were shedding off the end of the vane. This turned out not to be the case. The experimental loss contour plot and the converged steady state RANS simulation loss contour plot are shown in Figure 6.42. After approximately 5,900 transient simulation iterations and 0.005869 seconds of

simulation time, the loss coefficient contour developed into what is shown in Figure 6.43. The loss core became much stronger although it was distorted by a near wall vortex. The simulation was run past 5,900 iterations; however, the additional iterations had a minimal effect on the flow field. This can be seen in Figure 6.44, which shows the cross-passage mass averaged loss coefficient over time as the transient simulation progressed. The vane surface pressure distribution, which is shown in Figure 6.45, was also examined during the transient simulation and did not appear to show any variation from the surface pressure distribution from the steady state RANS simulation.
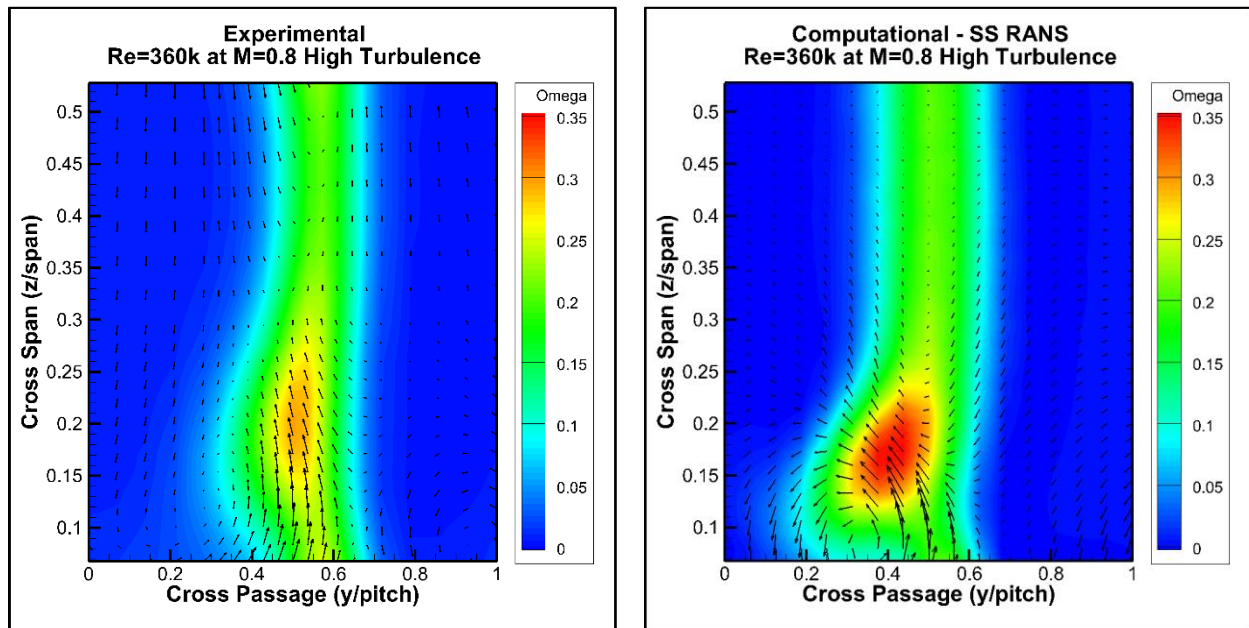
Figure 6.42. Exit survey total pressure loss coefficient for Re = 360,000, Ma = 0.8, and high turbulence, experimental (left) and computational (SS RANS) (right)

Figure 6.43. Exit survey total pressure loss coefficient for Re = 360,000, Ma = 0.8, and high turbulence, SAS simulation at 0.005869 seconds, starting from steady state
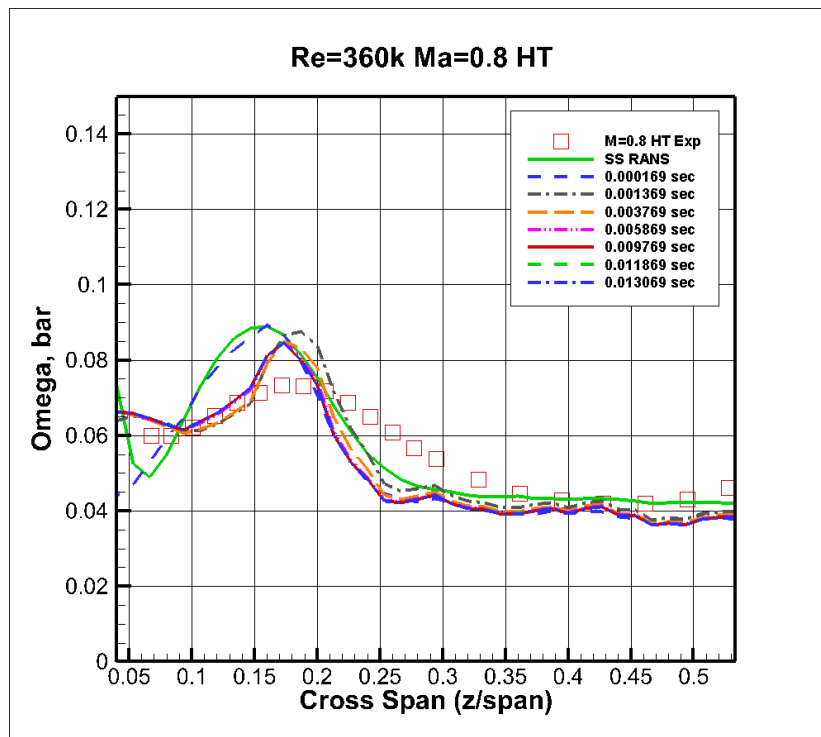
Figure 6.44. Cross-passage mass averaged total pressure loss coefficient versus span for Re = 360,000, Ma = 0.8, and high turbulence over time, starting from steady state
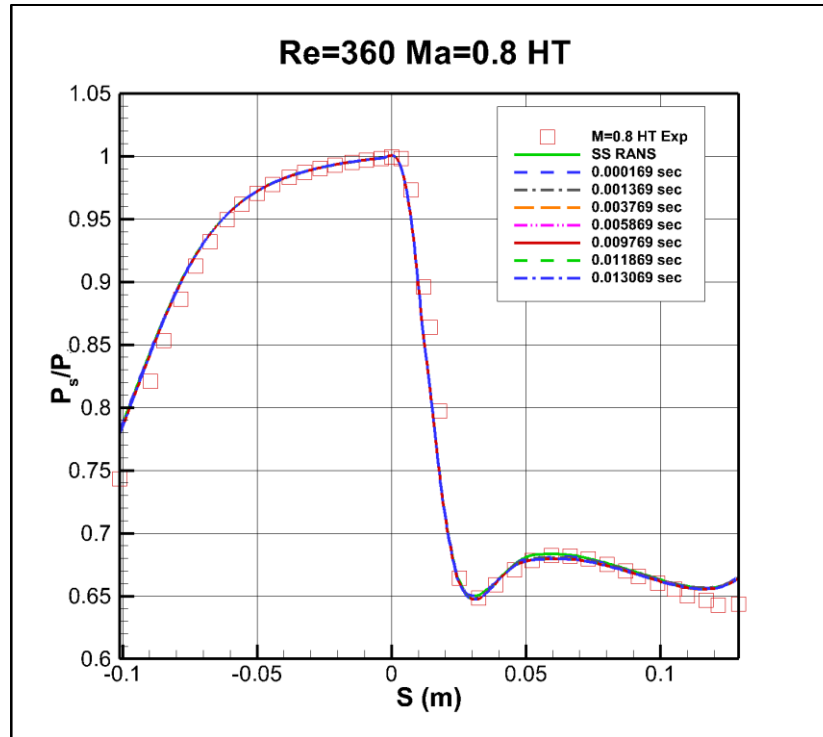
Figure 6.45. Vane pressure distribution versus surface arc for Re = 360,000, Ma = 0.8, and high turbulence over time, starting from steady state

In order to verify that starting the transient simulation from the fully converged steady state simulation was not smoothing out large turbulent features, a second transient SAS simulation was run. This time it was started from an unconverged steady state RANS simulation that was only run about 60 iterations. This transient simulation was run out to 10,000 iterations; however, the flow field appeared to stop changing around 8,000 iterations and 0.007939 seconds of transient simulation time. The loss coefficient contour plot from 8,000th iteration is shown in Figure 6.46. If Figure 6.46 is compared with Figure 6.43, it can be seen that they are virtually identical. This shows that the result is independent of the choice of starting solution for the transient SAS simulation.
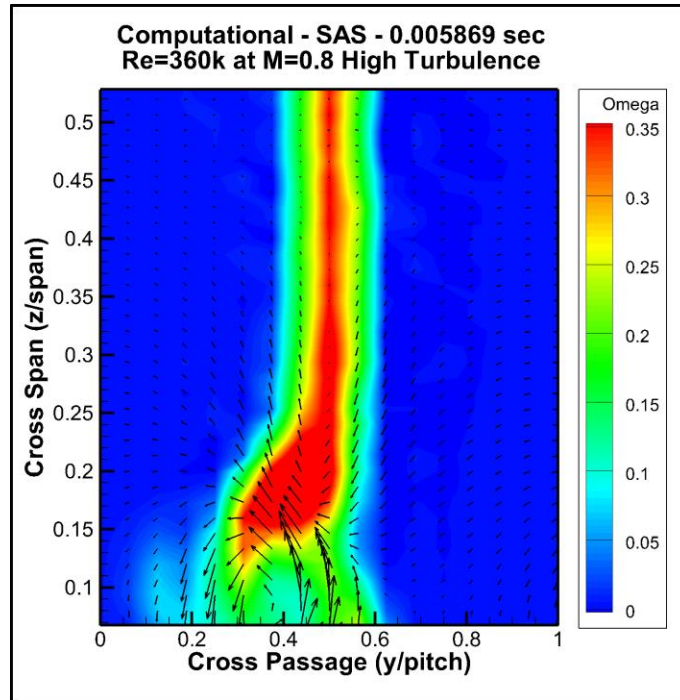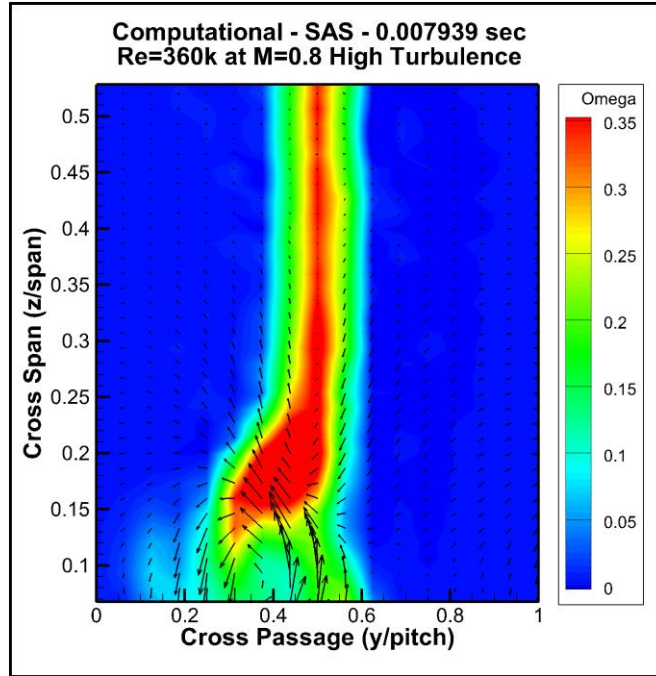
Figure 6.46. Exit survey total pressure loss coefficient for Re = 360,000, Ma = 0.8, and high turbulence, SAS simulation at 0.007939 seconds, starting from unconverged steady state simulation

A second SAS simulation was run for a heat transfer case at a Reynolds number of 720,000 and a Mach number of 0.8. Since it was previously shown that the starting solution did not have an effect on the result, the converged steady state RANS simulation was used as the starting solution. For this case, the higher inlet turbulence level with the curvature correction for the SST turbulence model was used. The heat transfer SAS simulation was run out to 4000 iterations and 0.0036 seconds. The results were compared with the steady state RANS simulation results in Figure 6.47. The heat transfer coefficient on the vane's surface remained constant and did not change over the entire run.
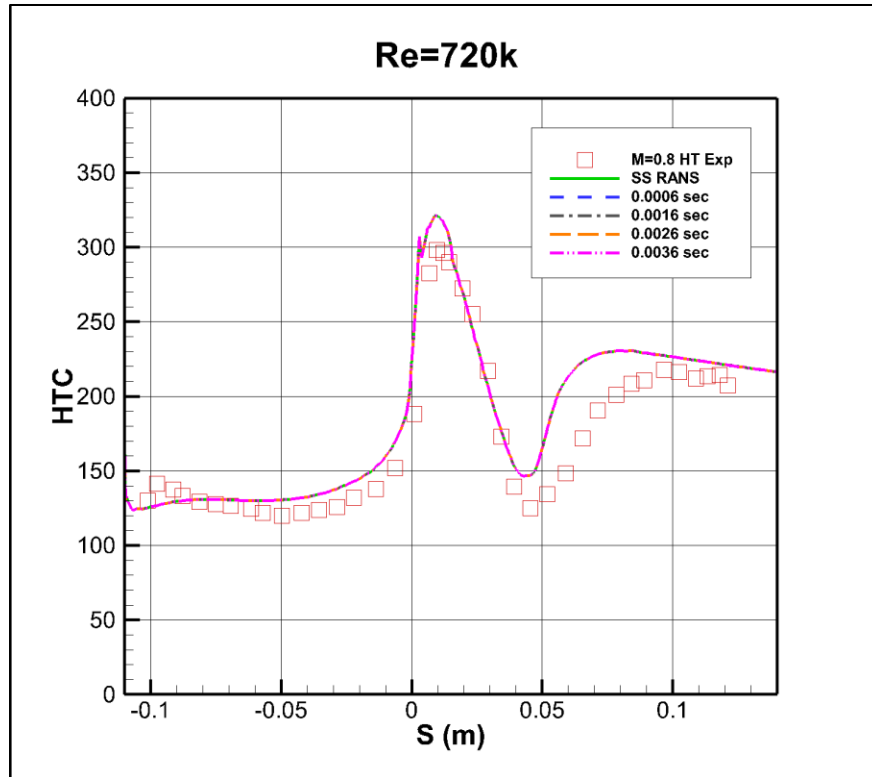
Figure 6.47. Heat transfer coefficient comparison from transient SAS simulation for Re = 720,000 and Ma = 0.8 at high turbulence

7. CONCLUSIONS AND FUTURE WORK

7.1. Conclusions

In order to accurately model a specific flow case, the turbulence and transition models to be used must be validated against different experimental cases. These should include general cases, such as the T3-series of experiments for a transitional boundary layer on flat (Savill, 1993), as well more complicated cases similar to the flow that is desired to be modeled. Validation is especially important for turbomachinery applications because the flow patterns within a gas turbine can be highly turbulent and extremely complex. CFD simulations can save money early in the design process by reducing the need for physical models; however, in order to trust the results, the turbulence and transition models need to be validated against similar flow problems.

This thesis has presented the validation of the SST turbulence model and the γ-Re_θ transition model against aerodynamic and heat transfer experiments using the first stage stator vane from a high-altitude UAV. The high altitude causes the engine to operate at low pressures and low Reynolds numbers. Under these conditions, transition can play important role in the boundary layer development on the vane surfaces.

The first part of the study examined the aerodynamic loading of the vane under various flow conditions. For most cases, the experimental and computational vane loading results matched very well. At the highest Reynolds numbers, there was a sudden increase in pressure near the tail end of the vane on the suction surface. In addition to the surface pressure distribution, the loss coefficient downstream from the instrumented vane was also examined. The loss coefficients showed significant differences between the experimental and computational results. There are a few possible reasons for the discrepancy. It is possible that the RANS

steady state simulations are smoothing out some of the larger turbulent structures within the flow, and this is affecting the flow pattern downstream from the vane cascade. During the experiments, there was also some unsteadiness reported from the Roots blower. This was not quantified in the available experimental data, nor can it be accounted for with the constant boundary conditions used in the simulation. In order to try improving the loss coefficient downstream of the vanes, a transient SAS simulation was run. In theory, this should better capture any larger turbulent structures in the freestream, but for the case tested, the loss coefficient plot only got worse. Because of this, it is believed that the discrepancy is due to some of the unsteadiness within the experimental flow field. This cannot be captured with the simulations as they are setup now due to the constant boundary conditions. Additionally, the information to setup a fluctuating boundary is not available.

The second part of the study examined the heat transfer on the vane surface. At the low turbulence levels, the flow remained laminar over the entire suction surface of the vane and there was an excellent match between experimental and computational results. At the high turbulence level, the boundary layer on the suction surface began to show transitional flow. At Reynolds numbers of 90,000 and 180,000, the flow remained laminar and showed excellent agreement between the experimental and computational results. At higher Reynolds numbers, the flow became transitional, and disagreements between the experimental and simulation results became apparent. The simulations predicted an earlier transition than what was measured in the experiment. They also over predicted the heat transfer coefficient in the fully turbulent region.

The results of this study show that for many different flow conditions, the SST turbulence model and γ-Re$_\theta$ transition model can provide an accurate result for the both the pressure loading and heat transfer on the vane surface. At higher Reynolds numbers and turbulence levels, some

discrepancies become apparent between the experimental results and the computational results for the heat transfer calculations. This is likely due to a lack of information on the turbulence level within the cascade as well as some of the limitations of the SST turbulence model and the γ-Re$_\theta$ transition model used for the simulations.

7.2. Future Work

Based on the information collected from the original experiments, the simulations as presented are fully complete. In order to better match the heat transfer at a high Reynolds number and high turbulence level, additional improvements to the SST turbulence model and γ-Re$_\theta$ transition model are needed. This is currently an area of ongoing research. Any updated turbulence and transition models used for simulation of the vane cascade experiments will still suffer from a lack of certainty about the inlet turbulence level.

The turbulence level is an extremely important aspect of the flow field. A small difference in the turbulence intensity can make the difference between a well-matched heat transfer coefficient and an early transition point with an over predicted heat transfer coefficient. For the cases presented, the turbulence intensity was only measured for a couple of the experimental cases, and then it was assumed that all cases with the same inlet nozzle configuration would experience the same level of turbulence. If additional experimental work is done with these cases or similar cases, the turbulence intensity should be measured for all cases. Ideally, multiple measurements would be taken throughout the inlet nozzle in order to be able to accurately match the decay of turbulent kinetic energy; however, even one measurement per test case, directly in front of the test cascade would provide valuable information about the flow field.

REFERENCES

Ames, F. (1997). "The Influence of Large-Scale High Intensity Turbulence on Vane Surface Heat Transfer." Journal of Turbomachinery, 23-30.

Ames, F. E. (1999). "An Algebraic Model for High Intensity Large Scale Turbulence." ASME Turbo Expo. Indianapolis, Indiana.

Ames, F. E., Argenziano, M., & Wang, C. (2004). "Measurement and Prediction of Heat Transfer Distributions on an Aft-Loaded Vane Subjected to the Influence of Catalytic and Dry Low NOx Combustor Turbulence." Journal of Turbomachinery, 139-149.

Ames, F. E., Wang, C., & Barbot, P. A. (2003). "Measurement and Prediction of the Influence of Catalytic and Dry Low NOx Combustor Turbulence on Vane Surface Heat Transfer." Journal of Turbomachinery, 221-231.

Bardina, J. E., Huang, P. G., and Coakley, T. J. (1997). "Turbulence Modeling Validation, Testing, and Development." NASA Technical Memorandum 110446.

Anderson, J. (2011). "Fundamentals of Aerodynamics." McGraw-Hill.

ANSYS, Inc. (2012). "ANSYS CFX-Solver Theory Guide Release 14.5."

B. Baldwin, B., & Lomax, H. (1978). "Thin-layer approximation and algebraic model for separated turbulent flows." 16th Aerospace Sciences Meeting. AIAA 78-257.

Center for Computationally Assisted Science and Technology. (2018). "Hardware." https://www.ccast.ndsu.edu/resources/hardware/ Accessed: 4/14/2019

Chen, K. K., & Thyson, N. A. (1971). "Extension of Emmons' Spot Theory to Flows on Blunt Bodies." AIAA Journal, 821-825.

Cho, J. R., & Chung, M. K. (1992). "A k-e-y Equation Turbulence Model." Journal of Fluid Mechanics, 301-322.

Cutrone, L., Palma, P., Pascazio, G., & Napolitano, M. (2008). "Predicting transition in two- and three-dimensional separated flows." International Journal of Heat and Fluid Flow, 504-526.

De Palma, P. (2006). "Numerical simulations of three-dimensional transitional compressible flows in turbomachinery cascades." International Journal of Numerical Methods for Heat & Fluid Flow, 509-529.

Dhawan, S., & Narasimha, R. (1958). "Some properties of boundary layer flow during the transition from laminar to turbulent motion." Journal of Fluid Mechanics, 418-436.

Eppler, R. (1978). "Practical Ca1culation of Laminar and Turbulent Bled-Off Boundary Layers." NASA Technical Memorandum 75328. (translated from Ingenieur Archiv, Vol. 32, 1963, (pp. 221-245).

Egorov, Y., & Menter, F. (2007). "Development and Application of SST-SAS Turbulence Model in the DESIDER Project." Second Symposium on Hybrid RANS-LES Methods, Corfu, Greece.

Flage, A. P. (2015). "Computational Investigation of Low-Pressure Turbine Aerodynamics." Thesis. North Dakota State University.

Glassman, J., Whitney, W., & Steward, W. (1994). "Turbine Design and Application." NASA SP-290.

Gostelow, J. P., Blunded, A. R., & Walker, G. J. (1994). "Effects of Free-Stream Turbulence and Adverse Pressure Gradients on Boundary Layer Transition." Journal of Turbomachinery, 392-404.

Grotjans, H., & Menter, F. R. (1998). "Wall Functions for General Application CFD Codes." European Computational Fluid Dynamics Conference.

Hinze, J. O. (1959). "Turbulence." New York: McGraw-Hill.

Hoffmann, K. A., & Chiang, S. T. (1998). "Computational Fluid Dynamics." Wichita, KS: Engineering Education System.

Huang, J., Corke, T. C., & Thomas, F. O. (2003). "Plasma actuators for separation control of low-pressure turbine blades." AIAA Paper AIAA-2003-1027.

Huber, J. J. (2013). "Numerical Simulations of Incompressible and Compressible Transitional Turbine Flows." Thesis. North Dakota State University.

Jones, W. P., & Launder, B. E. (1972). "The Prediction of Laminarization with a Two-Equation Model of Turbulence." International Journal of Heat and Mass Transfer, 301-314.

Kachanov, Y. S. (1994). "Physical Mechanisms of Laminar-Boundary-Layer Transition." Annual Rev. Fluid Mechanis, 411-482.

Kaszeta, R. W., Simon, T. W., & Asphis, D. E. (2001). "Experimental Investigation of Transition to Turbulence as Affected by Passing Wakes." ASME Turbo Expo 2001, ASME Paper No. 2001-GT-0195.

Kaynak, U. (2012). "Transition at Low-Re Numbers for some Airfoils at High Subsonic Mach Numbers." In Low Reynolds Number Aerodynamics and Transition. InTech.

Kingery, L. B., Suzen, Y. B., & Ames, F. E. (2010). "Computations of Heat Transfer in Transitional Turbine Flows." 10th AIAA/ASME Joint Thermophysics and Heat Transfer Conference.

Kolmogorov, A. N. (1941). "Local Structure of Turbulence in Incompressible Viscous Fluid for Very Large Reynolds Numbers." Doklady Akademiya Nauk SSSR, 299-303.

Lake, J. P., King, P. I., & Rivir, R. B. (1999). "Reduction of separation losses on a turbine blade with low Reynolds number." AIAA Paper AIAA-99-0242.

Launder, B. E., & Sharma, B. I., (1974). "Application of the Energy Dissipation Model of

        Turbulence to the Calculation of Flow Near a Spinning Disc." Letters in Heat and Mass

        Transfer, vol. 1, no. 2, (pp. 131-138).

Mayle, R. E. (1991). "The Role of Laminar-Turbulent Transition in Gas Turbine Engines."

        Journal of Turbomachinery, 509-537.

Mayle, R. E., & Schulz, A. (1996). "The Path to Predicting Bypass Transition." Journal of

        Turbomachinery, 405-411.

McAuliffe, B. R., & Metin, M. I. (2008). "Numerical Study of Instability Mechanisms Leading

        to Transition in Separation Bubbles." Journal of Turbomachinery.

McAuliffe, B. R., & Metin, M. I. (2010). "Transition Mechanisms in Separation Bubbles Under

        Low- and Elevated- Freestream Turbulence." Journal of Turbomachinery.

McDonough, J. (n.d.). "Introduction to Turbulence Lecture Notes." Retrieved from

        http://www.engr.uky.edu/~acfd/lctr-notes634.pdf Accessed: 2/16/2019

Medic, G., & Durbin, P. A. (2002). "Toward Improved Prediction of Heat Transfer on Turbine

        Blades." Journal of Turbomachinery, 187-192.

Menter, F. R. (1994). "Two-Equation Eddy-Viscosity Turbulence Models for Engineering

        Applications." AIAA.

Menter, F. R. (1997). "Eddy Viscosity Transport Equations and Their Relation to the k-ε

        Model." Journal of Fluids Engineering, 876-884.

Menter, F. R. (1992). "Influence of Freestream Values on k-ω Turbulence Model Predictions."

        AIAA Journal, Vol. 30, No. 6, (pp. 1657-1659).

Menter, F. R., & Egorov, Y. (2005). "A Scale-Adaptive Simulation Model using Two-Equation Models." 43rd AIAA Aerospace Sciences Meeting and Exhibit. Reno, Nevada. AIAA 2005-1095.

Menter, F. R., & Egorov, Y. (2010). "The Scale-Adaptive Simulation Method for Unsteady Turbulent Flow Predictions. Part 1: Theory and Model Description." Flow Turbulence Combust (pp. 113-138). Springer Science.

Menter, F. R., & Langtry, R. B. (2012). "Transition Modelling for Turbomachinery Flows." In Low Reynolds Number Aerodynamics and Transition. InTech.

Menter, F. R., Kuntz, M., & Bender, R. (2003). "A Scale-Adaptive Simulation Model for Turbulent Flow Predictions." AIAA.

Menter, F. R., Langtry, R. B., Likki, S. R., Suzen, Y. B., Huang, P. G., & Volker, S. (2006). "A Correlation-Based Transition Model Using Local Variables - Part 1: Model Formulation." Journal of Turbomachinery, 413-422.

Menter, F. R., Langtry, R. B., Likki, S. R., Suzen, Y. B., Huang, P. G., & Volker, S. (2006). "A Correlation Based Transition Model Using Local Variables - Part 2: Test Cases and Industrial Applications." Journal of Turbomachinery, 423-434.

Michel, R. (1951). "Etude de la Transition et Calcul de la Trainee des Pro fils d'aile en Incompressible." ONERA Publ. 58.

Mihelish, M. P., & Ames, F. E. (2013). "The Development of a Closed Loop High Speed Cascade Wind Tunnel for Aerodynamic and Heat Transfer Testing at Moderate to Low Reynolds Numbers." ASME Turbo Expo. San Antonio, Texas.

Mihelish, M. P., & Ames, F. E. (2013). "Aerodynamic Loss Measurements in a Compressible Flow Vane Cascade Showing the Influence of Reynolds Number Lapse." ASME Turbo Expo. San Antonio, Texas.

Morkovin, M. V. (1969). "On the many faces of transition." In Viscous Drag Reduction (pp. 1-31). New York: Plenum Press.

Piotrowski, W., Elsner, W., & Drobniak, S. (2010). "Transition Prediction on Turbine Blade Profile with Intermittency Transport Equation." Journal of Turbomachinery.

Praisner, T. J., & Clark, J. P. (2007). "Predicting Transition in Turbomachinery - Part 1: A Review and New Model Development." Journal of Turbomachinery, 1-13.

Praisner, T. J., & Clark, J. P. (2007). "Predicting Transition in Turbomachinery - Part 2: Model Validation and Benchmarking." Journal of Turbomachinery, 14-22.

Reynolds, O. (1883). "An Experimental Investigation of the Circumstances Which Determine Whether the Motion of Water Shall Be Direct or Sinuous, and of the Law of Resistance in Parallel Channels." Philosophical Transactions of the Royal Society of London, Vol. 174 (pp. 935-982). Royal Society.

Savill, A. M. (1993). "Some Recent Progress in the Turbulence Modeling of By-pass Transition. In Near End Wall Flows" (pp. 829-848). Elsevier Science Publishers.

Schlichting, H. (1979). "Boundary Layer Theory." New York: McGraw-Hill.

Schubauer, G. B., & Klebanoff, P. S. (1955). "Contribution on the Mechanics of Boundary Layer Transition." NASA. Technical Note 3489.

Simon, F. F., & Stephens, C. A. (1991). "Modeling of the Heat Transfer in Bypass Transitional Boundary-Layer Flows." NASA. Technical Paper 3170.

Simon, T. W., Qiu, S., & Yuan, K. (2000). "Measurements in a Transitional Boundary Layer Under Low-Pressure Turbine Airfoil Conditions." NASA. CR-2000-209957.

Smirnov, P. E., & Menter, F. R., (2009). "Sensitization of the SST Turbulence Model to Rotation and Curvature by Applying the Spalart-Shur Correction Term." Journal of Turbomachinery.

Smith, A. M. O. & Cebeci, T. (1967). "Numerical solution of the turbulent boundary layer equations." Douglas Aircraft Division report DAC 33735.

Smith, A. M. O. & Gamberoni, N. (1956). "Transition, Pressure Gradient and Stability Theory." Douglas Aircraft Company. Technical Report ES-26388.

Solomon, W. J., Walker, G. J., & Gostelow, J. P. (1995). "Transition Length Prediction for Flows with Rapidly Changing Pressure Gradients." ASME International Gas Turbine and Aeroengine Congress & Exposition.

Spalart, P. R. (2000). "Strategies for turbulence modeling and simulations." International Journal of Heat and Fluid Flow, 252-263.

Spalart, P. R. & Allmaras, S. R., (1994). "A One-Equation Turbulence Model for Aerodynamic Flows." Recherche Aerospatiale, No. 1, pp. 5-21.

Spalart, P. R., & Shur, M. (1997). "On the Sensitization of Turbulence Models to Rotation and Curvature." Aerospace Science and Technology. 297-302.

Spalart, P. R., & Strelets, M. K. (2000). "Mechanisms of transition and heat transfer in a separation bubble." Journal of Fluid Mechanics, 329-349.

Stahl, K. A., Moualeu, L. P. G., Long, J. A., Ames, F. E., & Suzen, Y. B. (2014). "Heat Transfer Measurements in a Compressible Flow Vane Cascade Showing the Influence of Reynolds

Number, Mach Number, and Turbulence Level on Transition and Augmentation of Laminar Heat Transfer by Free-Stream Turbulence." AIAA.

Steelant, J., & Dick, E. (1996). "Modelling of Bypass Transition with Conditioned Navier-Stokes Equations Coupled to an Intermittency Equation." International Journal for Numerical Methods in Fluids, 193-220.

Stieger, R. D., Hollis, D., & Hodson, H. P. (2004). "Unsteady Surface Pressures Due to Wake-Induced Transition in a Laminar Separation Bubble on a Low-Pressure Cascade." Journal of Turbomachinery. 544-550.

Suzen, Y. B., & Huang, P. G. (1999). "Modeling of Flow Transition Using an Intermittency Transport Equation." NASA. CR-1999-209313.

Suzen, Y. B., & Huang, P. G. (2005). "Comprehensive validation of an intermittency transport model for transitional low-pressure turbine flows." The Aeronautical Journal of the Royal Aeronautical Society.

Suzen, Y. B., & Huang, P. G. (2005). "Numerical Simulation of Unsteady Wake/Blade Interactions in Low-Pressure Turbine Flows Using an Intermittency Transport Equation." Journal of Turbomachinery, 431-444.

Suzen, Y. B., Huang, P. G., & Ashpis, D. E. (2007). "A Computational Fluid Dynamics Study of Transitional Flows in Low-Pressure Turbines under a Wide Range of Operating Conditions." Journal of Turbomachinery, 527-541.

Suzen, Y. B., Huang, P. G., Hultgren, L. S., & Ashpis, D. E. (2001). "Predictions of Separated and Transitional Boundary Layers Under Low-Pressure Turbine Airfoil Conditions Using an Intermittency Transport Equation." 39th AIAA Aerospace Sciences Meeting & Exhibition AIAA 2001-0446.

Suzen, Y. B., Xiong, G., & Huang, P. G. (2002). "Predictions of Transitional Flows in Low-Pressure Turbines Using Intermittency Transport Equation." AIAA Journal, 254-266.

Thurman, D., Flegel, A., Giel, P. (2014). "Inlet Turbulence and Length Scale Measurements in a Large Scale Transonic Turbine Cascade." 50th AIAA/ASME/SAE/ASEE Joint Propulsion Conference AIAA 2014-3934.

van Ingen, J. L. (2008). "The e^N Method for Transition Prediction. Historical review of Work at TU Delft." 38th Fluid Dynamics Conference and Exhibit. AIAA 2008-3830.

Versteeg, H. K., & Malalasekera, W. (2007). "An Introduction to Computational Fluid Dynamics: The Finite Volume Method." Pearson Education Limited.

Vicedo, J., Vilmin, S., Dawes, S., & Savill, A. M. (2004). "Intermittency Transport Modeling of Separated Flow Transition." Journal of Turbomachinery, 424-431.

Volino, R. J. (2002). "Separated Flow Transition Under Simulated Low-Pressure Turbine Airfoil Conditions - Part 1: Mean Flow and Turbulence Statistics." Journal of Turbomachinery, 656-664.

Volino, R. J. (2002). "Separated Flow Transition Under Simulated Low-Pressure Turbine Airfoil Conditions - Part 2: Turbulence Spectra." Journal of Turbomachinery, 645-655.

Volino, R. J. & Simon, T. W. (1991). "Bypass Transition in Boundary Layers Including Curvature and Favorable Pressure Gradient Effects." NASA. Contractor Report 187187.

Walker, G. (1993). "The Role of Laminar-Turbulent Transition in Gas Turbine Engines: A Discussion." Journal of Turbomachinery, 207-217.

Wang, L., Fu, S., Carnarius, A., Mockett, C., & Theile, F. (2010). "A modular RANS approach for modelling laminar-turbulent transition in turbomachinery flows." International Journal of Heat and Fluid Flow, 62-69.

Westin, K. J. A., and Henkes, R. A. W. M. (1997). "Application of Turbulence Models to Bypass Transition." Journal of Fluids Engineering, 859-866.

White, F. (2006). "Viscous Fluid Flow." McGraw-Hill.

Wilcox, D. (2006). "Turbulence Modeling for CFD." DCW Industries, Inc.